OBSERVATIONS OF THE COALESENCE OF MISCIBLE DROPS

QIAN BIAN
(B.Eng., SJTU)

A THESIS SUBMITTED

FOR THE DEGREE OF MASTER OF ENGINEERING

DEPARTMENT OF MECHANICAL ENGINEERING

NATIONAL UNIVERSITY OF SINGAPORE

2006

Acknowledgements

I would like to express my deep gratitude and indebtedness to Prof. Siggi Thoroddsen, for introducing me to this field of coalescence of miscible drops, and assistance in construction of the experimental setup as well as performing the experiments. I would also like to thank him for his encouragement, continuous support and guidance during this work. Without his advice and support, this project would not have been possible.

In addition, many thanks are given to Mr. Tan Kim Wah, Mr. Yap Chin Seng, Mrs. Lee Cheng Fong and Mrs. Iris Chew for their instructions on using various equipments and administrative helps which made research and student life so much easier. It is a pleasure to acknowledge useful conversations and cooperation during the course of research as well as study with my colleagues Li Yangfan and Xu Zhifeng.

Table of Contents

Summary

This experimental study investigates a fundamental phenomenon in free-surface flows, i.e. the coalescence of two liquid masses, which come into contact. The focus is on the coalescence of two fluid masses, which have large differences in liquid properties. The coalescence configuration studied is a pendent drop, which is slowly grown from a needle until it touches a flat surface of a deep pool. The main part of the study looks at the rapid coalescence motions when the two liquids have a large difference in surface tension and/or a large difference in viscosity. A dual-frame PIV camera is used to image each coalescence event at two times, one immediately following the first contact and the other at a precisely controlled time thereafter. By imaging numerous similar drops, using different time-delays, we are able to build up the time sequence showing the evolution of the drop shape during the coalescence.

The coalescence of a water drop with a pool of ethanol, where the difference in surface tension is large, shows the formation of strong Marangoni waves, which travel up the drop. The shape of these waves is analyzed to extract their amplitude as a function of the arclength along the drop surface, starting from the bottom tip of the drop. These waves are shown to be self-similar, when scaled with time to the 3/2 power. The coalescence speed of the waves is also observed to be controlled by the liquid having the lower surface tension. Images taken under the pool surface, show a cone of water being driven down into the ethanol pool.

The coalescence of a very viscous liquid drop with a low-viscosity pool of either water or ethanol, shows markedly different surface shapes. Capillary waves are absent and the lower viscosity liquid moves along the drop surface, as if it were

spreading along a solid. The region where the two fluids meet is characterized by a very sharp corner. The curvature of this corner was measured from the images and is in some cases at the limits of the experimental sensitivity, with a radius of curvature of a few microns.

Limited experiments were also carried out with surfactant solutions coalescing with pure water drops. The shape of the surface waves might be useful in characterizing or distinguishing different groups of surfactants.

List of Figures

List of Tables

Nomenclature

a	Capillary length
c	Concentration
C	Constant
F	Free surface of the liquid
g	gravity
G	Dimensionless function
P_{tip}	Pressure at bottom tip of drop
r	Instantaneous radius of the coalescing neck between drops
R	Drop radius
R_1, R_2	Principal radii of curvature
s	Arclength
u	Velocity component
x	Space coordinate
y	Space coordinate
α	Power-law exponent
β	Angle of the free surface touching a solid surface
δ	Viscous length scale

ϕ	Angle or the velocity potential
η	Similarity variable
κ	Curvature
ρ	Liquid density
σ	Surface tension
μ	Liquid dynamic viscosity
ν	Kinematic viscosity
τ	Capillary-inertial time-scale
ξ	Similarity variable

1 Introduction

1.2 General outline

Recently there has been renewed work concentrating on the two basic *'singularities'* occurring in free-surface flows, that is to say the breakup of a liquid thread into two pieces and the merging or coalescence of two liquid masses into one. This interest has been motivated both by new theories as well as improved experimental techniques which have allowed more detailed study of the very fast motions which occur during these singularities. The pinch-off of a drop and the breakup of a liquid thread have been extensively studied, as reviewed by Eggers (1997). This has for example revealed an extraordinary pinch-off cascade by Shi *et al.* (1994), which occurs when a viscous drop is pinched off from a nozzle. The neck region undergoes a cascade of smaller and smaller necks emerging before the eventual break-off. It has recently been suggested that singularities in the surface curvature can generate jetting from a free surface, see Zeff et al. (2000). Such singularities might be used in manufacturing, such as inkjet printing of electronic components using polymeric liquids (Sirringhaus *et al.* 2000), or other manipulations in free-surface micro-fluidics, as in Velev *et al.* (2003). It is therefore important to understand the basic dynamics of free-surface flows at small length-scales.

Coalescence is also important on the nano-scale for alloy formation by coalescence of nano-sized particles, see Lee *et al.* (2002) and Martinez-Herrera and Derby (1995).

However, as Eggers (1997) points out, the time resolution of previous measurements has been *'insufficient to observe much of the extremely rapid motion after two surfaces touch''*. In this thesis we will use a new experimental setup to study

the early motions when two liquid masses merge together. The focus will be on the coalescence of two miscible liquids which have different liquid properties, such as different surface tension, or different viscosity. Some experiments will also study the effects of surfactants on the coalescence dynamics.

To observe the very fast motions we have used a dual-frame camera which can take two high-resolution images of each coalescence event. This camera is designed to perform *Particle Image Velocimetry* (PIV), but is here used simply as a camera which can take two frames very close together in time. By using a precise electronic trigger and many identical or very similar drops we can build up a sequence of images showing the coalescence process.

Due to its commonness in nature as well as in industrial processes and easy realization in experimental setup, our interest in this project is mainly focuses on studying the coalescence of a drop onto a flat liquid surface. Limited experiments of coalescence between a drop and a much smaller liquid mass at the tip of a small needle were also included. In addition, few observations were done for the purposes of demonstrating and investigating the evolution of the wave shape which develops underneath the flat liquid surface.

Studying the effect of difference in liquid properties on drop coalescence, we sorted the experimental data into four main groups: Firstly, liquids that have a large difference in surface tension, but are both of low viscosity; Secondly, a low-viscosity liquid coalescing with a much higher viscous liquid without much surface tension difference between the two; Thirdly, the effects of variation in viscosity on the Marangoni waves generated from surface tension gradient; Finally, the coalescence of a water drop with a water pool which contains some surfactant molecules, was also investigated and will be presented.

We start by looking at the coalescence of a water drop with a pool of water or a pool of ethanol/water solution, which builds a large difference in surface tension between the two liquids and at the same time retains low viscosity for both liquids. Effects of the drop size on the coalescence were also investigated by testing different diameter tubes from which the drops were generated. The amplitude of the resulting Marangoni waves were measured and scaled with respect to the static drop shape. Furthermore, the coalescence of a liquid drop with a much smaller liquid droplet was investigated to see the effects of the boundary conditions.

We are also interested in the coalescence of a glycerin/water drop with a water pool and the effect of viscosity on the coalescence motions. By varying the concentration of glycerin, the difference in dynamic viscosity μ can therefore be set to as high as a factor of 600 above that of water, while keep the surface tension not too much changed, at about 65 dyn/cm for the water/glycerin mixtures versus 73 dyn/cm for the pure water. Experimenting with different viscous drops, we qualitatively analyzed the change of coalescence speed and quantitatively measured the total curvatures at the corner of the contact region, where the two liquids meet.

Research interests in this project also included observation of the coalescence of a drop onto a flat liquid surface, while maintaining both a large difference in surface tension, as well as a large difference in the viscosity of the two liquids. This is accomplished by keeping the flat surface as a 94% ethanol/water mixture, while changing the viscosity of the drop using water/glycerin mixtures as high up to 98% glycerin.

Finally, we present experimental results for a water drop coalescing onto a water pool which contains some surfactant molecules. The surfactants lowers the surface tension of the bottom pool liquid, but also introduces some dynamic surface

tension effects. The measurement of Marangoni waves formed in this experiment were compared to that observed for the coalescence of a water drop with alcohol, because surfactant molecules mainly stay on the liquid surface and thereby gradually change the surface tension of the liquid when surfactant concentration is below some critical value. For investigating the effects of the strength of surfactant concentration on the Marangoni waves, two surfactant solutions with different concentrations were experimented with.

1.2 Objectives and Scope

This work aims at understanding the basic fluid dynamics of free-surface flows when a difference in liquid properties produces strong Marangoni stresses or strong gradients in viscosity. To produce this large variation in surface tension and viscosity along a continuous free surface, two drops, or a drop and a flat surface, were brought into contact to coalesce. This produces an initial configuration with a step change in liquid properties along the interface. The objective is to see how quickly and in what way the free surface will respond to this applied stress.

Most interest is herein placed on understanding the very earliest motions produced in this configuration. However, the scope of the work is limited to the length- and time-scales which can be observed with the available instrumentation. Inherent time-delay between the initial contact between the two liquids and the time when the camera and flash-units can respond, makes it impossible to observe the very earliest motions.

Various liquid combinations are used to generate a range of different strength of the Marangoni stresses and viscosity differences between the two liquids. This produces results which should be of general relevance and applicable to various configurations, where these types of free-surface stresses arise.

2 Literature Review

In this chapter we will review the previous work on coalescence performed to date, focusing on the experimental studies, but also reviewing a few of the major theoretical papers on this phenomenon.

The only previous measurements capable of time resolving the original motions were obtained by Menchaca-Roca *et al.* (2001). They used two mercury drops sitting on a glass plate, as shown in the figure below. These drops were pushed together until they came into contact and the coalescence motion was recorded with high-speed cameras. They used electrical contact between the two drops to start the recording. However, most of their measurements were carried out with a camera which does not have very fast frame-rates, only about 1000 frames/s. They also used another much higher speed film camera capable of taking only 8 consecutive frames, with *dt* about 10 μs. They only show 16 data points using this faster camera, possibly due to difficulty with triggering the images.

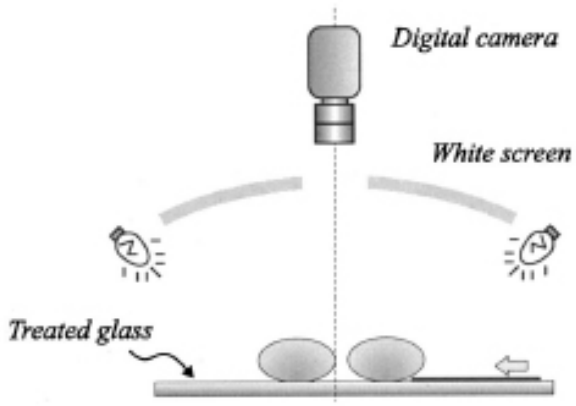

Figure 2-1: The experimental setup used by Menchaca-Roca *et al.* (2001).

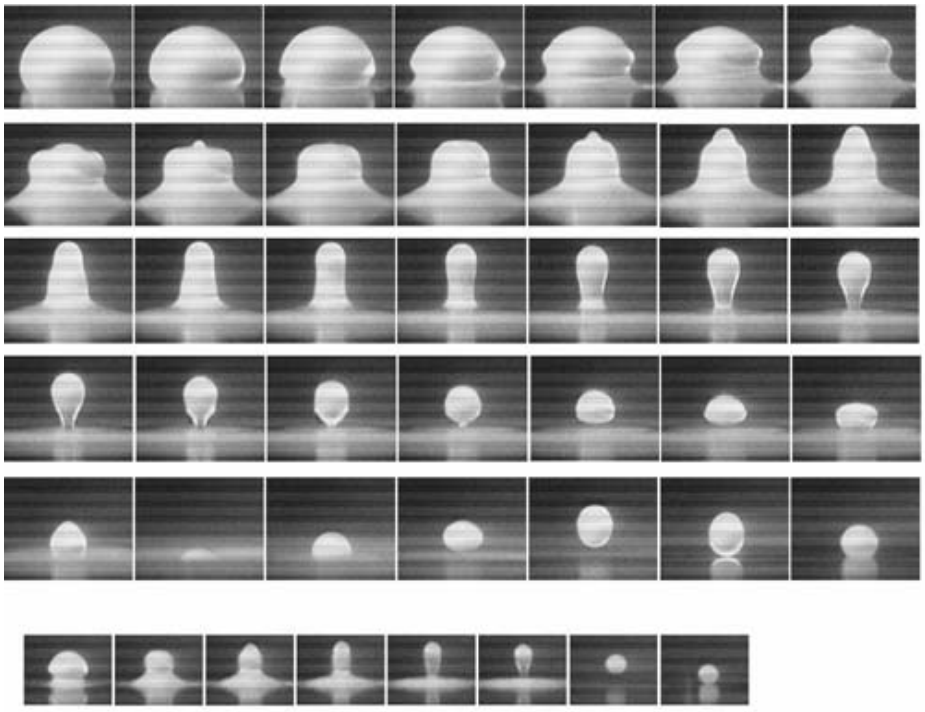

Figure 2-2: Two steps in the coalescence cascade of a drop which sit on a flat liquid surface.

Similar measurements were carried out by Thoroddsen et al. (2005) who used a novel ultra-high-speed video camera, developed by Etoh *et al.* (2002, 2003) and capable of acquiring 103 consecutive frames at frame-rates up to 1 million frame/s. They focus on the initial coalescence motions, by growing a pendent and a sessile drop on vertically aligned metal tubes, until they come into contact. Their setup did not therefore allow the study of the long-term evolution of coalescing drops, such as the *coalescence cascade* discovered by Thoroddsen & Takehara (2000), for a drop coalescing with a flat liquid surface. This cascade is observed when a drop impacts onto a pool of liquid at very low velocity, by releasing it from a nozzle very close to the free surface. This cascade proceeds at the capillary-inertial time scale, with a daughter drop being pinched off at the top of the original drop. This daughter drop then settles onto the surface and a new step in the cascade takes place. Each initial condition is geometrically identical, with a sphere sitting on a flat surface. Similar

cascade for a drop at an immiscible liquid-liquid interface, i.e. where the air is replaced by another immiscible liquid, was previously discovered by Charles & Mason (1960). They used a high-speed 16 mm movie camera, which could reach 10,000 frame/s. For the liquid-liquid case studied by them the coalescence speeds are much slower than the liquid-air case, making 10,000 frame/s sufficiently fast to observe the details.

Very recently, measurements of coalescence of drops in micro-devices have been carried out by Wu *et al.* (2003) and reported in more detail by Wu *et al.* (2004). These measurements are in overall agreement with those of Thoroddsen *et al.* (2005).

Thoroddsen et al. (2005) have studied the related problem of the coalescence of two air bubbles, grown at the openings of two needles in ethyl alcohol. They observed that the interface shape is different for the coalescence of two bubbles from that for two drops. For two bubbles the neck region connecting the two bubbles has a circular shape.

The coalescence of two bubbles has previously been studied using a linear array of high-speed photodiodes by Stover et al.(1997). They looked at very small bubbles grown by electro-phoresis and were as small as 50 μm. The limitations of measuring only one line of photodiodes at a time made the measurement of surface shapes very difficult and the shapes are not the same as observed in the previously mentioned study. The speed of coalescence is also different from that study, but one should keep in mind that the sizes of the bubbles are quite different in the two studies.

Theoretical treatment of coalescence has mostly focused on the two-dimensional configuration. The classic paper on the topic is by Keller and Miksis (1983) where they look at the coalescence of liquid wedges in two dimensions. For wedges the initial configuration is self-similar having no characteristic length-scale,

the only geometric factor being the value of the cone-angle. These self-similar solutions can not be directly applied here, as our configuration has imposed external length-scale of the drop diameter. This paper will be described in detail in the theoretical section of this thesis.

Keller *et al.* (2000) have recently computed the coalescence shapes for two-dimensional inviscid wedges. These calculations are based on the self-similar solutions found earlier for capillary driven flows, by Keller & Miksis (1983). For very large cone-angles the coalescence motions lead to reconnections of the free surface as shown in a later figure.

Oguz & Prosperetti (1989) have numerically simulated the coalescence of two flat surfaces connected at a neck region. Their calculations are inviscid and were performed in both two and three-dimensions. They have shown the formation of bubble rings when the top drop is moving downwards, as the capillary wave on the upper surface touches the capillary wave on the lower surface. Such bubble rings have been observed experimentally during the impact of a drop onto a liquid surface by Thoroddsen et al. (2003).

Miksis & Vanden-Broeck (1999) have found the corresponding self-similar solution for viscous wedges, over a limited range of viscosity ratios between the inner and outer liquids.

The coalescence of very viscous liquids, where inertia is negligible, has been widely studied due to its importance to sintering (see Martinez-Herrera & Derby (1995)) and coarsening of emulsions Rother et al. (1997). The coalescence of nano-particles such as gold is a recent topic of interest and fluid models may be of relevance here, see Lee et al. (2002).

Hopper (1990, 1992, 1993a,b) has found an analytical solution for the coalescence of two viscous cylinders. The solution is two-dimensional, but allows for different radii for the two cylinders. Richardson (1992) explained these solutions in more detail.

Eggers *et al.* (1999) have studied the asymptotics of the viscous-dominated coalescence, where the 3-D problem can be treated as if it where 2-D. Their work is formulated for the very early stages of the coalescence, where the radius of the neck region is less than 3.5% of the drop radius, i.e. r/R < 0.035. These asymptotics show that the earliest motions of the neck should proceed as

$$r / R = const(t \ln t)$$

The speed is not exactly constant, rather has a *'logarithmic correction'*. However, recent measurements of Arts et al. (2005) have failed to find such a logarithmic correction, showing very linear behavior for the viscous dominated cases. The measurements of Thoroddsen et al. (2005) showed some early linear behavior, but could not look at the earliest coalescence for r/R < 0.035.

Duchemin *et al.* (2003) have performed inviscid simulations of this setup, for the very early coalescence. They find repeated reconnections entrapping toroidal regions of outer fluid, when r/R < 0.035. This is qualitatively similar to the numerical results by Oguz & Prosperetti (1989) for two approaching surfaces, as well as the results by Keller et al. (2000) for very wide 2-D wedges.

The paper by Eggers *et al.* (1999) concentrates on the very viscous coalescence, but also contains a short model for inviscid coalescence. Their argument shows that the neck should grow as time to the power of a half, by the following argument. The capillary pressure is balanced against the dynamic pressure. This gives

$$r / R = const(\sigma / \rho) t^{1/2}$$

which contains an unknown proportionality constant. The numerical and theoretical work of Duchemin, Eggers & Josserand (2003) refined this model and comes up with an expression containing no adjustable constant

$$r / R = 1.62\left(t / \tau\right)^{1/2}$$

Where τ is the characteristic capillary-inertial time-scale

$$\tau = \left(\rho R^3 / \sigma\right)^{1/2}$$

The measurements of Wu *et al.* (2004) and Arts *et al.* (2005) show that the value of the prefactor is in the range of 1.09 – 1.29. The data taken from Thoroddsen *et al.* (2005) shows a similar value for water drops, of around 1.28. Therefore, all three of these studies show a lower value of the prefactor, than the theory above predicts. Possible explanations are that the theory does not include any gas on the outside of the drops. In the numerics and theory, the repeated reconnections of the surfaces, entrap toroidal bubbles or voids. These reconnections cause some problems for the theory and numerics. To overcome these problems, the authors restart the flow after every reconnection, from rest. The real flow would not behave in such a manner and this may cause, some problems. However, starting back from rest after every reconnection should slow down the outwards motion of the neck radius and therefore result in a smaller prefactor, which is the opposite to what is observed in the above-mentioned experiments.

Rein (2002) has looked at the energy-balance during the coalescence. He points out the need to measure the kinetic energy of the pool liquid, where a vortex ring often is generated, see Peck & Sigurdson (1994).

3 Theoretical Background

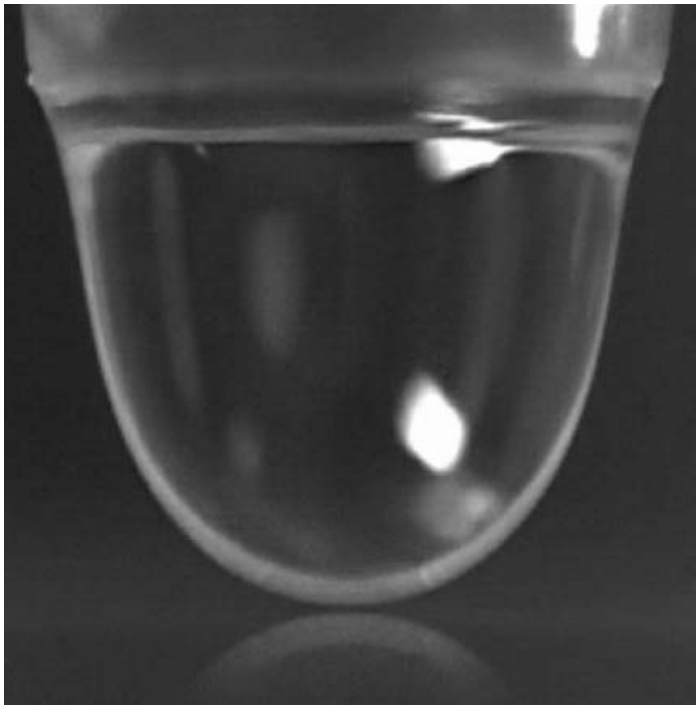

Figure 3-1: The static shape of a pendent water drop. The nozzle is about 5 mm in diameter.

3.1 Initial static shapes of drops

In the absence of other forces, surface tension will shape the drop into a perfect sphere. However, gravity introduces a balance between hydrostatic pressure inside the drop and capillary pressure caused by the surface curvature. Due to the direction of gravity, drops are distorted differently depending on their orientation with respect to gravity. The pendent drop, hanging from a nozzle, is stretched while the bottom sessile drops, sitting on a flat plate, or a non-wetting nozzle, become flatter than a sphere. The extent of this deformation is characterized by a length-scale, i.e. the so-called '*capillary length'* for a particular liquid

$$a = \left(\frac{\sigma}{\rho g} \right)^{1/2}$$

Where σ is the surface tension coefficient ρ is the liquid density and g is gravity. For drop radius $R > a$, gravity will cause significant deviations from spherical form. The initial drop shape and drop radius of curvature are important information for further measurement and calculation. Our images allow us to measure the initial shape precisely, except at the very tip of the drop, where the first contact occurs. At this very tip, the drop has always made contact in the first image due to fixed time delay associated with the triggering and recording system making it impossible to get the initial drop shape precisely at the tip. This is a rather small area and does not cause much error in the later images.

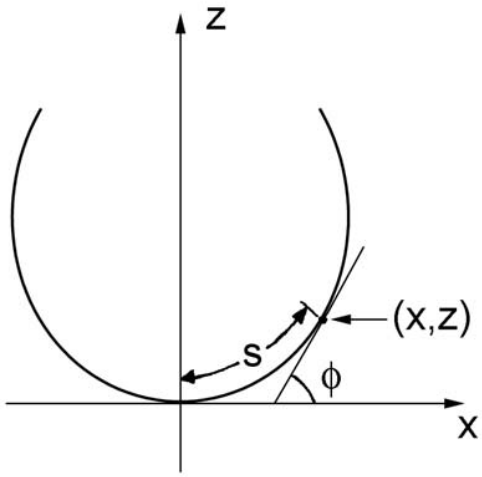

Figure 3-2: The coordinate system used to derive the equations used to determine static drop shapes.

For precise characterization of the initial static drop shapes, we have numerically solved the differential equations describing these shapes, using the method described by Fordham (1948). The method was originally proposed to evaluate σ from images of pendent drop shapes. The static drop is in a balance state between hydrostatic pressure ρgz and capillary pressure. Capillary pressure is expressed by the *Young-Laplace* equation in the following equality

$$\sigma\left(\frac{1}{R_1}+\frac{1}{R_2}\right)=P_{in}-P_{out} \tag{3-1}$$

where R_1 and R_2 are the principal radii of curvature of the free surface, P_{out} is the ambient atmospheric pressure and P_{in} is the pressure just inside the surface of the drop on the liquid side. The pressure inside the liquid at the bottom tip of the drop is determined solely by the bottom radius of curvature, as $z=0$ and $R_1=R_2$, $P_{tip}=R_t/2\sigma$. Here, we distinguish the tip radii of curvature for the top drop and for the bottom drop with symbol R_t and R_b. Working in terms of gauge pressure, P_{out} is set to zero and the hydrostatic pressure varies with the height inside the top drop, the function of inside pressure with respect to height is given by

$$P_{in}=\frac{2\sigma}{R_t}-\rho gz$$

Substituting this relation into above equation and dividing each term by σ, we get

$$\frac{1}{R_1}+\frac{1}{R_2}=\frac{2}{R_t}-\frac{\rho gz}{\sigma}$$

Next, all lengths in the above equation are normalized by the unknown tip curvature R_t or R_b

$$\frac{1}{R_1/R_t}+\frac{1}{R_2/R_t}=2-\frac{\rho gR_t^2}{\sigma}\frac{z}{R_t}$$

The ratios of two principal radiuses of curvature R_1 and R_2 over tip curvature R_t are denoted as $1/\kappa$ and $R/\sin\phi$, in which $1/\kappa$ is the radius of curvature at point (*r, z*) along the free surface, calculated in the *z*-direction and ϕ is the slope of the free surface. The non-dimensional number, Bond number, is here denoted by $\beta=\frac{\rho gR_t^2}{\sigma}$.

The sign of this number changes with the orientation of drop with respect to gravity. So the above equation can be expressed in cylindrical coordinates as

$$\kappa + \frac{\sin\phi}{R} = 2 + \beta z \tag{3-2}$$

where κ, β and ϕ are functions of the arclength. These equations are expressed in terms of arclength s along the drop surface and result in a set of three differential equations:

$$\frac{dR}{ds} = \cos\phi, \quad \frac{dz}{ds} = \sin\phi, \quad \frac{d\phi}{ds} = 2 + \beta z - \frac{\sin\phi}{R}$$

This set of ODEs is solved by integrating them along the arclength with the Runge-Kutta method starting from the tip of drop. To find the value of R_t, a range of values are tried using a shooting method, based on an initial guess of R_t. This allows us to find the best value of R_t which gives the minimum least-square difference between calculated drop shape and the drop shape obtained from the experimental images.

3.2 Coalescence of liquid wedges

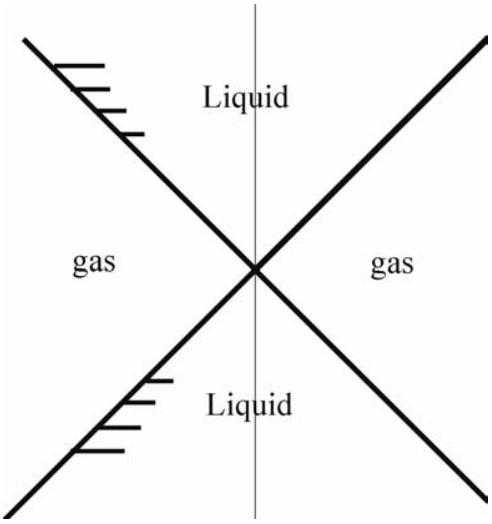

Figure 3-3: The theoretical setup used by Keller and Miksis (1983).

The theoretical and numerical treatment of coalescence of liquid wedges was done by Keller & Miksis (1983). In their study, two types of configurations are considered, one modeling the breaking up of a sheet of liquid and the other simulating the interface motion of a free surface of a liquid spreading on a solid. The former setup is shown in figure 3-3. Despite the fact that it is not a common physical situation, they found that the solution of this problem is self-similar, which reduces the number of independent variables by one and simplifies the numerical solution.

To get the group of equations describing the coalescence of liquid wedges, first let $\phi(x,y,t)$ be the potential function of the flow of the liquid and $F(x,y,t)$ be the free surface of the liquid. The equations satisfied by $\phi(x,y,t)$ and $F(x,y,t)$ are Laplace's equations in the fluid

$$\nabla^2\phi = 0$$

and the kinematic and dynamic boundary conditions on the free surface, which state that a fluid element on the surface remains on the surface. The second expression is the unsteady Bernoulli equation:

$$F_t + \nabla\phi \cdot \nabla F = 0$$
$$\phi_t + \frac{1}{2}(\nabla\phi)^2 + (\sigma/\rho)\kappa = 0 \quad \text{on } F = 0$$

where κ is the curvature of the surface, counted positive when the surface is concave toward the fluid. And the free surface of the flow should also satisfy the following boundary and initial conditions

$\phi_y = 0, y = 0$ (the rigid surface)

$F(x, y, 0) = y\cos\theta_0 - x$ (initial position of free surface is a straight line on $x - y$ plane)

$\phi = 0, x^2 + y^2 \to \infty$ (the fluid is at rest at infinity)

$-F_x / F_y = \tan\beta$ at $y = 0$, $F(x, 0, t) = 0$ for $t > 0$

Here β is the angle at the point of free surface touching the rigid surface, which can be related to the wedge angle. Dimensional analysis showed that the solution should be a function of dimensionless combination of x, y and t, and two independent combinations ξ and η were postulated, which are defined by

$$\xi = x\left(\frac{\rho}{\sigma t^2}\right)^{1/3}, \eta = y\left(\frac{\rho}{\sigma t^2}\right)^{1/3} \tag{3-3}$$

And ϕ, F are expressed in terms of ξ and η

$$\phi(x, y, t) = \left(\sigma^2 t/\rho^2\right)^{1/3} \varphi(\xi, \eta)$$
$$F(x, y, t) = \left(\rho/\sigma t^2\right)^{-1/3} G(\xi, \eta)$$

with the dimensionless variable G, the equation satisfying kinematic condition is transform to

$$\frac{dF(x, y, t)}{dt} = G\frac{d}{dt}\left(\frac{\rho}{\sigma t^2}\right)^{-1/3} + \left(\frac{\sigma t^2}{\rho}\right)^{1/3}\frac{dG}{dt}$$

$$\frac{dG}{dt}=\frac{\partial G(\xi,\eta)}{\partial \xi}\frac{\partial \xi}{\partial t}+\frac{\partial G(\xi,\eta)}{\partial \eta}\frac{\partial \eta}{\partial t}$$

$$\frac{\partial \xi}{\partial t}=\frac{d}{dt}\left(\rho/\sigma t^2\right)^{1/3}x=-\frac{2}{3}x\left(\frac{\rho}{\sigma}\right)^{1/3}t^{-5/3}$$

$$\frac{\partial \eta}{\partial t}=-\frac{2}{3}y\left(\frac{\rho}{\sigma}\right)^{1/3}t^{-5/3}$$

So

$$\frac{dF(x,y,t)}{dt}=G\frac{d}{dt}\left(\frac{\rho}{\sigma t^2}\right)^{-1/3}-\frac{2}{3}t^{-1}\left(xG_\xi+yG_\eta\right)$$

$$\nabla\phi=\left(\frac{\sigma^2 t}{\rho^2}\right)^{1/3}\left(\frac{\partial\varphi}{\partial\xi}\frac{\partial\xi}{\alpha x}+\frac{\partial\varphi}{\partial\eta}\frac{\partial\eta}{\alpha y}+\frac{\partial\varphi}{\partial\xi}\frac{\partial\xi}{\partial y}+\frac{\partial\varphi}{\partial\eta}\frac{\partial\eta}{\partial x}\right)$$

Here

$$\frac{\partial\xi}{\partial x}=\left(\frac{\rho}{\sigma t^2}\right)^{1/3},\frac{\partial\eta}{\partial y}=\left(\frac{\rho}{\sigma t^2}\right)^{1/3}\ and$$

$$\frac{\partial\xi}{\partial y}=0,\frac{\partial\eta}{\partial x}=0$$

Therefore

$$\nabla\phi=\left(\frac{\sigma}{\rho t}\right)^{1/3}\left(\frac{\partial\varphi}{\partial\xi}+\frac{\partial\varphi}{\partial\eta}\right)=\left(\frac{\sigma}{\rho t}\right)^{1/3}\nabla\varphi$$

Similarly

$$\nabla F=\nabla G$$

finally, the equation describing the kinematic boundary condition transforms to

$$F_t+\nabla\phi\nabla F=0,F=0$$

$$\Rightarrow G\frac{d}{dt}\left(\frac{\rho}{\sigma t^2}\right)^{-1/3}-\frac{2}{3}t^{-1}\left(xG_\xi+yG_\eta\right)+\left(\frac{\sigma}{\rho t}\right)^{1/3}\nabla\varphi\cdot\nabla G=0,G=0$$

$$\Rightarrow-\frac{2}{3}\left(\frac{\rho}{\sigma t^2}\right)^{1/3}\left(xG_\xi+yG_\eta\right)+\nabla\varphi\cdot\nabla G=0,G=0$$

$$\Rightarrow-\frac{2}{3}\left(\xi G_\xi+\eta G_\eta\right)+\nabla\varphi\cdot\nabla G=0,G=0$$

Next the Bernoulli equation

$$\phi_t + \frac{1}{2}(\nabla\phi)^2 + (\sigma/\rho)\kappa = 0$$

As before

$$\nabla\phi = \left(\frac{\sigma}{\rho t}\right)^{1/3}\left(\frac{\partial\varphi}{\partial\xi} + \frac{\partial\varphi}{\partial\eta}\right) = \left(\frac{\sigma}{\rho t}\right)^{1/3}\nabla\varphi \Rightarrow \frac{1}{2}(\nabla\phi)^2 = \frac{1}{2}\left(\frac{\sigma}{\rho t}\right)^{2/3}(\nabla\varphi)^2$$

The time derivative of the velocity potential is transformed

$$\frac{\partial\phi(x,y,t)}{\partial t} = \left(\frac{\sigma}{\rho}\right)^{2/3}\frac{\partial}{\partial t}\left(t^{1/3}\varphi(\xi,\eta)\right) = \left(\frac{\sigma}{\rho}\right)^{2/3}\left(\frac{1}{3}t^{-2/3}\varphi(\xi,\eta) + t^{1/3}\frac{\partial}{\partial t}\varphi(\xi,\eta)\right)$$

The time derivative is now carried through into the argument of φ

$$\frac{\partial}{\partial t}\varphi(\xi,\eta) = \frac{\partial\varphi}{\partial\xi}\frac{\partial\xi}{\partial t} + \frac{\partial\varphi}{\partial\eta}\frac{\partial\eta}{\partial t},$$

where

$$\frac{\partial\xi}{\partial t} = \frac{d}{dt}\left(\rho/\sigma t^2\right)^{1/3}x = -\frac{2}{3}x\left(\frac{\rho}{\sigma}\right)^{1/3}t^{-5/3} = -\frac{2}{3}\xi\frac{1}{t}$$

$$\frac{\partial\eta}{\partial t} = -\frac{2}{3}y\left(\frac{\rho}{\sigma}\right)^{1/3}t^{-5/3} = -\frac{2}{3}\eta\frac{1}{t}$$

therefore

$$\frac{\partial}{\partial t}\varphi(\xi,\eta) = -\frac{2}{3}\nabla\varphi\cdot(\xi,\eta)\frac{1}{t}$$

Substituting into equation we end up with

$$\frac{\partial}{\partial t}\phi(x,y,t) = \left(\frac{\sigma}{\rho}\right)^{2/3}\frac{1}{3}t^{-2/3}\varphi + t^{1/3}\left(-\frac{2}{3}\nabla\varphi\cdot(\xi,\eta)\frac{1}{t}\right) = \left(\frac{\sigma}{\rho}\right)^{2/3}\left(\frac{1}{3}\varphi - \frac{2}{3}\nabla\varphi\cdot(\xi,\eta)\right)$$

Combining all these terms into the Bernoulli equation we get

$$-\frac{2}{3}\left(\xi G_\xi + \eta G_\eta\right) + \frac{1}{2}(\nabla\varphi)^2 + \frac{1}{3}\varphi + \frac{\sigma}{\rho}\left(\frac{\rho t}{\sigma}\right)^{2/3}\kappa = 0$$

The last term becomes

$$\left(\frac{\sigma t^2}{\rho}\right)^{1/3}\kappa = \frac{y}{\eta}\kappa$$

which convert κ in $x-y$ coordinate into κ in $\xi-\eta$ coordinate.

So the set of equation and corresponding boundary conditions are converted into

$$\nabla^2\varphi = 0$$

$$-\frac{2}{3}\left(\xi G_\xi + \eta G_\eta\right) + \nabla\varphi\cdot\nabla G = 0 \quad \text{on} \quad G = 0,$$

$$-\frac{2}{3}\left(\xi\varphi_\xi + \eta\varphi_\eta\right) + \frac{1}{2}\left(\nabla\varphi\right)^2 + \frac{1}{3}\varphi + \kappa = 0 \quad \text{on} \quad G = 0,$$

$$\varphi_\eta = 0 \quad \text{on} \quad \eta = 0, \quad G \sim \eta\cos\theta_0 - \xi \quad \text{at} \ \infty, \quad \varphi \sim 0 \quad \text{at} \ \infty,$$

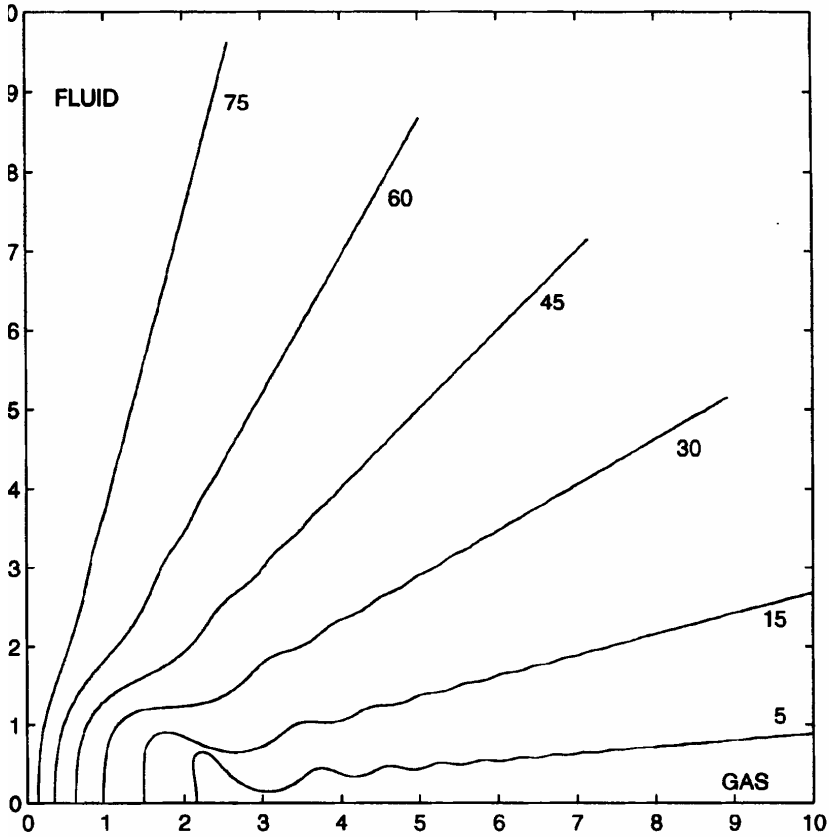

Figure 3-4: The self-similar shapes of coalescing wedges of fluid. Modified from Keller et al. (2000).

$$-G_\xi / G_\eta = \tan\beta \quad \text{at} \ \eta = 0, \quad G(\xi,0) = 0$$

This set of equations can be solved numerically, as was done by Keller and Miksis (1983) to give the surface profiles in figure 3-4. Note that for each wedge-angle there is only one surface profile, which grows in size according to the scaling laws, but does not change in shape. Similar profiles are shown by Keller *et al.* (2000, 2003).

This theory suggests the form of self-similar power-laws, which will be tested on the experimental results in a later section.

3.3 Film spreading

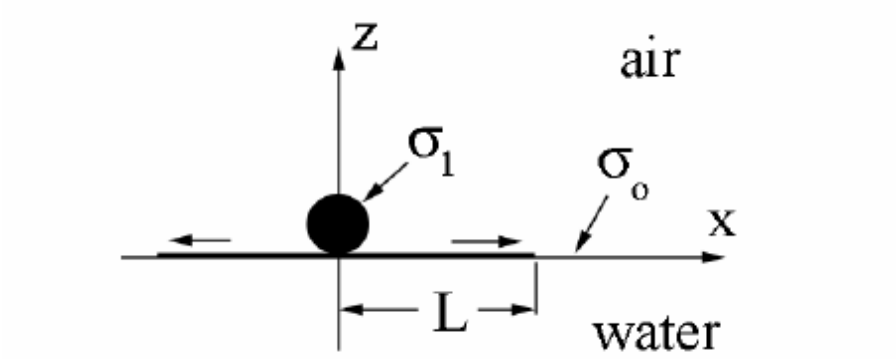

Figure 3-5: The two dimensional setup by Joos & Pintens (1977).

The experiments on coalescence of water and alcohol drops lead to the so-called Marangoni stresses, where the difference in the value of the surface tension generates pulling along the surface, from the liquid with the weaker surface tension to the one with the stronger surface tension. This stress accelerates the liquid next to the surface generating a boundary layer under the surface. The viscous stress in this boundary layer will balance the Marangoni stress. Many theories have looked at this phenomenon. Most of this theoretical work looks at the spreading of surfactants and not of two miscible liquids, as is studied herein. However, some are quite relevant

and here we will look at the early ones, which give the general idea of how these forces and dynamics can be characterized.

The simplest theoretical model of a surfactant spreading on a flat surface is probably that of Joos & Pintens (1977), where they treat the two-dimensional problem. Figure 3-5 shows the setup, where a rod of surfactant solution, with surface tension σ_1, makes contact with a flat water surface, which has a higher surface tension of $\sigma_0 > \sigma_1$. The spreading of the surfactant is driven by Marangoni stresses, as the water has higher surface tension than the surfactant solution, pulling it outwards along the surface. The gradient of the surface tension represents an unbalanced stress, which will accelerate the free surface, until it reaches balance with the viscous stress in the boundary layer under the film, due to the gradient of the horizontal velocity u with depth z. This balance can be written, at the free surface $z = 0$,

$$\frac{d\sigma}{dx} = \mu \frac{du}{dz} \tag{3-4}$$

where μ is the dynamic viscosity. Notice, that in writing this equation we have ignored the inertia of the fluid, which has to be accelerated with the film. The simplest approximation for the surface tension gradient is to assume it changes from σ_1 at the origin to σ_0 at the tip of the spreading film $x = L$. We call $\Delta\sigma = \sigma_1 - \sigma_2$, giving

$$\frac{d\sigma}{dx} = \frac{\Delta\sigma}{L}$$

The velocity is now assumed to take an exponential form, from the value $u(x, z = 0, t)$ at the surface

$$u(x, z, t) = u(x, 0, t)\exp(z / \delta); \quad \delta = \sqrt{vt}$$

where the depth of the boundary layer is approximated as the viscous length scale. As $z \to -\infty$ we see that $u \to 0$.

The next approximation involves the distribution of the horizontal velocity at the film surface. Here they assume the motion is in *uniform expansion*, which is expressed as

$$u(x,0,t) = \frac{x}{L}\frac{dL}{dt}$$

which means the velocity changes linearly from zero at the origin $x = 0$ and becomes the same as the spreading speed of the film at its tip, i.e. $u = dL/dt$ at $x = L$. Substituting this into the previous equation we get for the velocity

$$u(x,z,t) = \frac{x}{L}\frac{dL}{dt}\exp(z/\delta)$$

which we can use to find the shear stress under the surface

$$\frac{du(x,z,t)}{dz} = \frac{d}{dz}\left(\frac{x}{L}\frac{dL}{dt}\exp(z/\delta)\right) = \frac{x}{L}\frac{dL}{dt}\frac{1}{\delta}\exp(z/\delta)$$

This we evaluate at the surface by setting $z = 0$ and substitute into the original equation,

$$\frac{\Delta\sigma}{L} = \mu\frac{1}{\sqrt{vt}}\frac{x}{L}\frac{dL}{dt} = \sqrt{\frac{\mu\rho}{t}}\frac{x}{L}\frac{dL}{dt}$$

We now evaluate this equation at the front of the film, at $x = L$ and integrate to find $L(t)$. We search for a power-law expression, i.e. $L(t) = Ct^{\alpha}$

$$\frac{\Delta\sigma}{Ct^{\alpha}} = \sqrt{\frac{\mu\rho}{t}}\frac{d(Ct^{\alpha})}{dt} \Rightarrow t^{-\alpha}t^{1/2}t^{1-\alpha} = \frac{C^2\alpha\sqrt{\mu\rho}}{\Delta\sigma}$$

Giving $\alpha = 3/4$ and $C^2 = \Delta\sigma/(\alpha\sqrt{\mu\rho})$ giving the solution

$$L(t) = \sqrt{\frac{4\Delta\sigma}{3}}\frac{1}{(\mu\rho)^{1/4}}t^{3/4} \qquad (3\text{-}5)$$

The speed of the edge can now be found by differentiating this relationship,

$$u(x = L,0,t) = \frac{dL(t)}{dt} = \sqrt{\frac{4}{3}}\frac{3}{4}\frac{\Delta\sigma}{(\mu\rho)^{1/4}}t^{-1/4} = \sqrt{\frac{3}{4}}\frac{\Delta\sigma}{(\mu\rho)^{1/4}}t^{-1/4} \qquad (3\text{-}6)$$

What this relationship shows is that the velocity approaches infinity at the earliest times. However, as stated above, the assumptions above ignore the inertia of the liquid, which will certainly be important during the initial motions. For very early times, the balance might be capillary-inertial, not capillary-viscous.

This relationship also shows that the speed depends linearly on the strength of the surface-tension difference $\Delta\sigma$. Suciu *et al.* (1970) measured this dependence using a miscible drop on a flat water surface. They followed small discs on the water surface using stroboscopic imaging to get the surface velocity. The discs were 2 mm in diameter, getting measurements as close as 7 mm from the first contact. They used a regular film camera and a rotating disc placed in front of the camera. This disc had an 36° open sector, which allowed intermittent exposure of the disc during its motion. They then extrapolated these measurements to zero, getting an initial velocity for a number of liquids, which follows approximately the relationship

$$U_0 = 0.04 \times \frac{d\sigma}{dC}$$

where U_0 is in ms^{-1} and $\Delta C \times (d\sigma / dC)$ in dyn/cm. For ethanol on water this gradient takes a value of 15 dyn/cm, which gives an initial velocity of

$$U_0 = 0.04 \times 15 = 0.6 ms^{-1}$$

This value can be compared to our data.

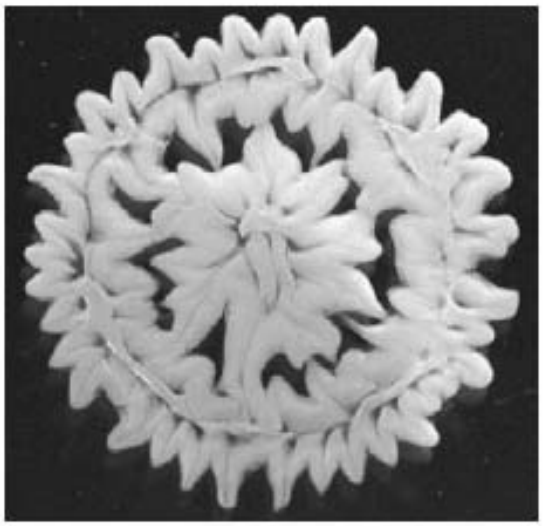

Figure 3-6: Manrangoni instability on the edge of a water drop sitting on top of a layer of glycerin by Tan & Thoroddsen (1998a,b).

A more detailed model by Ruckenstein *et al.* (1970) carried out a more detailed analysis of the flow problem, in the axisymmetric configuration. However, their setup was for the steady situation of a drop sitting on the surface of the water, being fed continuously through a tube. The geometry here is therefore set as a lens of surfactants having a radius of r_0.

This is similar to the situation in Tan & Thoroddsen (1998b), where a drop of water sits on top of a layer of glycerin. The Marangoni-driven flows are in this case unstable to azimuthal instabilities, forming a flower-like pattern, shown in Tan & Thoroddsen (1998a), reproduced in figure 3-6.

Using cylindrical coordinates, the advection diffusion equation takes the form

$$u\frac{\partial c}{\partial r}+v\frac{\partial c}{\partial z}=D\left(\frac{\partial^2 c}{\partial z^2}+\frac{1}{r}\frac{\partial}{\partial r}\left(r\frac{\partial c}{\partial r}\right)\right)$$

where D is the diffusivity of the scalar, or one liquid in the other. In our case this would be the diffusivity of ethanol in water. The horizontal momentum equation is

$$u\frac{\partial u}{\partial r}+v\frac{\partial u}{\partial z}=\nu\left(\frac{\partial^2 u}{\partial z^2}+\frac{\partial^2 u}{\partial r^2}+\frac{1}{r}\frac{\partial u}{\partial r}-\frac{u}{r^2}\right)$$

As they have assumed axisymmetry, there is no azimuthal momentum equation. They have also assumed that the vertical velocities are small enough to ignore. Finally the continuity equation has the form

$$\frac{1}{r}\frac{\partial}{\partial r}(ru)+\frac{\partial v}{\partial y}=0$$

These equations have to be solved with the appropriate boundary conditions. These boundary conditions are applied at the free surface

$$y=0\Rightarrow v=0;\quad \frac{\partial c}{\partial z}=0;\quad \frac{\partial u}{\partial z}=-\frac{1}{\mu}\frac{\partial \sigma}{\partial r}$$

which assumes no vertical motion of the interface and no flux of ethanol into the air. This may not be very accurate, as ethanol is very volatile liquid. The last equality represents a balance between the Marangoni stress and the viscous stress, like is used in the previous subsection.

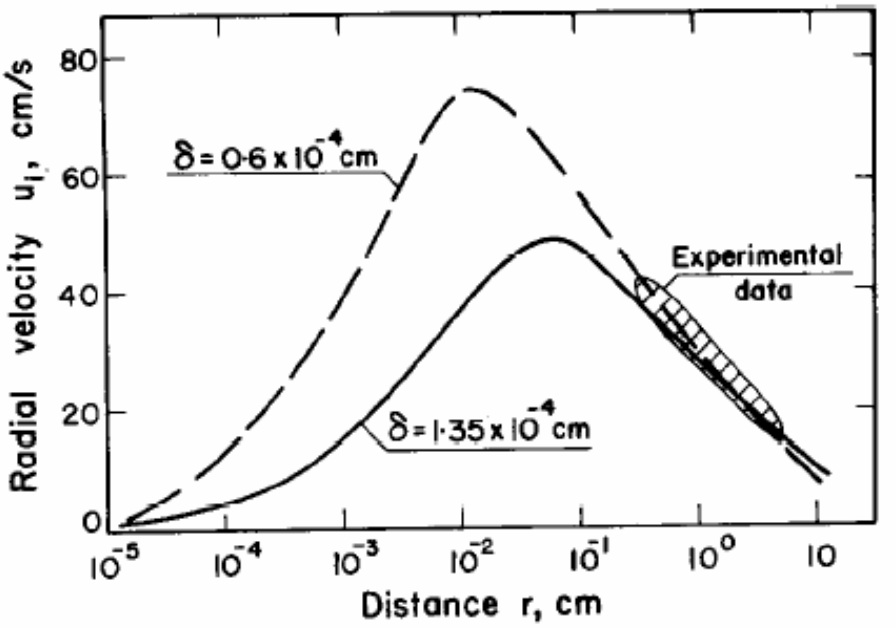

Theoretical velocity distribution for the case of pure isobutanol–pure water system.

Figure 3-7: Solution for the free-surface velocity obtained by Ruckenstein *et al.* (1970).

The boundary conditions at the edge of the drop $r = r_0$, they assume

$$r = r_0 \Rightarrow u = 0; \quad c = c_0 \quad for \quad 0 < z < \delta; \quad c = 0 \, for \quad \delta < z < \infty$$

and the disturbances decay away from the interface

$$z \to \infty \Rightarrow u = v = 0; c = 0$$

Now, as $v << u$ they use this to simplify the advection/diffusion equation and ignore all but the first terms on the right hand side of these equations. This leaves the following equations

$$u_i \frac{\partial c}{\partial r} = D \frac{\partial^2 c}{\partial z^2}$$

$$u_i \frac{\partial u}{\partial r} = v \frac{\partial^2 u}{\partial z^2}$$

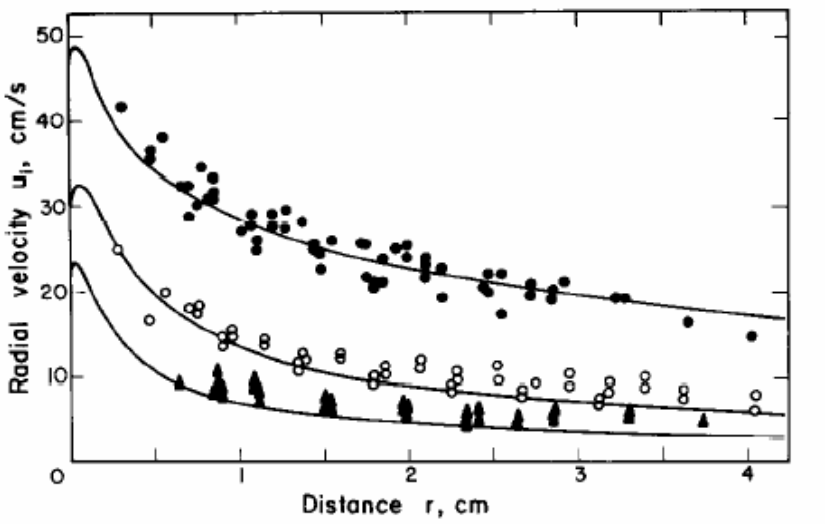

Comparison between theoretical and experimental velocity distributions computed with $\delta = 1{\cdot}35 \times 10^{-4}$ cm.

Systems: ● pure isobutanol–pure water;
○ pure isobutanol–aq. 2·8 per cent isobutanol sol.;
▼ pure isobutanol–aq. 5·25 per cent isobutanol sol.;
– theoretical curves (computed with $\delta = 1{\cdot}35 \times 10^{-4}$ cm).

Figure 3-8: Solution for the free-surface velocity obtained by Ruckenstein *et al.* (1970).

where the authors have assumed that the first u-velocity can be approximated by its value at the free surface $u = u_i$, while still retaining a non-zero velocity gradient to supply the viscous stress.

These equations are then solved by introducing a new variable

$$t = \int_{r=r_0}^{r} \frac{dr}{u_i}$$

Figures 3-7 and 3-8 show the results for the surface velocities. The maximum velocities observed and predicted are of the order of 60 cm/s.

This theoretical treatment includes an empirical determination of the thickness δ. It is interesting to note that the value of this δ is of the order of 1 μm.

This may explain why it is very difficult to observe the fluorescent in our fluorescence experiments during the water/alcohol coalescence.

More recent studies of the spreading of a surfactant on a layer of liquid are many, but most concentrate on the spreading of a surfactant, which comes in contact with a flat liquid. High-quality experimental work for surfactant spreading includes that of Dussaud and Troian (1998) and Santiago-Rosanne, Vignes-Adler and Velarde (1997). Both of these studies use small drops deposited onto a flat liquid surface.

The theoretical treatment of the spreading problem is reviewed in great detail by Jensen (1995), where many more references are given.

4 Experimental Setup

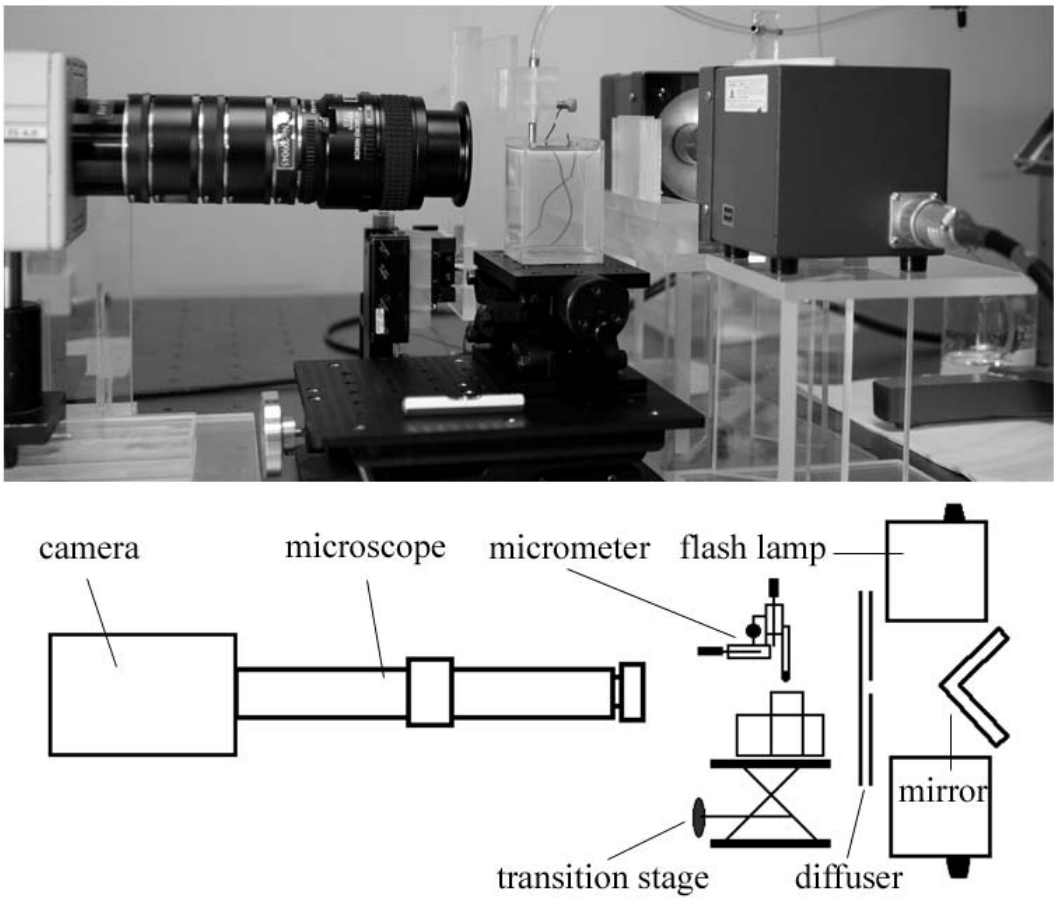

Figure 4-1: Experimental setup.

Figure 4-1 shows the basic experimental setup, which mainly includes the nozzle used to generate the drop, the image recording system, the optical setup used to magnify the region of interest, as well as the illumination sources. To reduce the oscillations of the surrounding environment and fix the aligned optics the whole setup was placed on to a large optical table. This was necessary to make the experiments repeatable, with the coalescence occurring approximately at the same spatial location.

4.1 Drop setup

To investigate the surface shapes of a drop coalescing onto a flat liquid surface, a circular acrylic cell with outside diameter of about 4 cm was prepared. This cylinder was filled to the rim to produce a flat liquid surface. It was put on a micro-transition stage to change the vertical position of the liquid surface in the field of view of the microscope. Due to the reflection and refraction problems across the wall of the bottom cell, which blurs or even blocks the view of coalescence motion near the liquid surface, the reservoir was always slightly overfilled. To reduce possible distortion of the image caused by the microscope not being absolutely vertical to the plane of the coalescence, the position of bottom liquid surface was kept around the centre of the field of view, so that initial coalescence motion always took place at the center. In a few cases when observing the wave motion underneath the original drop surface during drop coalescence, a different container was built, to avoid the optical distortion induced by the curved bottom cell. This square acrylic container had dimensions of 5 cm x 5 cm in cross-section and was 6 cm tall. It was partially filled to produce a flat liquid surface.

The pendant drop was grown at the end of a stainless-steel tube. The drop size was controlled by changing the tube outside diameter. The top tube was connected to a glassware reservoir via a plastic tube and held by a stainless-steel supporting arm. The tube position was adjusted vertically and horizontally via a 3-dimensional micrometer stage. To keep the tube perpendicular to the bottom liquid surface, a small level was used to monitor the horizontal position of its support arm. One of the aims of this project was to investigate the effects of drop size on the coalescence. This was accomplished using different size needles/tubes. Three sets of metallic needles made from stainless-steel tubes and one syringe needle were used in the experiments herein.

Their outside diameters were 0.88, 1.85, 2.95 and 4.75 mm. The contact line of the drop would stick to the outer edge of these tubes, so the OD determines the size of the drop and the ID is of little significance.

For studying the coalescence of two widely differently sized drops, a slight modification was made to the above experimental setup. The sessile drops at the bottom were generated with very small needles. Two different needles of outside diameter of 0.4 mm and 0.88mm respectively were selected for those experiments. The bottom needles were connected to a syringe which presses liquid out through the tube and a drop formed at the tip of the needle. And the bottom needle was fixed onto a translation stage which could only vary the vertical position whereas the horizontal position was fixed. The top pendent drop was generated with a tube of 4.75 mm in diameter and its position was adjusted with a 3-dimensional micrometer stage to allow the drops to meet at the midpoint of the camera view.

4.2 Camera and system hub

For the purpose of taking high quality pictures of the coalescence motions, a 4 megapixel digital camera (Redlake Megaplus ES4.0) was employed to record sets of two images for each coalescence event. Its high resolution, spatial resolution 2048 x 2048 and 12-bit progressive scan readout, gave us the power to see finer details. Its high sensitivity also allowed us to see important details under low-light condition. Besides, it provided a low noise output with consistently uniform response across the image. Although the slow frame rate of this camera (15 frame per second at full pixels) did not allow us to observe the entire evolution of a coalescence event in one experiment, its double exposure imaging mode enabled us obtain a pair of images for each coalescence event and resolve the whole initial coalescence motion by taking a

series of pictures using different delay times. It is therefore important to keep the conditions for many subsequent drops as much the same as possible. The camera is easy to use with the control software and the dedicated computer via a cable and frame grabber board. In the experiment, a PIV system hub from *Dantec* was used to coordinate the camera and illuminating source and detect the external trigger signal, which indicates the liquid contact. Its internal operating mechanism frees us from the complicate relationship between different time delay devices. The only thing required is to define devices from device libraries for each component. These libraries describe some characteristics of the particular device. The system hub can then automatically synchronize these devices. Another advantage of using the PIV system hub is its multiple control options. It is easy to adjust the time interval between the pair of images, change the trigger mode of the camera to choose the external trigger mode.

4.3 Long-distance Microscopic Lens

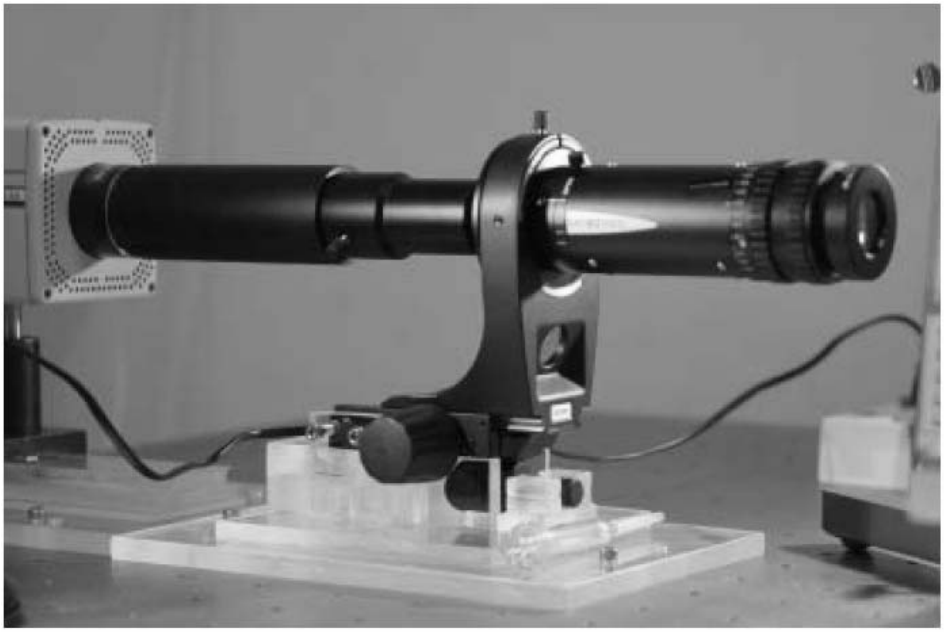

Figure 4-2: Long working distance microscope Leica Z16APO.

Previous experiments have revealed that the initial neck region of coalescence and the capillary/marangoni wave traveling along the drop surface had dimension order of 100 μm, large magnifications are therefore needed. Here we used a long working distance microscope (Leica Z16APO), which consists of a zoom control system and interchangeable objectives. Three different objectives were available, giving basic magnification of 0.5, 1 and 2. Different combinations of zoom selection and magnification objectives allow investigating a field of view from one centimeter to several tens of micrometers with optical resolution of about 1 micrometer. And its superiority in contrast, image sharpness, color fidelity and image precision make it well suited to high-precision inspection. In a few cases low magnification was needed, a Nikon microlens with magnification 1:1 extended with several extension tubes was used since its large aperture (compared with the microscope) allowing more light to enter under very low-light illuminating conditions.

4.4 Lighting

For viewing the evolution of the drop shape during coalescence, the motion was illuminated with backlighting onto a diffuser, thus showing the silhouette of the phenomenon. The PIV camera takes the first frame over a very short duration of a few micro-seconds, while for the second frame the exposure is much longer. This long second exposure is about 65 ms using the double frame imaging mode. This makes it impossible to conduct the experiment under continuous room lighting. Therefore, the experiments must be run in a dark room and intense flash lighting was needed to freeze the surface motions onto the frames. The dual-cavity Ng-Yang pulsed lasers, used for PIV measurements are good candidates for the illuminating source, especially due to the ultra-short light duration of only 1-5 ns for each pulse. However,

the long delay time, about 200 μs, for laser light launching due to the need for the flash-lamps to excite the laser crystals, are a problem. Another problem is that of laser speckles, which make these lasers non-ideal for our particular experiment. The delay time of 180 μs required between activating the flash lamp and opening the Q-switch prevents it from viewing the earliest stages of the coalescence motions. The other

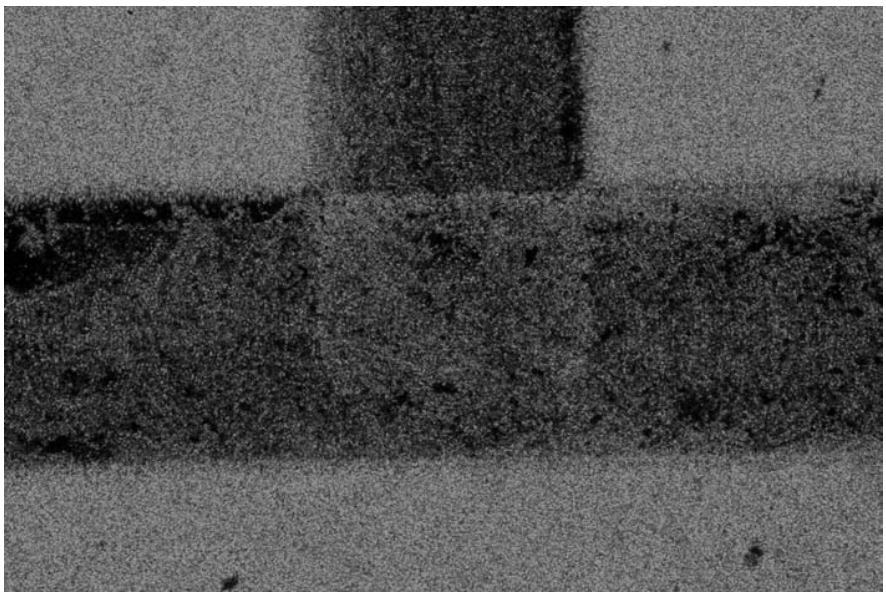

Figure 4-3: Laser speckles caused by high spatial coherence of laser light, the black region is the "T" shape micro-channel with size of 1mm.

disadvantage of laser speckles is the result of the high spatial coherence of laser light. Figure 4-3 shows our attempt at using this lighting. The image is of a micro channel, which was backlit with this laser. The uneven background intensity is quite evident. The image is covered by high contrast random speckle patterns producing unacceptable background noise. These laser speckles could smear out some important details and reduce the overall image quality. Many measures have been proposed to dampen or resolve the laser speckle, but few techniques are suitable for short-pulse duration lasers. These measures were found not to be practical in our project. We

therefore decided to use two xenon flash lamps which have 2-3 μs light duration as illumination sources.

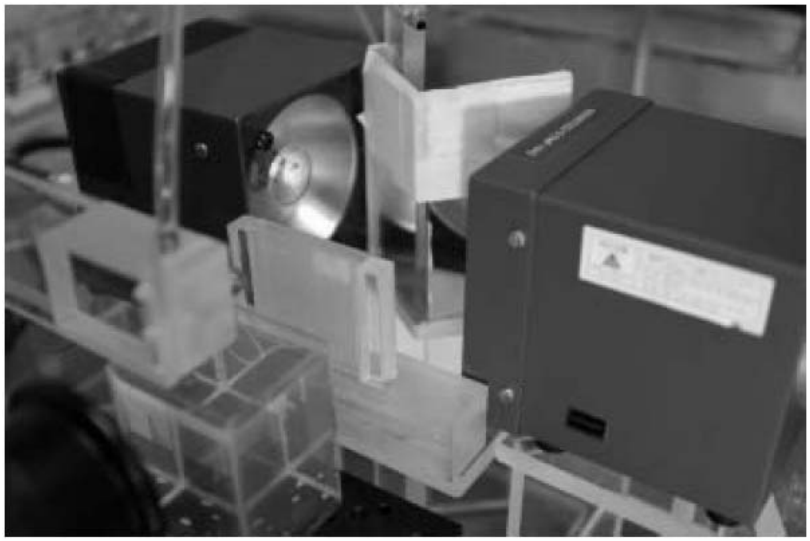

Figure 4-4: Lighting arrangement, which consist of two flash lamps, a reflection mirror and a diffuser.

An illuminated screen was built by combining several different density ground glass diffusers and drafting paper according the needed light intensity. The screen also included a drafting paper with a slit at the center with a size close to the diameter of the tube being used. This mask dampened the light surrounding the drop, which sometimes obscured the edge of the drop, and allowed the center light to become more parallel. This made the drop image sharper. Due to the large dimension of the flash lamp compared to the very small drops, it is difficult to arrange the two flash lamps, such that their light shines directly on the screen, while keeping the lamps close to the diffuser system for high illumination intensity. To reduce the light loss, the two flash lamps were arranged perpendicular to the line of the optical system and a mirror system consist of two mirrors placed between the lamps and the diffuser reflected the light, as shown in figure 4-4.

4.5 Fluorescent imaging

In some of the experiments we tried to identify the borderline between the two different liquids which are coalescing. In these experiments some fluorescent dye was added to the bottom liquid pool and a laser light was used to illuminate the bottom liquid. To keep the CCD camera safe from direct laser light, which can easily be reflected from the drop surface and also to improve the image quality, a band-pass filter (510 nm) was placed in front of the micro lens to block most of the reflecting laser light. To get rid of the rest of laser light, the laser beam was moved a little bit behind the centerline of the drop to limit most of the reflection to the back half of the drop surface. This orientation will also reduce the laser speckles. To make up the loss of light energy due to the dampening factor of the band-pass filter, the two separate laser cavities were triggered and launched at the same time to increase the light input to excite more of the fluorescent molecules and increase the number of photons reaching the camera CCD.

4.6 Contact trigger

To detect the initial liquid contact of the drop with the pool and to start the imaging, an electric contact trigger was designed and fabricated. This trigger senses when the two surfaces touch by sensing the corresponding electrical contact. This trigger circuit was built by the candidate from basic components. The trigger consists of two parts: one converts the electrical change in the circuit to a voltage change and amplifies the signal; anther part regulates the voltage change to standard TTL signal and adjusts the duration of this TTL signal. To get a fast response, a fast response operation amplifier was integrated into the amplified circuit. And to reduce the effect

of surface charge when the drop comes close to the surface, a large resistance was used to limit the contact current to less than 2.5 mA, which also depends on the ion density in the liquid. Therefore, a large amplification factor was needed and some noise screening measure was taken to prevent the noise causing malfunction in the circuit. The second part of the circuit changed the duration of the TTL signals by using chip number 74141 and by changing the combination of a resistor and a capacitor. The total delay of the contact circuit, from first electrical contact to the output TTL signal, was believed less than 5 μs. This was estimated by summing up all the delays in the chips under typical operating conditions.

To make the deionized water conducting, NaCl was added in solution, at a concentration of 1 g/l. For the ethanol solutions, this amount saturated the liquid leaving some of the salt on the bottom of the mixing container. The addition of this salt does not change the surface tension significantly, as it has no surfactant properties. Tables from handbooks suggest that it only increasing σ by less than 2%.

5 Results

5.1 Water drop coalescing with an alcohol pool

Figure 5-1 showed the shape of a water drop coalescing with a flat liquid surface of ethanol/water solution with 94% volume-concentration of ethanol, at times of 900 and 2300 μs from the initial contact. Obvious waves are observed to travel up along the drop surface when the neck region expands during the coalescence. Figure 5-2 highlights the wave motions on the free surface by contrasting the dual images

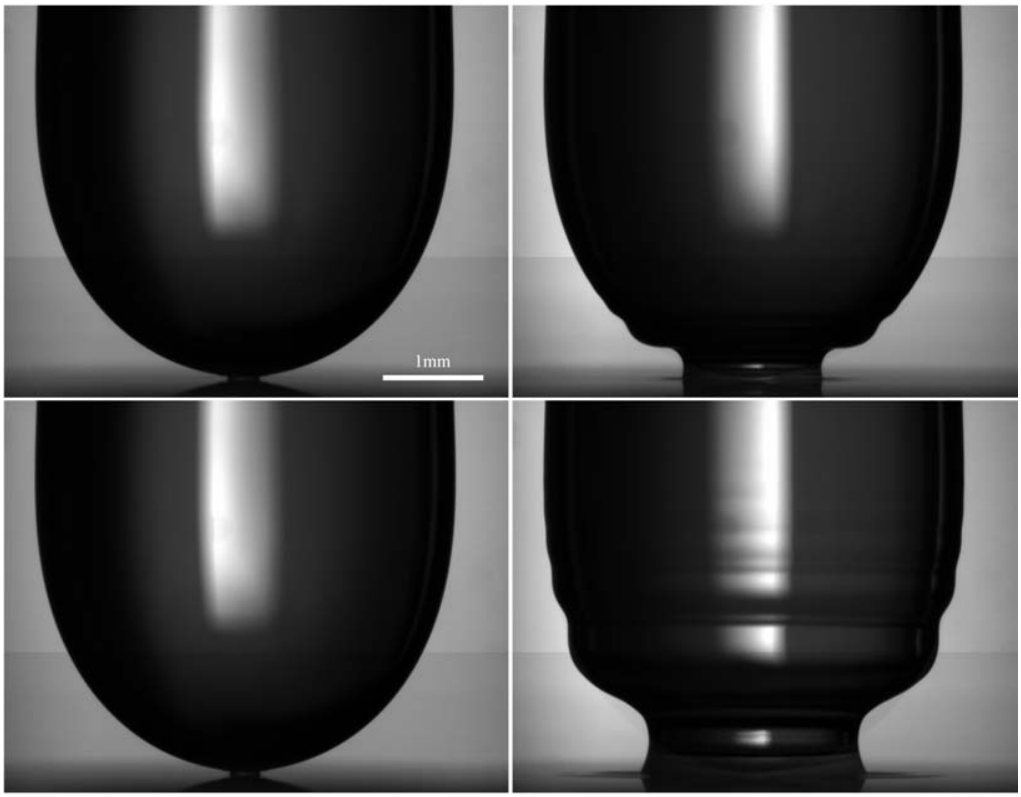

Figure 5-1: The coalescence of DI water drop onto 94% by volume ethanol/water solution in a pool, the left panel show the first contact image and the right panel taken 900 μs (top) and 2300 μs (bottom) respectively after the first contact.

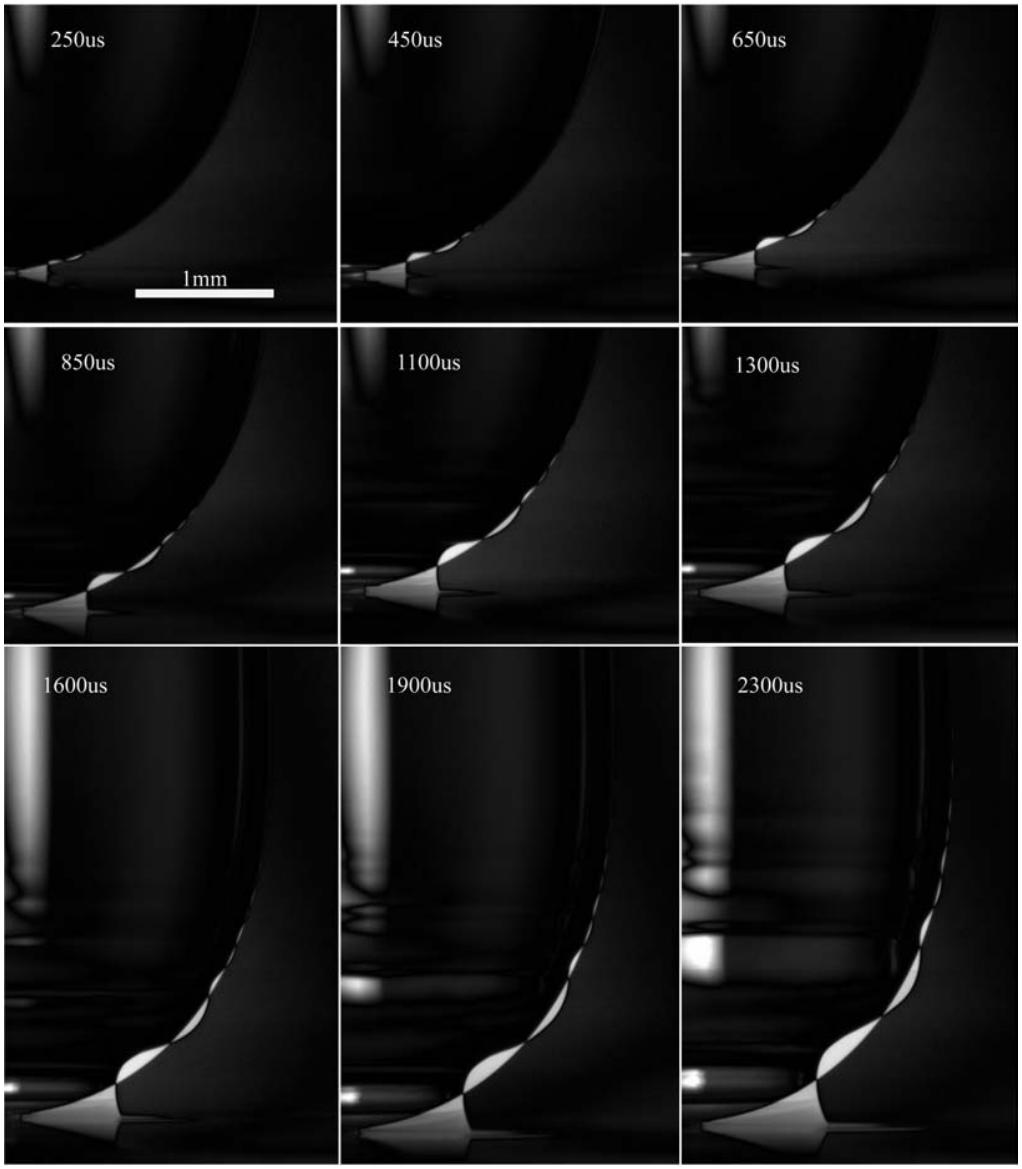

Figure 5-2: The evolution of water drop coalescence with 94% ethanol/water mixture pool, the outside diameter of the tube generating the water drop is 4.75 mm. The 1mm scale bar given in the first panel and the delay time between pair of images indicated in each panel.

taken within one coalescing event. This is done by finding the absolute value of the intensity difference at each pixel in the two images. The sequence of difference images shows the time evolution of the surface of a water drop coalescing with a 94% alcohol solution in the pool, obtained by recording a series of separate drops coalescing, under the same

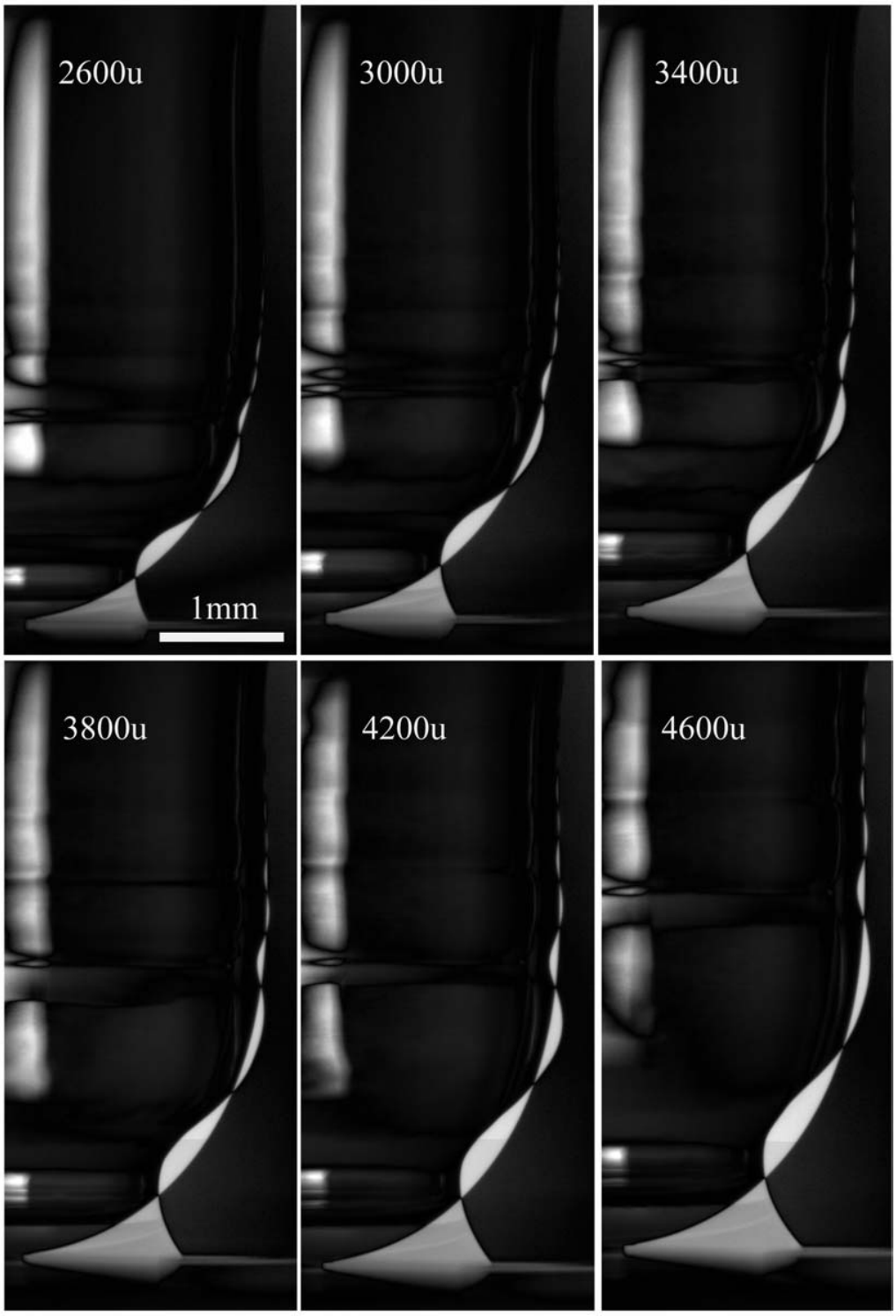

Figure 5-3: Evolution of water drop coalescence with ethanol/water mixture pool with the same setup to figure 5-2 but a smaller magnification scale and at later times after first contact.

experimental conditions. The times listed in the different panels are in μs after first contact of the two liquid surfaces. Note that the initial contact shown in the first frame is about 200 μm in diameter. This is due to the built in time-delay in the imaging system, as discussed in the experimental section. The actual size of the first contact is most likely significantly smaller than this, as we grow the drop very slowly from the nozzle. The lubrication pressure inside the air layer which is being pushed away can deform the very tip of the drop (Jones and Wilson 1978), making the drop touch the bottom along a ring, not at a point, however, for our case this ring should be quite small.

The alcohol solutions used did always consist of 94% ethanol and 6% deionized water. The addition of the water was necessary to dissolve enough NaCl salt for the electrical contact trigger to work properly. Without the water the salt would not dissolve sufficiently for reliable functioning of this trigger.

Figure 5-4 Compares the drop shapes for the coalescence of water onto a pool of water (left panels) and water onto a pool of alcohol (right panels). This comparison shows that larger waves appeared on the drop surface during the water/alcohol coalescence than for that of water/water coalescence. This difference is primarily due to the presence of Marangoni effects for the water/alcohol case. It appears that the waves generated in the water/water coalescence dampen quickly and the amplitude of the leading wave becomes so small that it is difficult to see. This comparison also shows that the speed of coalescence for water/water is considerably faster than that for water/alcohol. This is determined by comparing the diameter of the neck region connecting the two liquid masses.

Figure 5-5 shows similar results for comparison of the coalescence shape between alcohol/alcohol and water/alcohol cases. For the alcohol/alcohol case, there is only one big wave observed close to the neck region and other waves advancing up

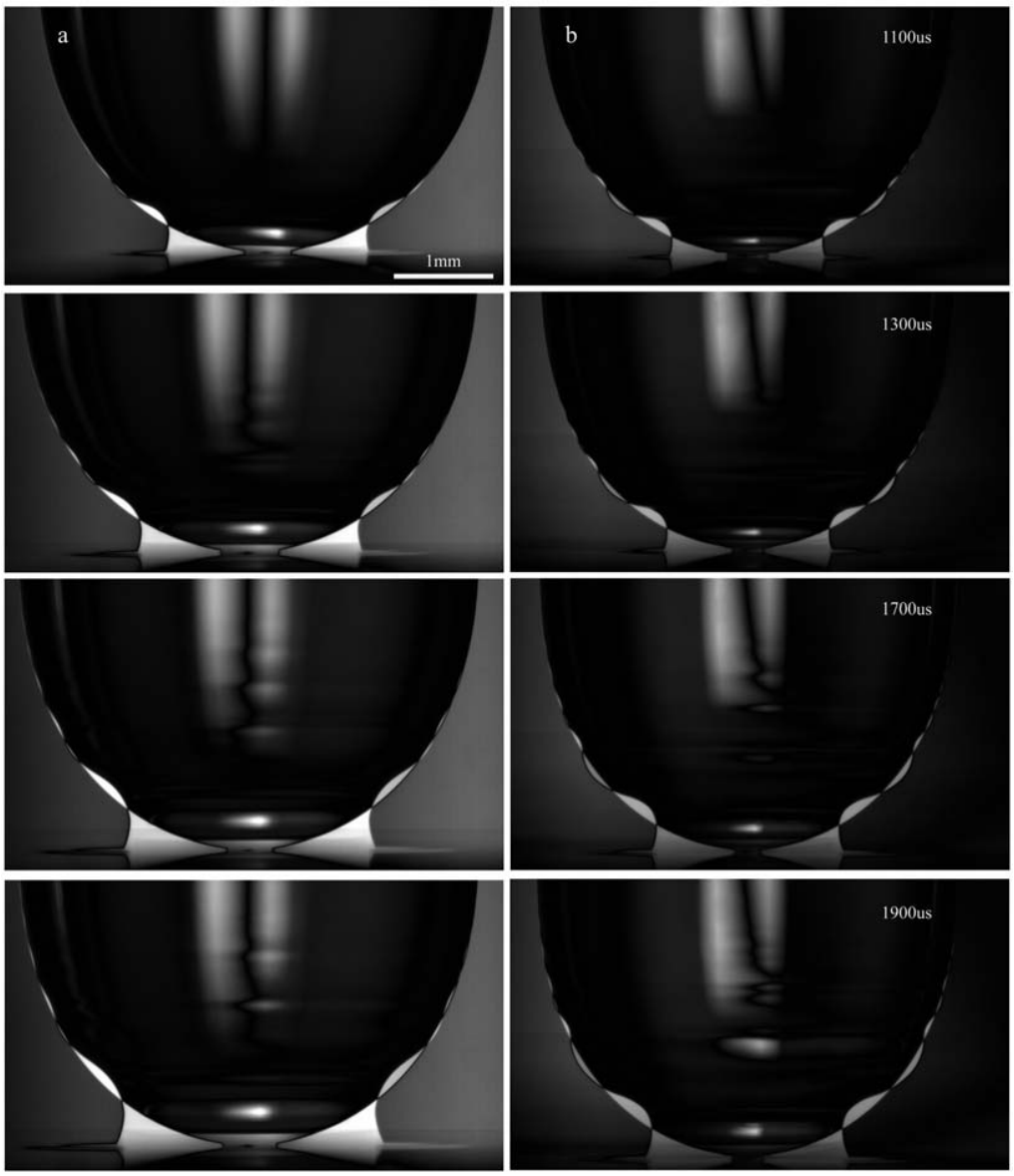

Figure 5-4: Comparison of coalescence evolution of a water drop onto water pool (a) and a water drop onto 94% ethanol/water mixture in the pool. The evolution was highlighted by calculating the difference between a pair of images, the delay time from the second image to the first contact is the same for the left and right images and is given in the right panels.

along the drop surface seem to disappear. The coalescence speeds appear very similar. It is however difficult to compare the coalescence speeds in these two cases directly.

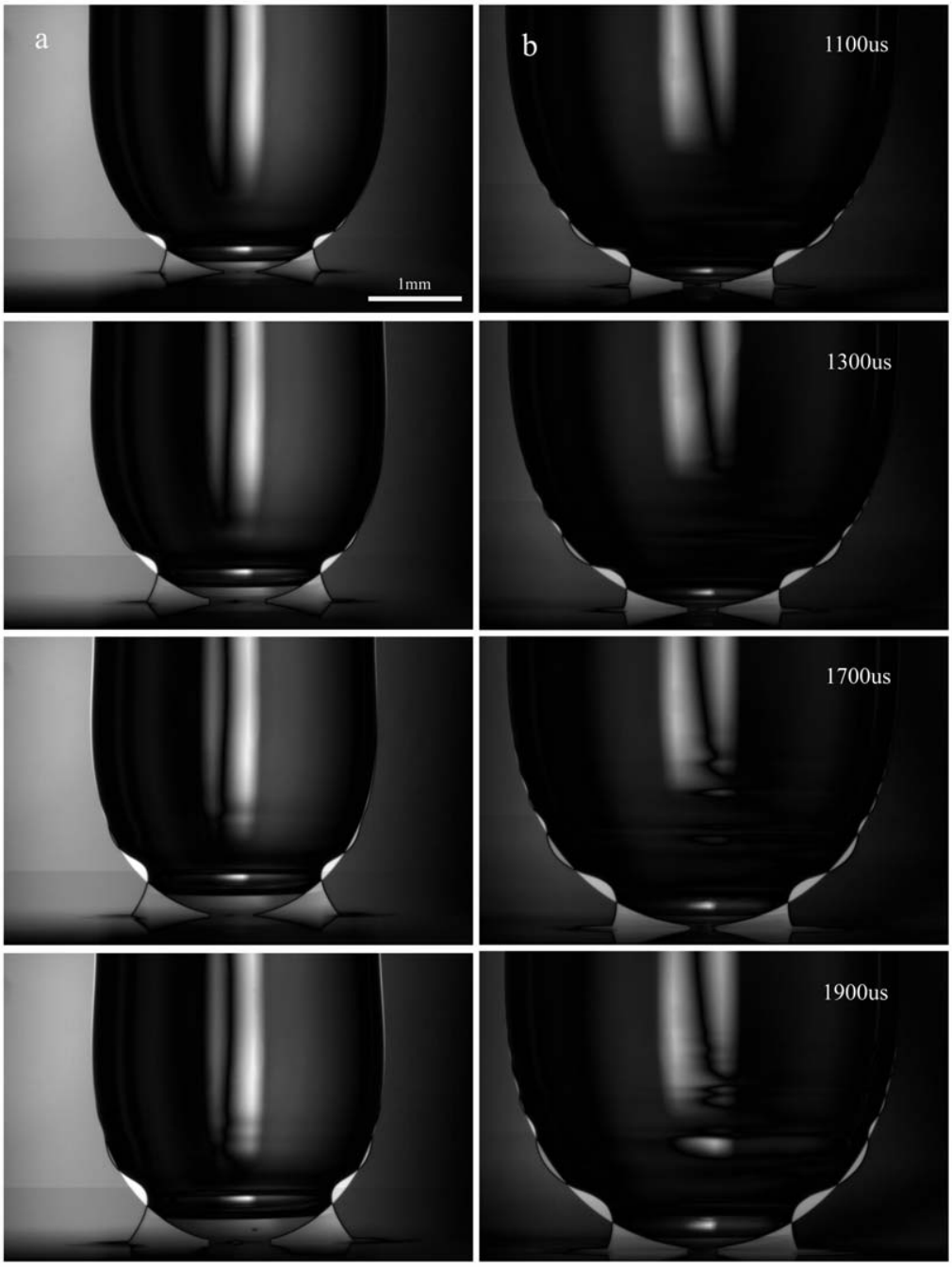

Figure 5-5: Comparison of coalescence evolution for (a) a drop of 94% ethanol/water mixture with the same mixture in the pool and (b) for a water drop onto ethanol/water solution pool.

This is due to the large difference in the value of the surface tension between water (73 dyn/cm) and ethanol (22 dyn/cm). The size of an alcohol drop is therefore much smaller than that of the water drop, under condition of the same top tube size and distance between the tube and bottom liquid surface. So it is not possible to compare

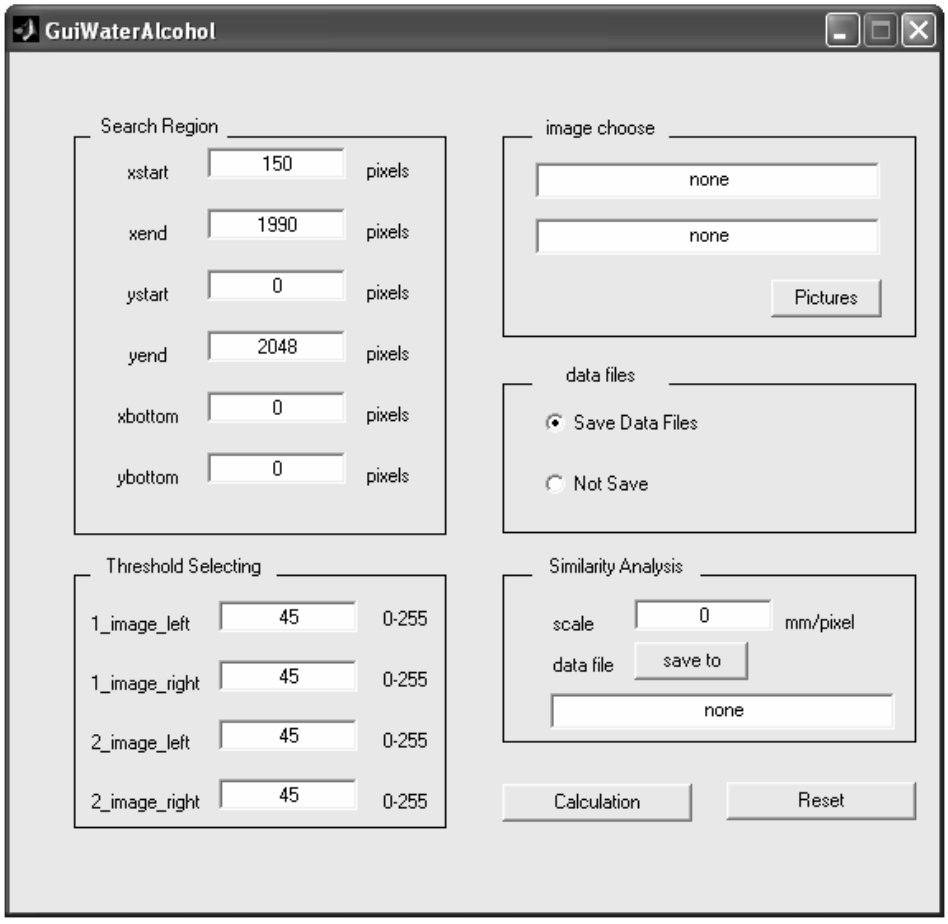

Figure 5-6: Input graphic interface built for the Matlab program that measures and draws the Marangoni wave shape.

directly the coalescence speeds between the cases of alcohol/alcohol and water/alcohol. Comparison of the coalescence shapes for water/water; water/alcohol and alcohol/alcohol indicate that the surface tension difference plays a major role in generating the surface waves. In other words Marangoni stresses are the main factor

in generating large surface waves. We can also conclude that the weaker surface tension determines the speed of coalescence.

The theoretical study of the coalescence of liquid wedges by Keller & Miksis (1983) showed that the wave shape traveling along the surface is self-similar. The configuration of that study is two-dimensional and furthermore it lacks an external

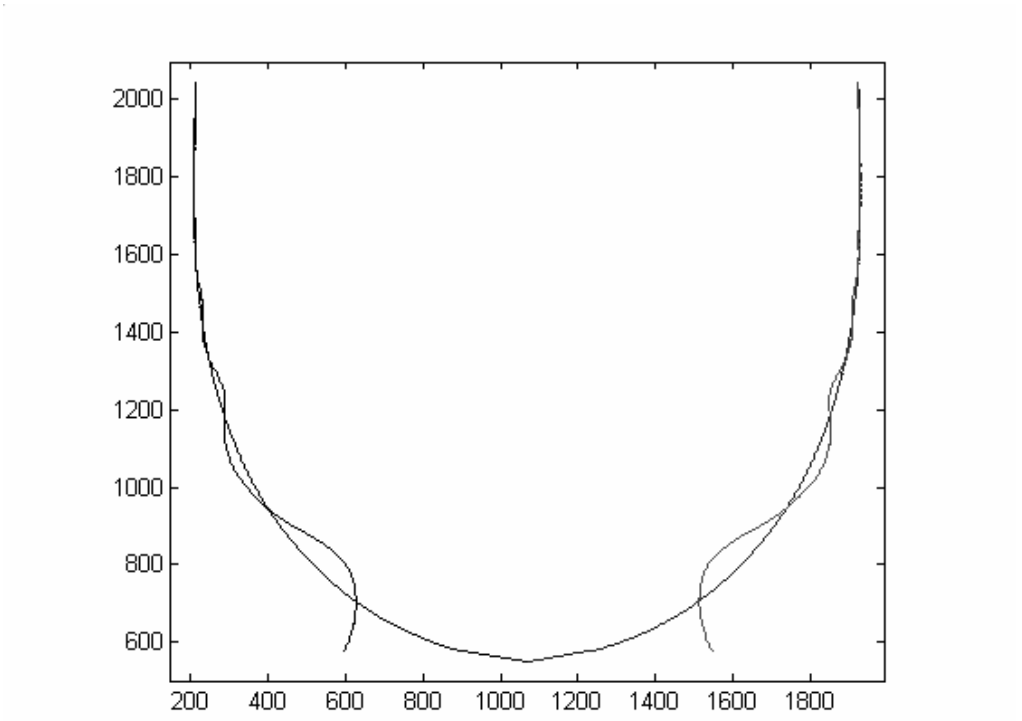

Figure 5-7: Drop shapes extracted from one set of dual images, the blue curve marks the edge of initial contacting drop and the red one shows the second drop shape after some given time of coalescence. The dimensions in the figure are in pixels.

length scale. Although both of these facts are not true of our experimental setup, i.e. a drop coalescing with a flat liquid surface, it still ignited our interests in looking for whether the self- similarity also exists for Marangoni waves generated from the large surface tension gradient, when water drop coalescing onto a alcohol liquid pool.

To study this we had to formulate the problem in terms of arklength s along the free surface. This required figuring out the drop shape from experimental images and

mapping the wave amplitude vs the arclength coordinate, where the amplitude is measured perpendicular to the original drop surface. To find the coalescence interface from the data images, many edge extraction techniques have been developed and realized in the matlab language written as internal Matlab functions. However, our images were sufficiently sharp and with good contrast, so it sufficed to simply selected a value of gray level as threshold to pick out the drop, instead of using those sophisticate edge detection techniques. One reason for this is that those conventional edge detection techniques required large computations and consume much computer resources, especially when large number of images need to be processed. Another

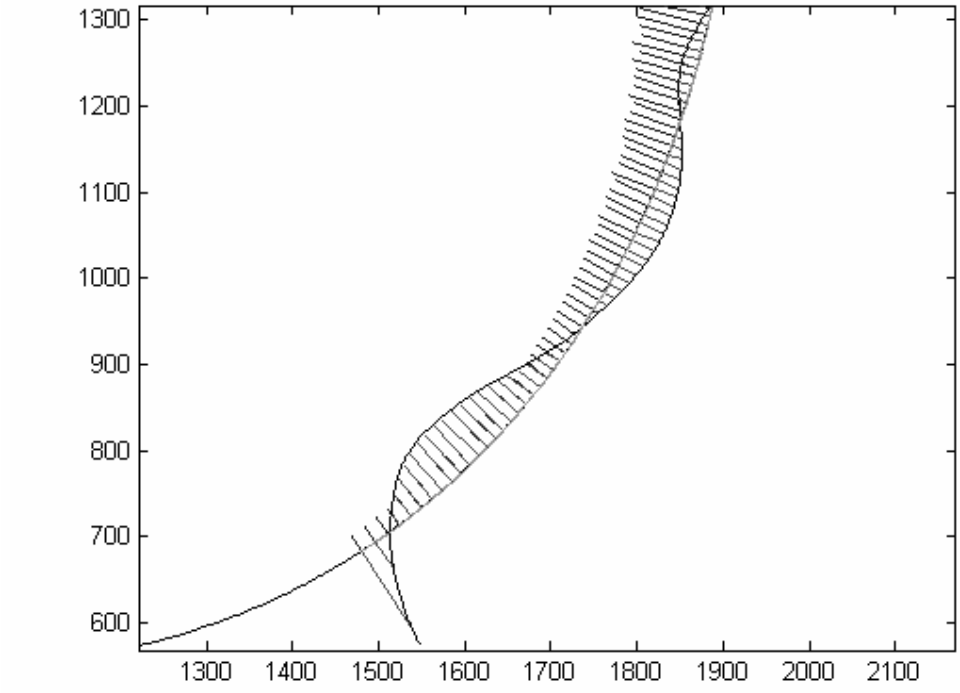

Figure 5-8: Sketch showing the search for a pair of corresponding points, whose connecting line is most normal to the tangential line through the investigated point on first curve, the green line denote the tangential line at each point and the blue line is the targeted line connecting the pair of corresponding points.

reason is that nearly identical results were obtained by the simple thresholding method as the other complicate edge detection methods mentioned above. The smoothness of the resulting drop surfaces are demonstrated in figure 5-7, where the wiggles are simply due to the pixel resolution of the CCD camera. To measure the amplitude of the wave in the second image, we employ the method illustrated in figure 5-8. We traverse along the original surface, point by point. At each of these points we find the tangent to the original drop surface. This was done by differentiating a polynomial curve fit, which is constructed over a set of points around the investigated point. Then we traverse along the second curve looking for the best point along the second curve, which is most perpendicular to the tangent at the investigated point on the first drop curve. This is simply done by drawing the vector from any particular point on the second curve and finding the dot-product with the tangent vector. The point which gives the scalar value closest to zero for this dot-product is the one closest to normal to the original surface. Traveling along this normal vector we can find the amplitude of the surface wave. Finally, some detection criteria were made to determine the signs of the wave amplitudes with respect to the first curve. To map the wave onto the curve of the original drop shape requirs calculating the arclength of all the points on the first curve. With 2 dimensional curve integration formula

$$\int_L f(x,y)ds = \int_{y_0}^{y} f[x,y(x)]\sqrt{1+y'^2(x)}dx$$

Here, $f(x,y)=1$ and $y'(x)$ is the slope of y with respect to x, which was obtained from differential of polynomial fitting function built with a set of data points around the calculated point. Because the curve is constructed of numerous discrete points, the integration was approximated by sum of all section lines at each point from the first

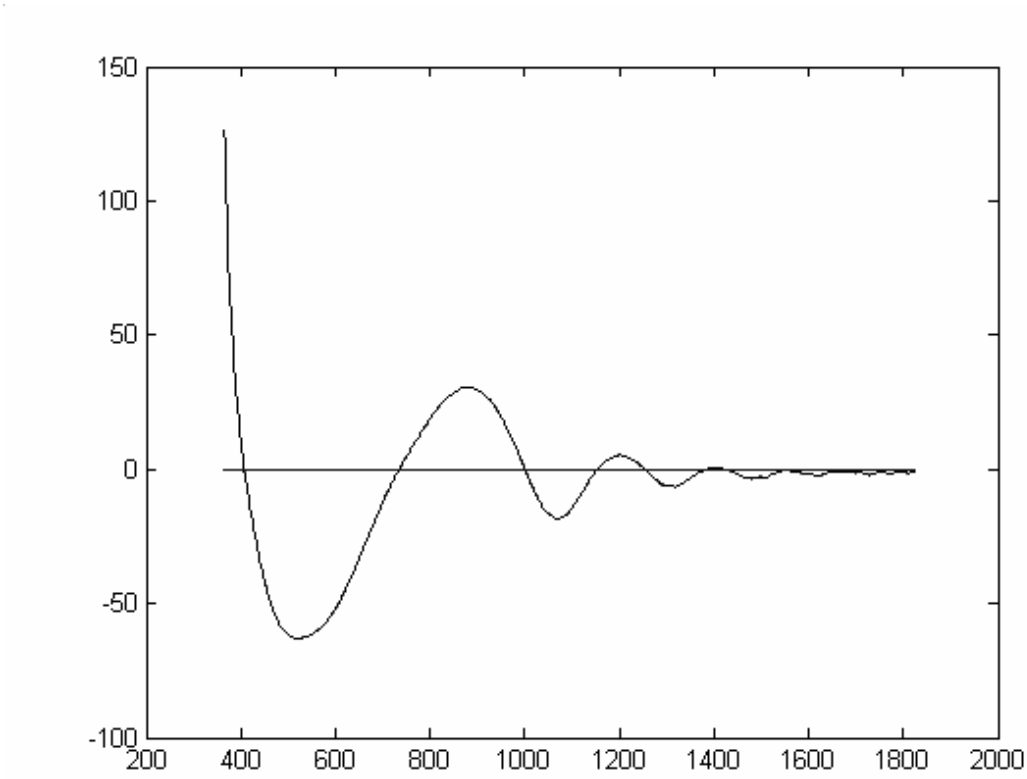

Figure 5-9: The profiles of the Marangoni wave along the drop surface in dimension of pixels for both coordinates.

contact point to the calculated point. Figure 5-9 shows a typical result for a Marangoni wave measured along the arclength of the original drop shape from one pair of experimental images. The *x*-coordinate denotes the curve's arclength from the first drop shape with the zero point fixed at the first contact point at the axis of symmetry. The y-coordinate indicates the wave amplitude of the drop surface in the second image. The measurements and calculations performed by this computer program follow the algorithm sketched in the box-diagram in figure 5-10.

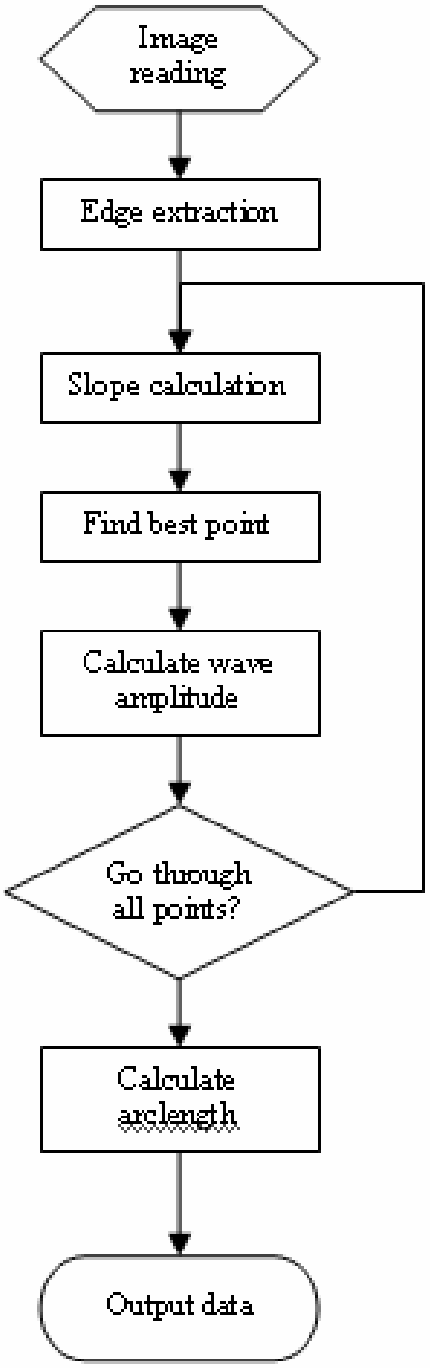

Figure 5-10: The programming algorithm used to extract the Marangoni wave from the images.

Figure 5-11 shows the time evolution of the Marangoni wave observed during the coalescence of a water drop with a pool of 94% ethanol. These wave-shapes were calculated from images similar to those presented previously in figure 5-2. The wave

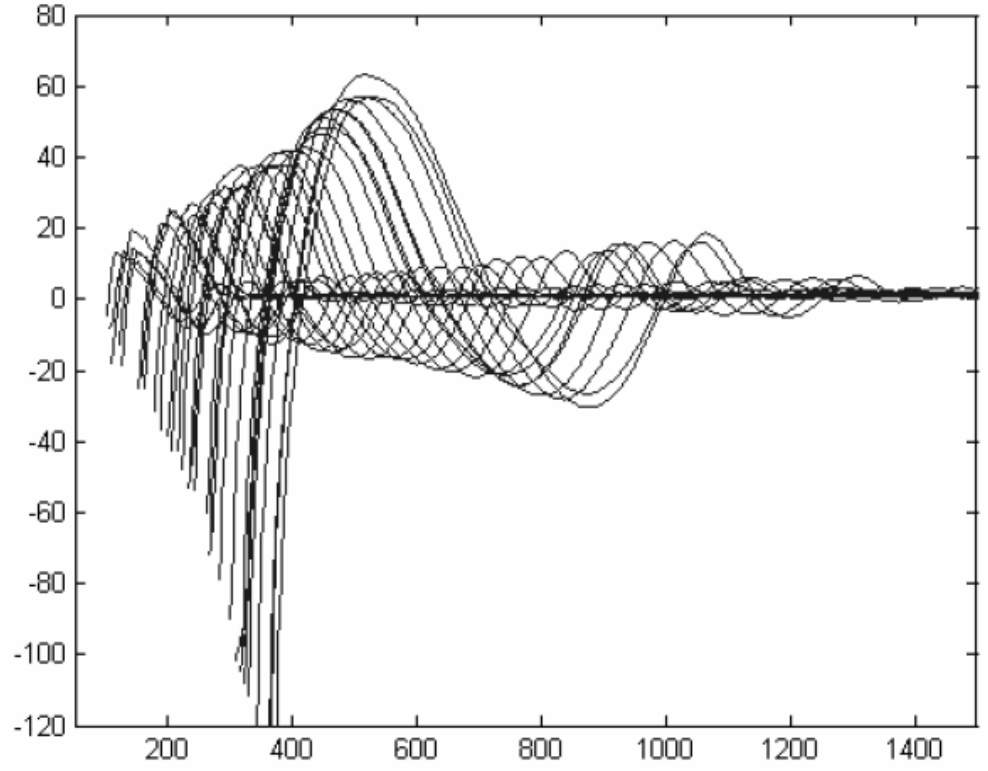

Figure 5-11: The amplitude of the Marangoni wave normal to the static drop surface, vs arclength, as it travels up the water drop. The wave-shape is shown at different times after initial contact. The axes are in units of pixels.

amplitude and wavelength increases with time measured from the beginning of the coalescence. The envelope of the Marangoni wave appears to follow approximately a straight line, i.e. the amplitude grows linearly as a function of arclenght. In comparison, the coalescence of a water drop with a pool of water (see photographs in figure 5-12) shows a slightly curved line where the amplitude grows slightly faster than linearly. This comparison also shows that the amplitude for water/alcohol wave is larger than for the water/water case. This is clearly seen by comparing the amplitude vs. arclength in figure 5-11 and 5-12. In figure 5-11 the maximum

amplitude is 60 pixels when the wave-crest has reached arclength *s*=550 pixels, whereas in figure 5-12, the amplitude is only about 30 pixels at this arclength. This is especially true for the amplitudes of the second and third waves. It indicates that the Marangoni forces must be increasing the amplitude of the waves in the former case, whereas for water/water the Marangoni stresses are absent and the amplitude of the capillary waves grow very slowly.

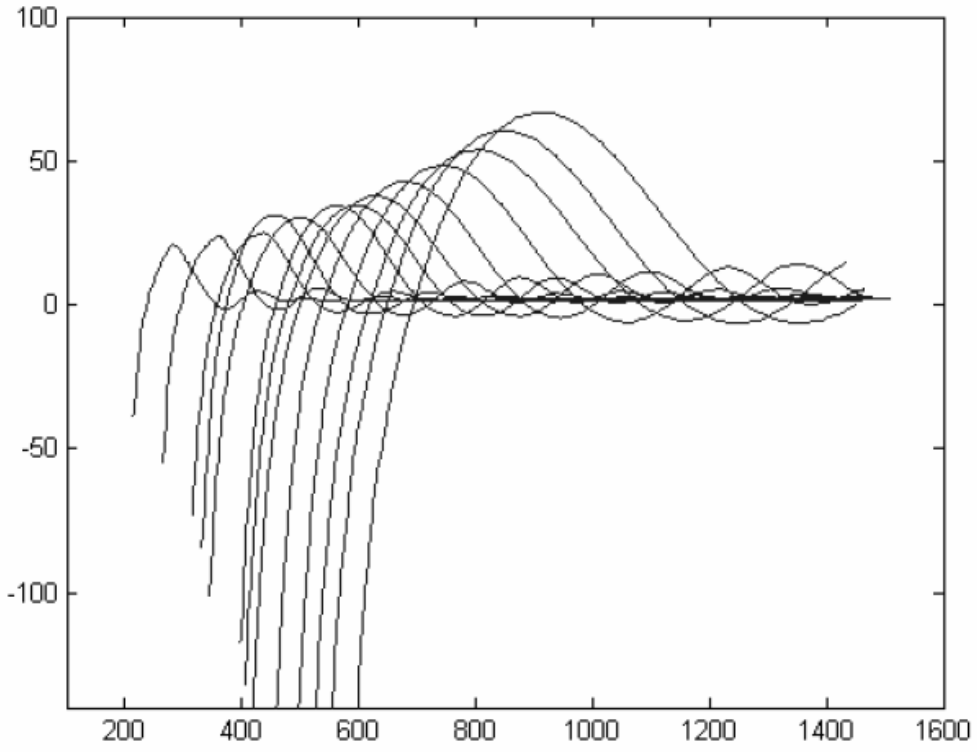

Figure 5-12: The shape of the capillary wave measured from the coalescence of a water drop with a water pool, as shown in left column of figure 5-4.

5.1.1 Effect of drop size on the coalescence

The size of the water drop, changes the internal pressure inside the drop and total curvature of the surface along which the waves will travel. To investigate whether this changes the speed of the Marangoni waves we have performed the same experiment for four different needles, i.e. four different drop sizes. Besides a tube of

an outer diameter of 4.75 mm, we also employed three other tube sizes, 2.95, 1.85 and 0.88 mm in diameter. The observed coalescence evolutions for the different sized drops are presented in figures 5-13, 5-14 and 5-15. The figures show an unavoidable change in the pendent drop shapes, due to the different distortion due to the gravity, which depends on the size of the drop relative to the capillary length. The smaller the drop, the more spherical it becomes. Due to the variation in the drop size, the time it takes the wave to travel from the bottom tip of the drop up to the tube becomes shorter when the drop diameter is decreased. This time duration for the coalescence of water/alcohol with 0.88 mm tube reduced to 1 ms from 2 ms for the 1.85 mm tube. This indicates that the wave traveling speeds are similar independent of drop size, thus only depending weakly on the internal pressure inside the drop.

We also measured the shape of the Marangoni waves for these coalescence experiments using the different size tubes. These results show similar linear growth in amplitude vs. arclength. This will be discussed in reference to self-similarity in the Discussion section.

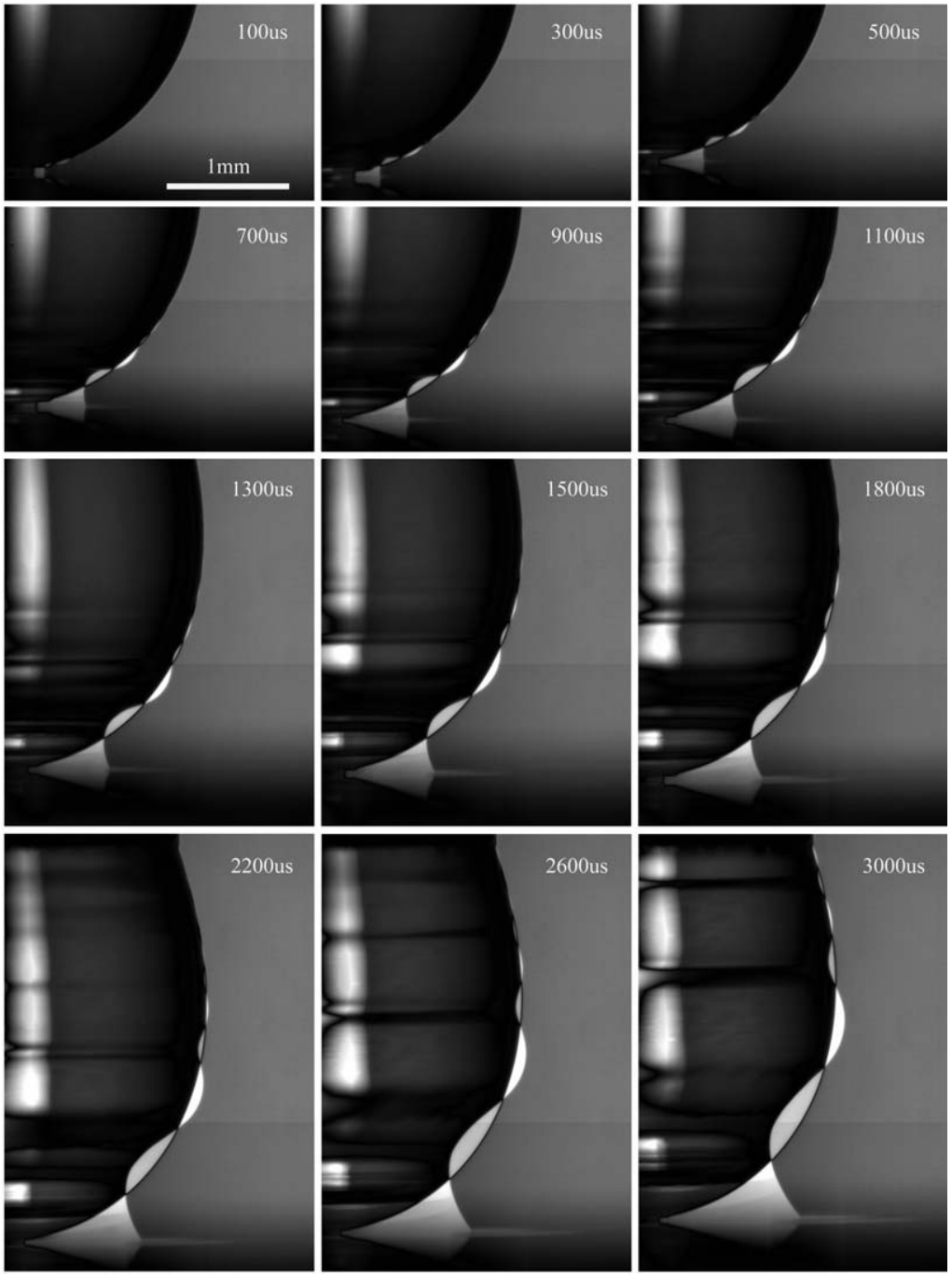

Figure 5-13: Coalescence of a water drop onto ethanol/water mixture pool, the needle used to produce the pendent drops had a outside diameter of D=2.95 mm.

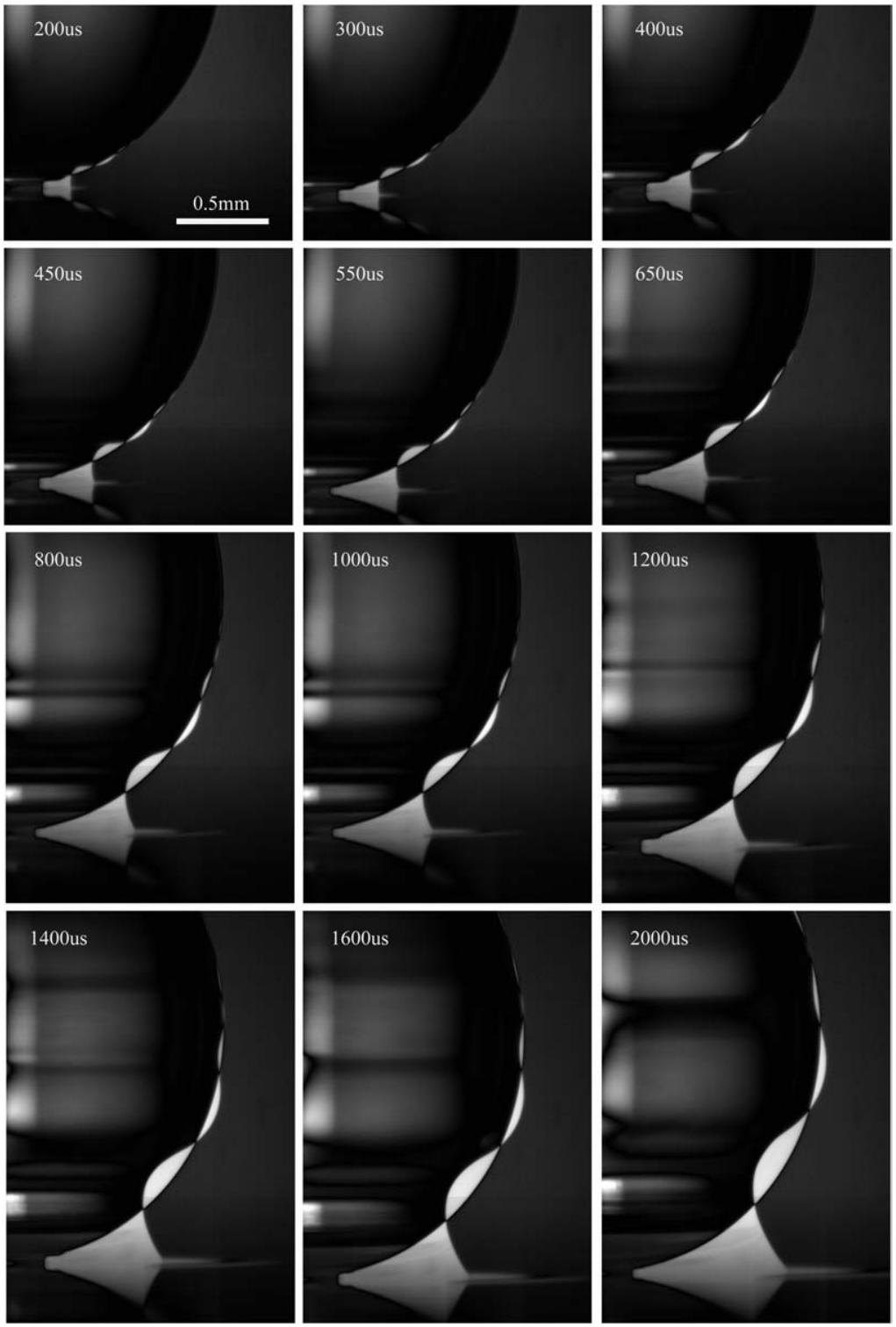

Figure 5-14: Coalescence of a water drop onto ethanol/water mixture pool, the needle used to produce the pendent drops had a outside diameter of D=1.85 mm.

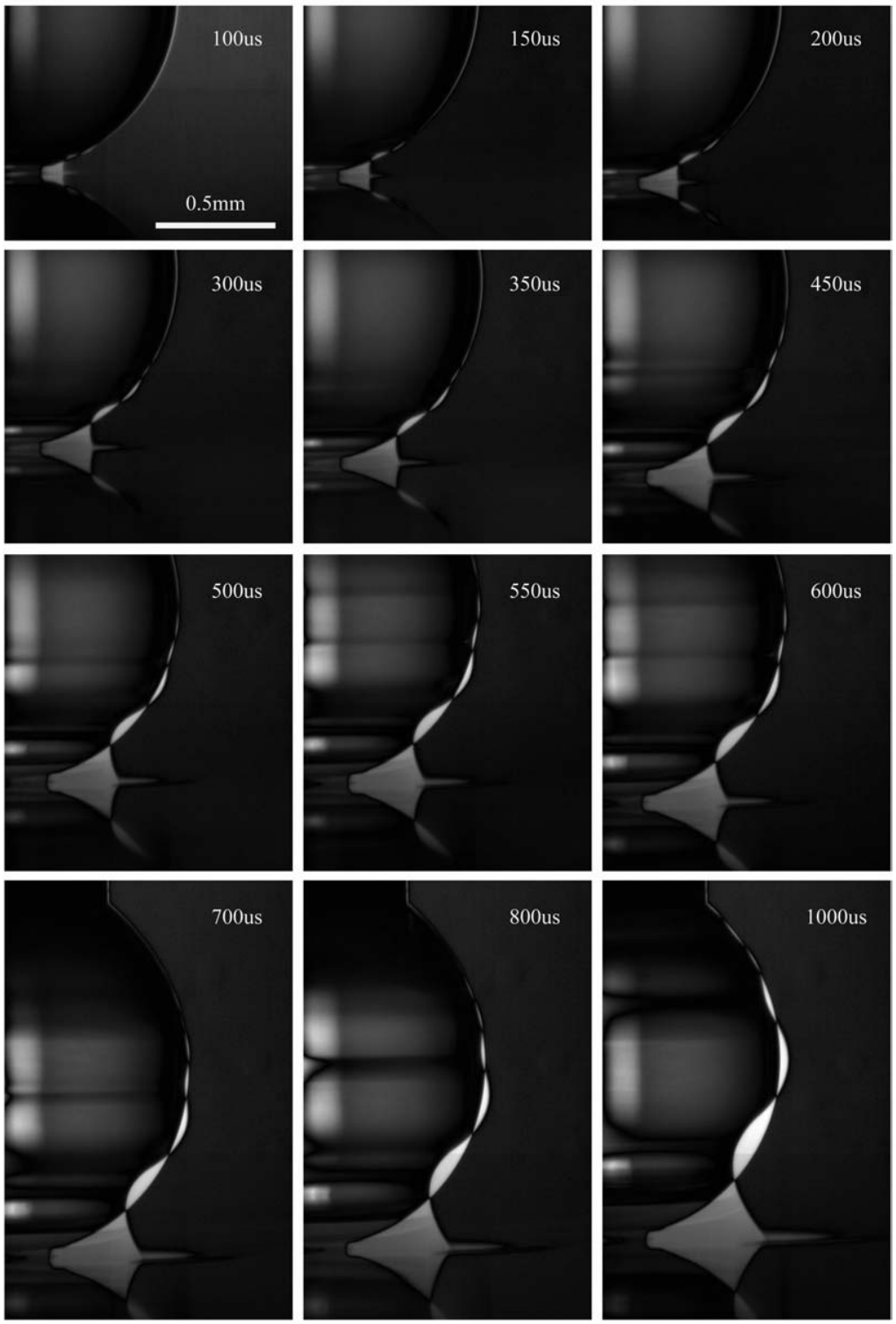

Figure 5-15: Coalescence of a water drop onto ethanol/water mixture pool, the needle used to produce the pendent drops had a outside diameter of D=0.88 mm. Note that the horizontal extent of each image panel is only about 1.2 mm.

5.1.2 Large water drop coalescing with small alcohol drop

To assess the effect of the contact size on the Marangoni waves, we used a small ethanol drop instead of the pool of ethanol used in all the previous figures. This setup is shown in figure5-16. If the surface concentration of the ethanol affects the Marangoni wave-shape, one would expect this configuration to give different results than the coalescence with a flat pool, as there is more area to drag ethanol from for the drop pool case. In other words, the circumference of the pure ethanol is much larger in the pool case than for the small drop case.

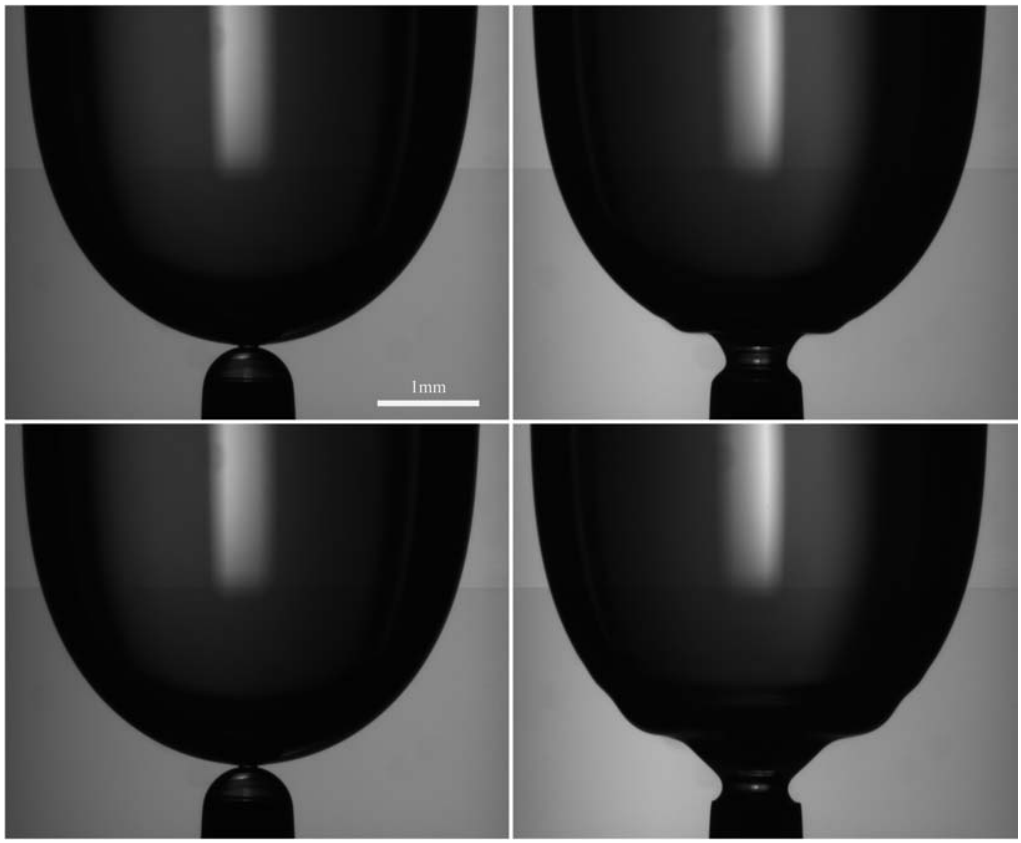

Figure 5-16: Coalescence of large water drop (top) with small ethanol/water drop (bottom), the needle size for producing the water drop is 4.75 mm and the one for ethanol is 0.88 mm, the times shown in the right panels are 550 μs (top) and 1300 μs (bottom) after the first contact.

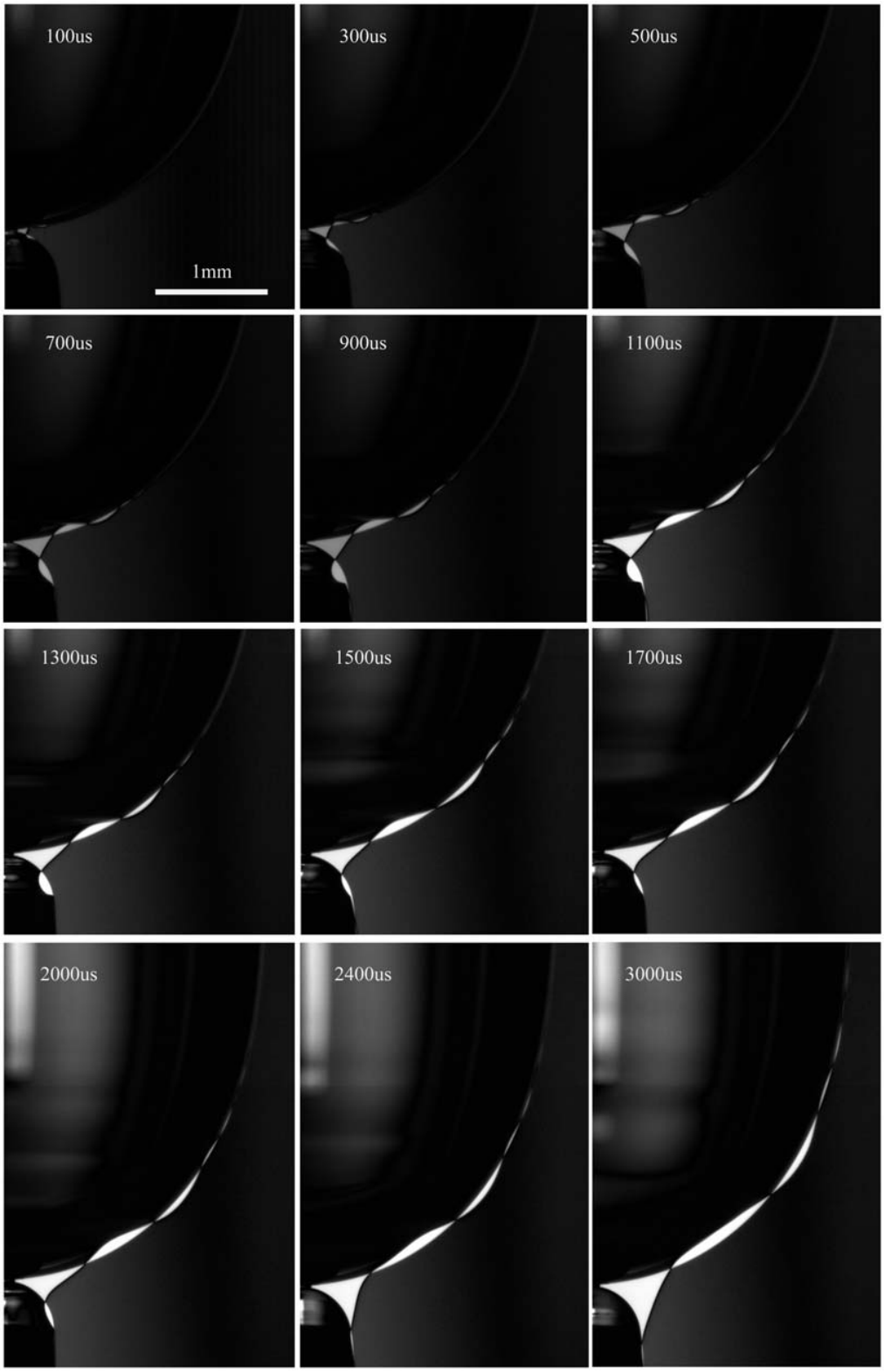

Figure 5-17: Evolution of coalescence of widely different size drops, the top drop is water drop generated with tube D=4.75 mm and the bottom ethanol/water drop produced with needle D=0.88 mm.

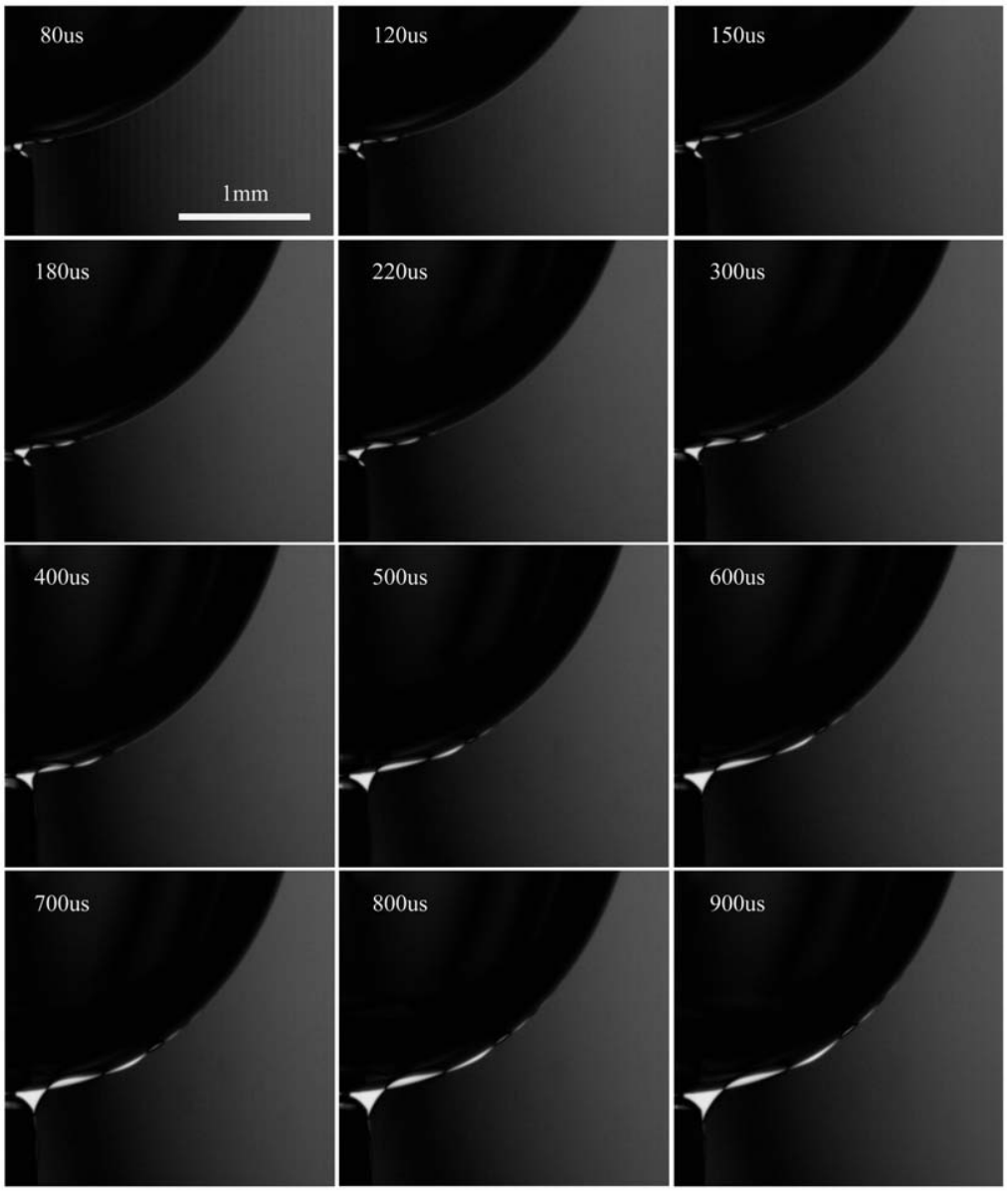

Figure 5-18: Evolution of coalescence of widely different size drops, the top drop is water drop generated with tube D=4.75 mm and the bottom ethanol/water drop produced with needle D=0.40 mm.

Figures 5-17 and 5-18 shows the surface shapes during this type of coalescence. Two different sizes needles, 0.88 and 0.4 mm in diameter, were used to generate the bottom drop. Due to the low surface tension of ethanol and the fact that the ethanol wets the steel tubes, the ethanol drop at the bottom needle had to be kept

small, only forming a hemisphere. If it was grown any larger it would travel down the outside of the bottom tube.

The results are clearly different for this configuration with the small drop, compared to the coalescence with a flat surface. This is especially true for the smaller bottom drop, generated on the 0.4 mm tube, in figure 5-18, where the amplitude of the waves does not grow much after the initial stage. When neck region touched the edge of the bottom needle, the wave stretches without obvious increase in wave amplitude. This observation was clearly seen in the wave measurement shown in figure 5-19. The wave origin is now fixed at the bottom needle, but as the wavelength increases the wave amplitude stays almost the same, or even reduces slightly.

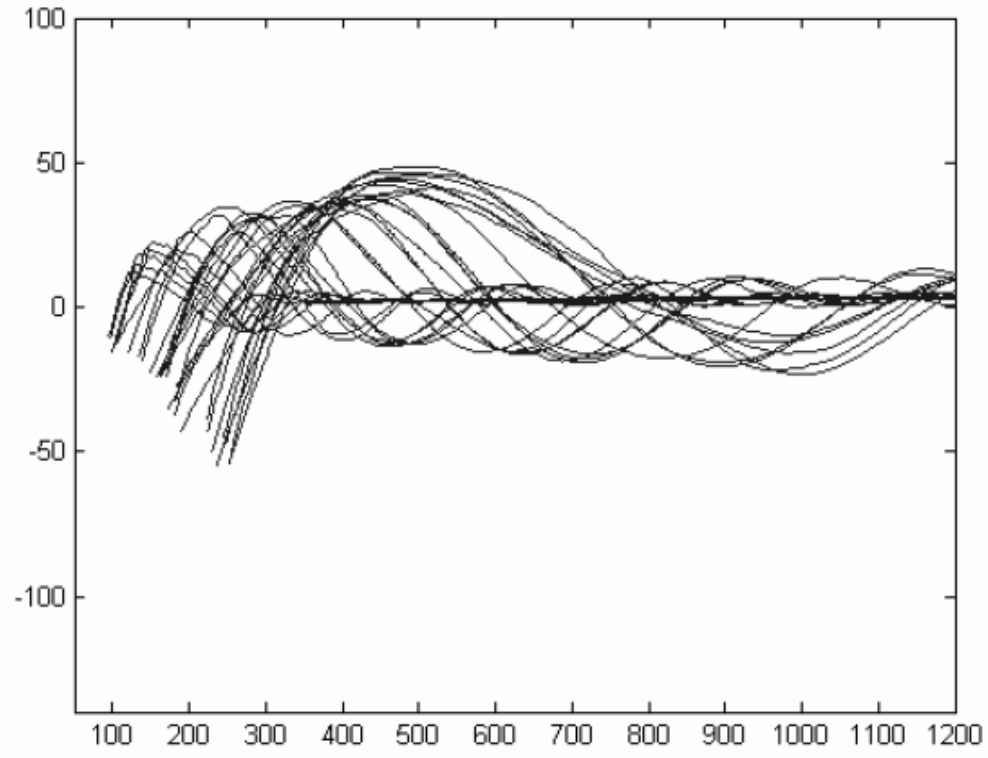

Figure 5-19: Marangoni wave measured from coalescence of water drop with a much smaller ethanol drop generated with 0.88 mm tube.

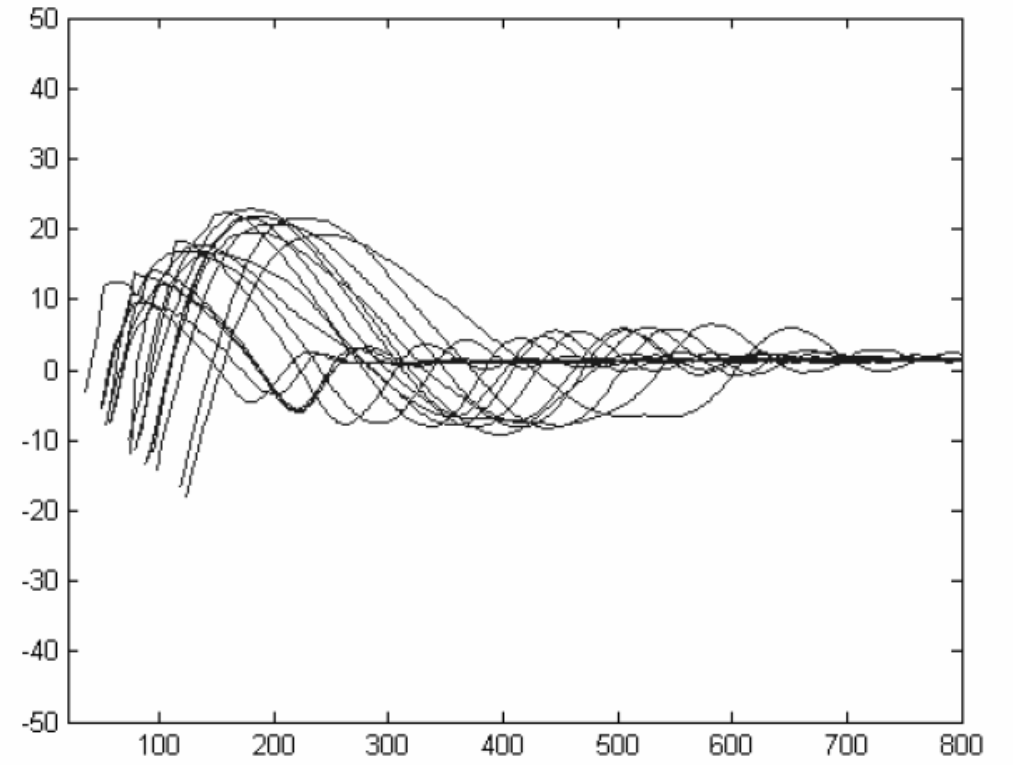

Figure 5-20: Marangoni wave measured from coalescence of water drop with a much smaller ethanol drop generated with 0.4 mm tube.

From comparison of figures 5-19 and 5-20, the maximum wave amplitude observed in both of the experiments with the 0.88 mm and the 0.4 mm needle, is about the same in relative terms, i.e. taking into account the magnification. The maximum amplitude are about 50 at s=500 and 20 at s=200.

5.2 Glycerin drop coalescing with water

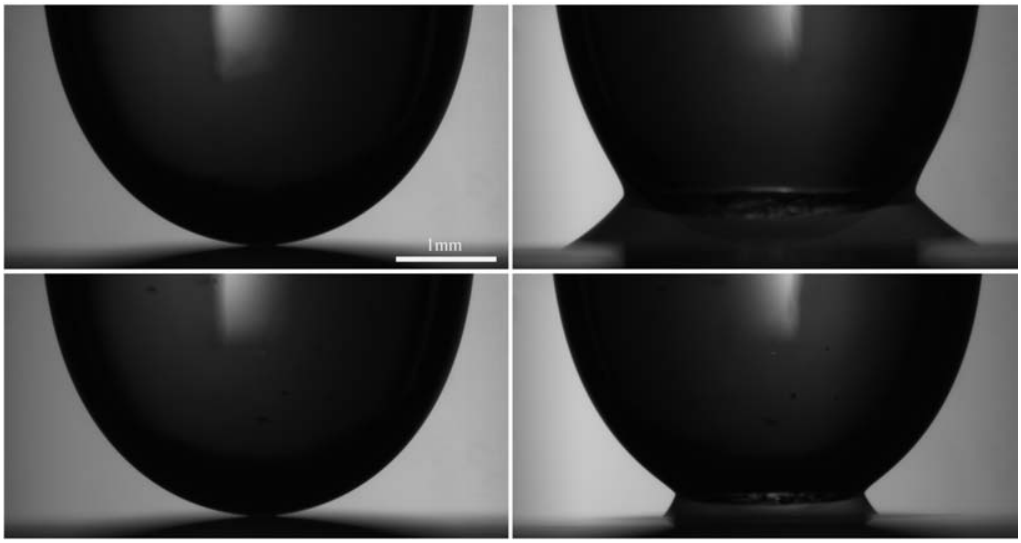

Figure 5-21: Coalescence of 98% glycerin/water drop onto flat water surface, the left panels showed the first contact and the right ones present the coalescing shapes with times 1600 μs (bottom) and 5000 μs after first contact.

To investigate the effects of a viscosity difference on the drop coalescence, we perform experiments on a configuration of a highly viscous glycerin drop coalescing with a water pool, as shown in figures 5-21. It is easily seen that with drops of high viscosity, the capillary wave shown in figure 5-22, which appears on the water drop surface during the coalescence of water/water, disappear and only one main 'wave' is observed, as a sharp corner where the coalescing neck meets the drop surface. The curvature in this neck region can be quite sharp and determining this curvature was one of the primary aims of this part of this coalescence study.

Due to the large difference in viscosity between the glycerin drop and water pool, this setup is reminiscent of drop spreading along a solid surface. However, there is a basic different between those two configurations, as our setup has no contact-line, where the liquid, the solid and the air meet. Here we are dealing with two miscible liquids, which will not have a sharp contact line. The advancing front of the water layer is assumed to be at the sharp corner in the neck region. To verify

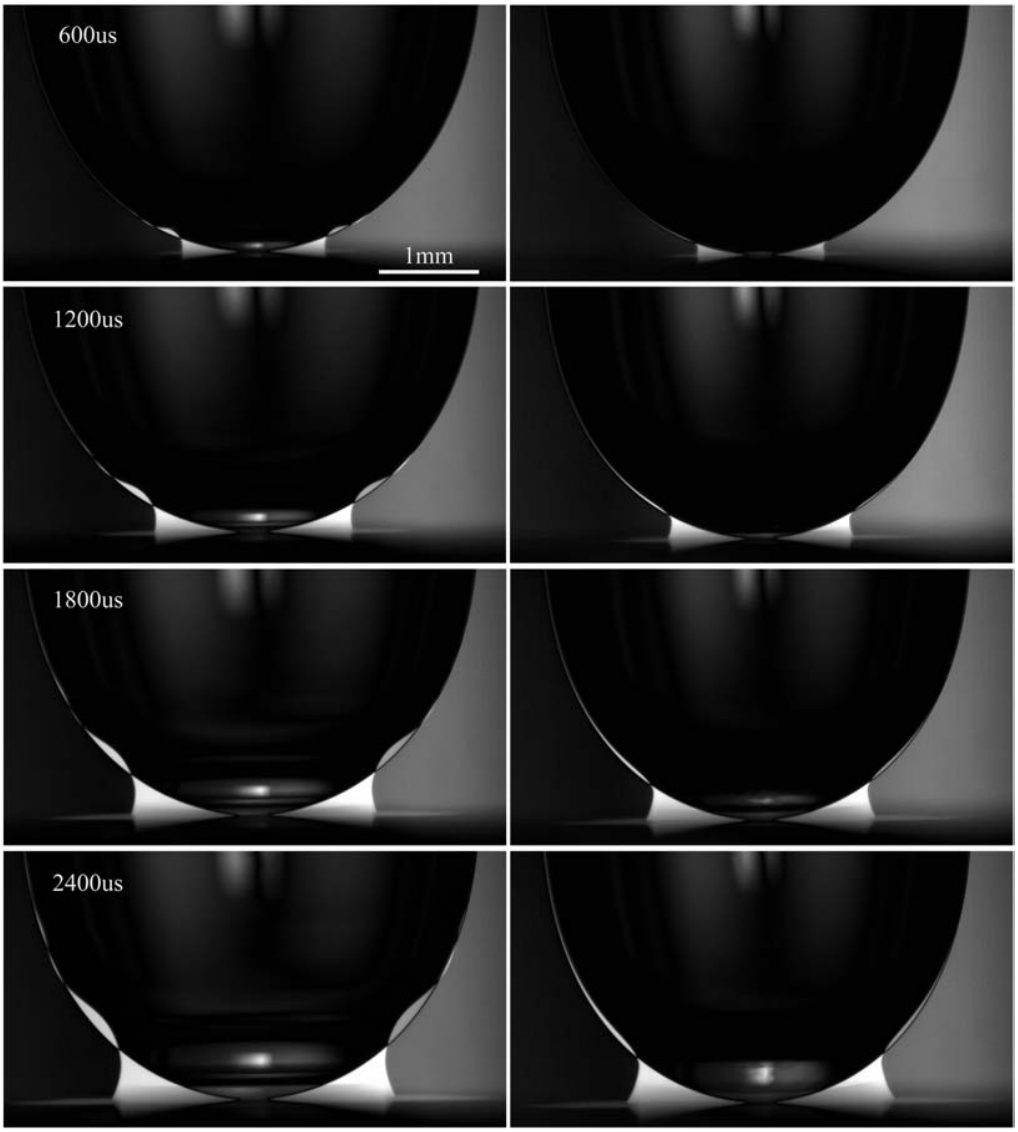

Figure 5-22: Comparison of drop coalescence between water_water and glycerin_water, the left column pictures show the coalescence shape of water_water and the right panels present the coalescence of 85% glycerin to water.

the location of interface between the two coalescing liquids, we added a trace of Fluorescence molecules into the bottom liquid pool and illuminated the vertical plane of coalescence with a laser light sheet. In figure 5-23, the horizontal white region marks the advancing interface of the bottom liquid. The drop surface is marked by a weak laser-light reflection, which we attempted to dampen out by using a band-pass

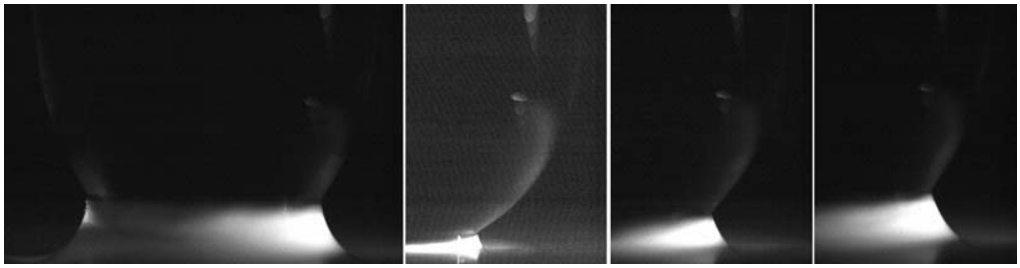

Figure 5-23: Interface imaging of glycerin/water mixture drop coalescing with flat water surface, the bottom liquid in addition of fluorescent was distinguished from the top drop by adjusting the gray level, the times shown in the image from left to right are 5000, 1000, 2500 and 4000 μs.

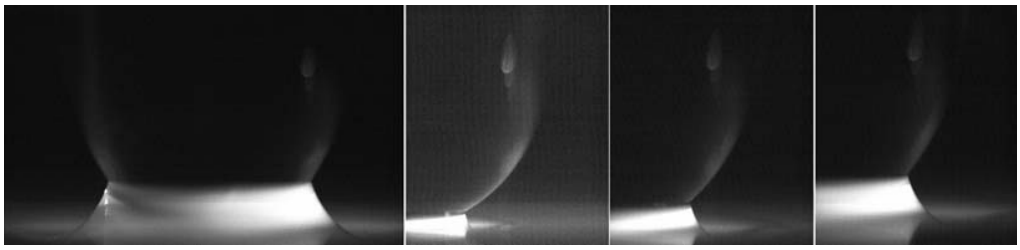

Figure 5-24: Interface imaging of glycerin/water mixture drop coalescing with flat 94% ethanol/water mixture surface, the times shown in the image from left to right are 5000, 1000, 2500 and 4000 μs.

filter at 510 nm. This is slightly lower than the wavelength of the Yag-laser, which is 532 nm. Due to the difference of light intensity between the bottom liquid and the drop, it is easy to identify the interface from these images. Figure 5-23 and 5-24 shows that as we expected the interface is always located in the neck region, where the curvature is largest. Table 5-1 shows the viscosity and surface tension for the glycerin mixtures used.

Glycerin % by volume	Density ρ kg/m^3	Viscosity μ $kg/(m \cdot s)$	Surface Tension σ N/m
0	1000	1.0×10^{-3}	0.072
70	1175	28.9×10^{-3}	0.065
80	1200	73.3×10^{-3}	0.065
85	1212	128×10^{-3}	0.065
90	1225	238×10^{-3}	0.065
95	1238	486×10^{-3}	0.065
98	1245	781×10^{-3}	0.065

Table 5-1: List liquid properties for glycerin/water mixtures at temperature of 22^o C

To study how the curvature at the neck region changes during the coalescence, a Matlab program was written, by the candidate, to measure this curvature directly from the images. This curvature will then be investigated as the radius of the neck grows in size during the coalescence.

For a two dimensional plane curve which is given by Cartesian parametric equations $x = x(t)$ and $y = y(t)$, where t here is not the time, but rather a parameter identifying the location along the curve, we have the formula defining the curvature,

$$\begin{aligned}\kappa &\equiv \frac{d\phi}{ds} \\ &= \frac{\frac{d\phi}{dt}}{\frac{ds}{dt}} \\ &= \frac{\frac{d\phi}{dt}}{\sqrt{\left(\frac{dx}{dt}\right)^2 + \left(\frac{dy}{dt}\right)^2}} \\ &= \frac{\frac{d\phi}{dt}}{\sqrt{x'^2 + y'^2}}\end{aligned}$$

where ϕ is the tangential angle and s is the arc length. As can readily be seen from the definition, curvature therefore has units of inverse distance, i.e. one over the radius of curvature. The $d\phi/dt$ derivative in the above equation can be found using the identity

$$\tan\phi = \frac{dy}{dx} = \frac{dy/dt}{dx/dt} = \frac{y'}{x'}$$

So

$$\frac{d}{dt}(\tan\phi) = \sec^2\phi\frac{d\phi}{dt} = \frac{x'y'' - y'x''}{x'^2}$$

And

$$\frac{d\phi}{dt} = \frac{1}{\sec^2\phi}\frac{d}{dt}(\tan\phi)$$
$$= \frac{1}{1+\tan^2\phi}\frac{x'y'' - y'x''}{x'^2}$$
$$= \frac{1}{1+\frac{y'^2}{x'^2}}\frac{x'y'' - y'x''}{x'^2} = \frac{x'y'' -' y'x''}{x'^2 + y'^2}$$

Combining above equations then gives

$$\kappa = \frac{x'y'' - y'x''}{\left(x'^2 + y'^2\right)^{3/2}}$$

For a two-dimensional curve written in the form $y = f(x)$, the equation of curvature becomes

$$\kappa = \frac{\frac{d^2y}{d^2x}}{\left[1+\left(\frac{dy}{dx}\right)^2\right]^{3/2}}$$

Here we look for a polynomial function to approximate the drop shape, which has been extracted from the experimental images, using thresholding techniques described in previous sections. Then the derivative $\frac{dy}{dx}$ is calculated by differentiating the polynomial function and then the curvature is obtained. To find the best curve-fitting function, the set of data points was selected carefully to reduce the residues around

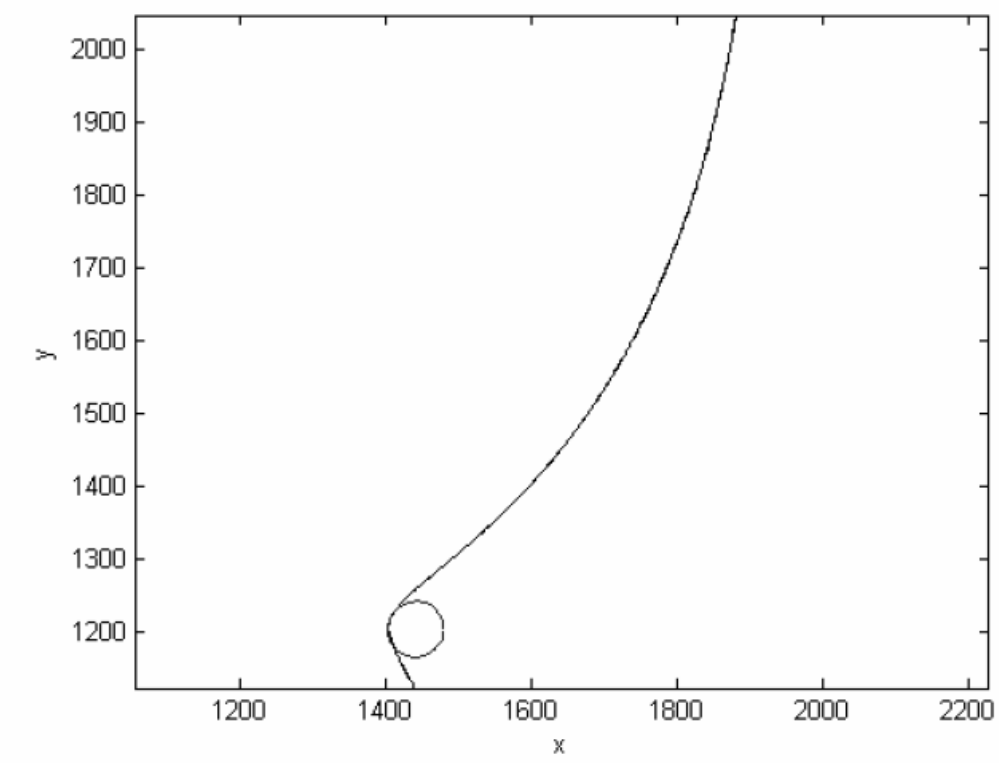

Figure 5-25: Inscribed circle at the corner of the contact neck region between the two liquids, The curve shows the instantaneous drop shape during coalescence.

the curve-fitting function. This required reducing the number of data point in the region of the largest curvature, which is realized within a loop in the program, which guarantees that the residues are below a certain level. One example of the inscribed circle found using this program is shown in figure 5-25.

5.2.1 Effect of viscosity on the coalescence

To study how the strength of the difference in liquid viscosity affects the drop coalescence shape and neck curvature, we performed the same experiment with drops of glycerin/water mixtures over a range of viscosities, for concentrations from 80% to 98% by volume. The resulting images were shown in figures 5-26, 5-27, 5-28, 5-29, and 5-30. The images are again contrasted with the static drop shapes and the white

region marks the shape difference. It is seen that for the highest drop viscosity the glycerin drop keeps its shape and the curvature in the corner of the neck region does not change much. As the viscosity is lowered, the drop shape changes as is clear in the difference images. The neck shapes become much smoother and the curvature is reduced.

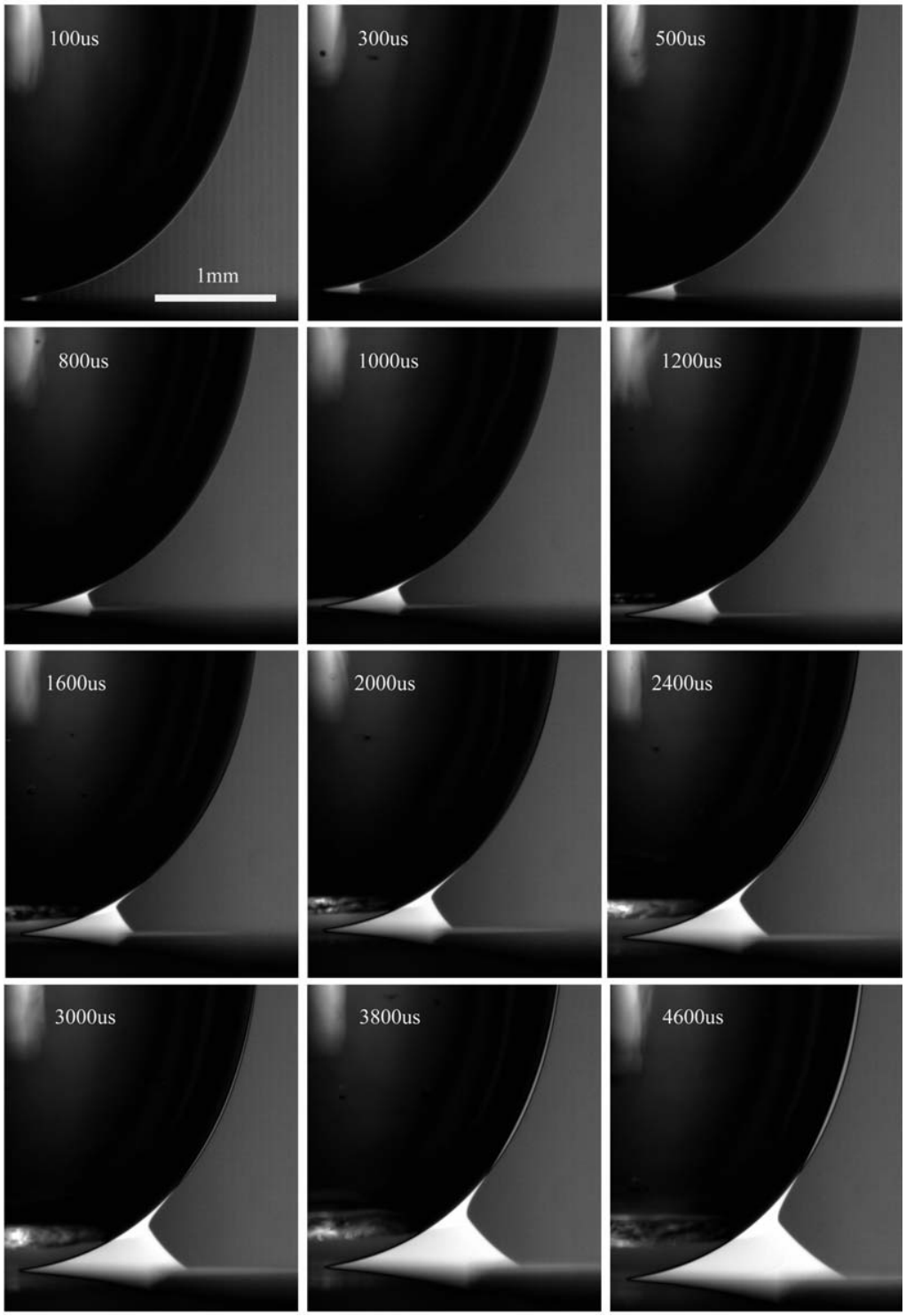

Figure 5-26: Coalescence of 98% glycerin/water mixture drop onto water pool, the needle used to produce the drop had outside diameter D=4.75 mm.

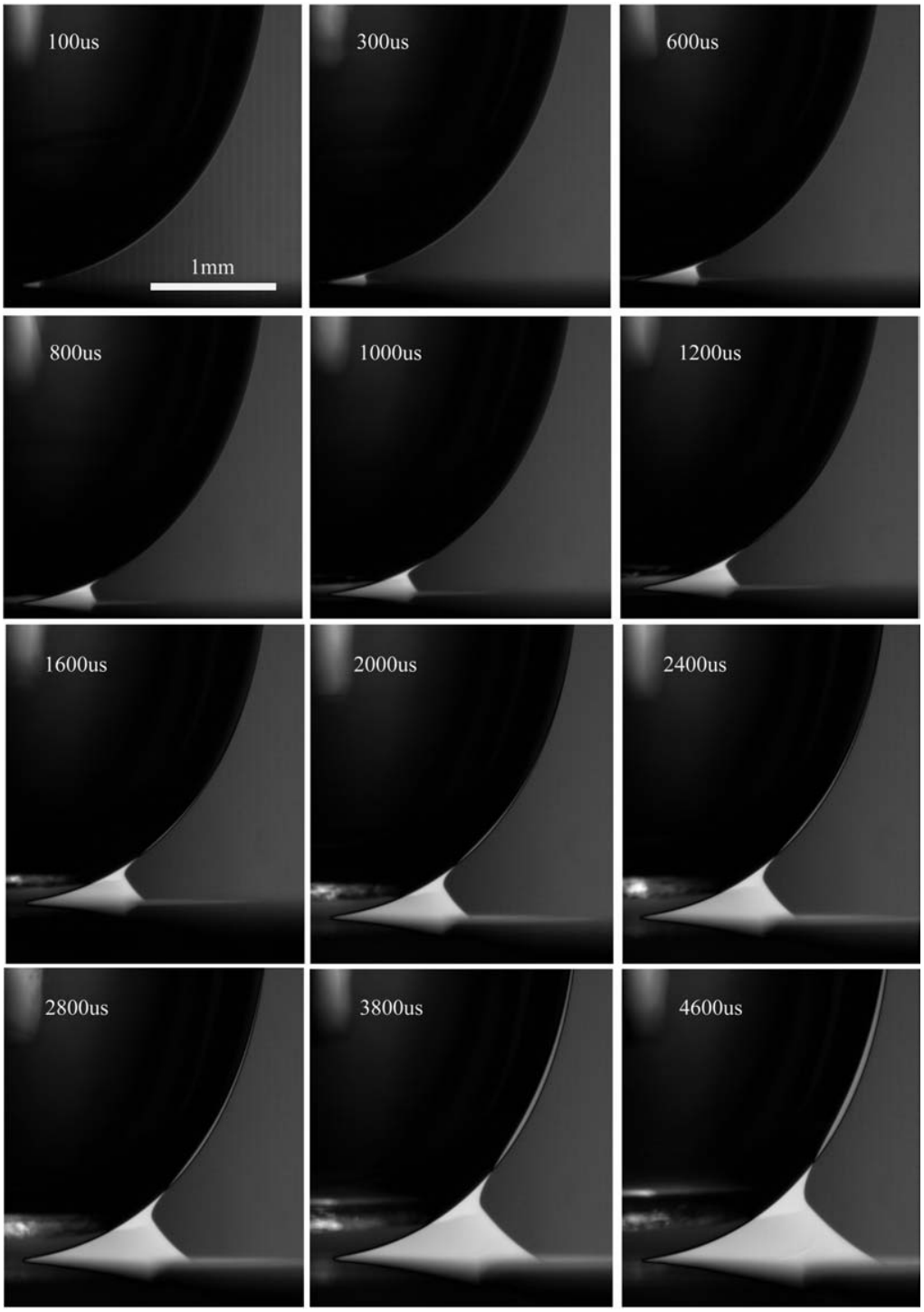

Figure 5-27: Coalescence of 95% glycerin/water mixture drop onto water pool, the needle used to produce the drop had outside diameter D=4.75 mm.

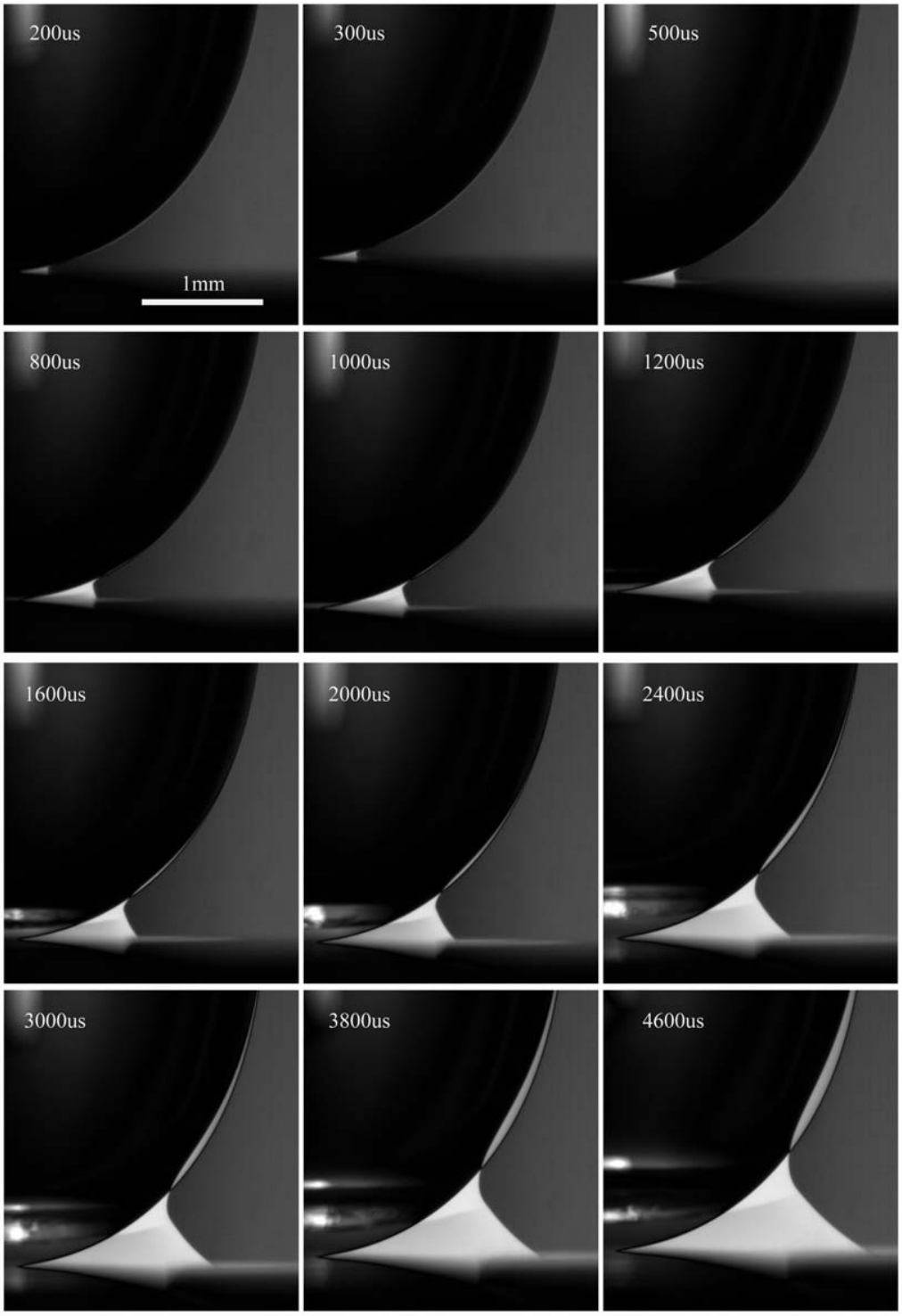

Figure 5-28: Coalescence of 90% glycerin/water mixture drop onto water pool, the needle used to produce the drop had outside diameter D=4.75 mm.

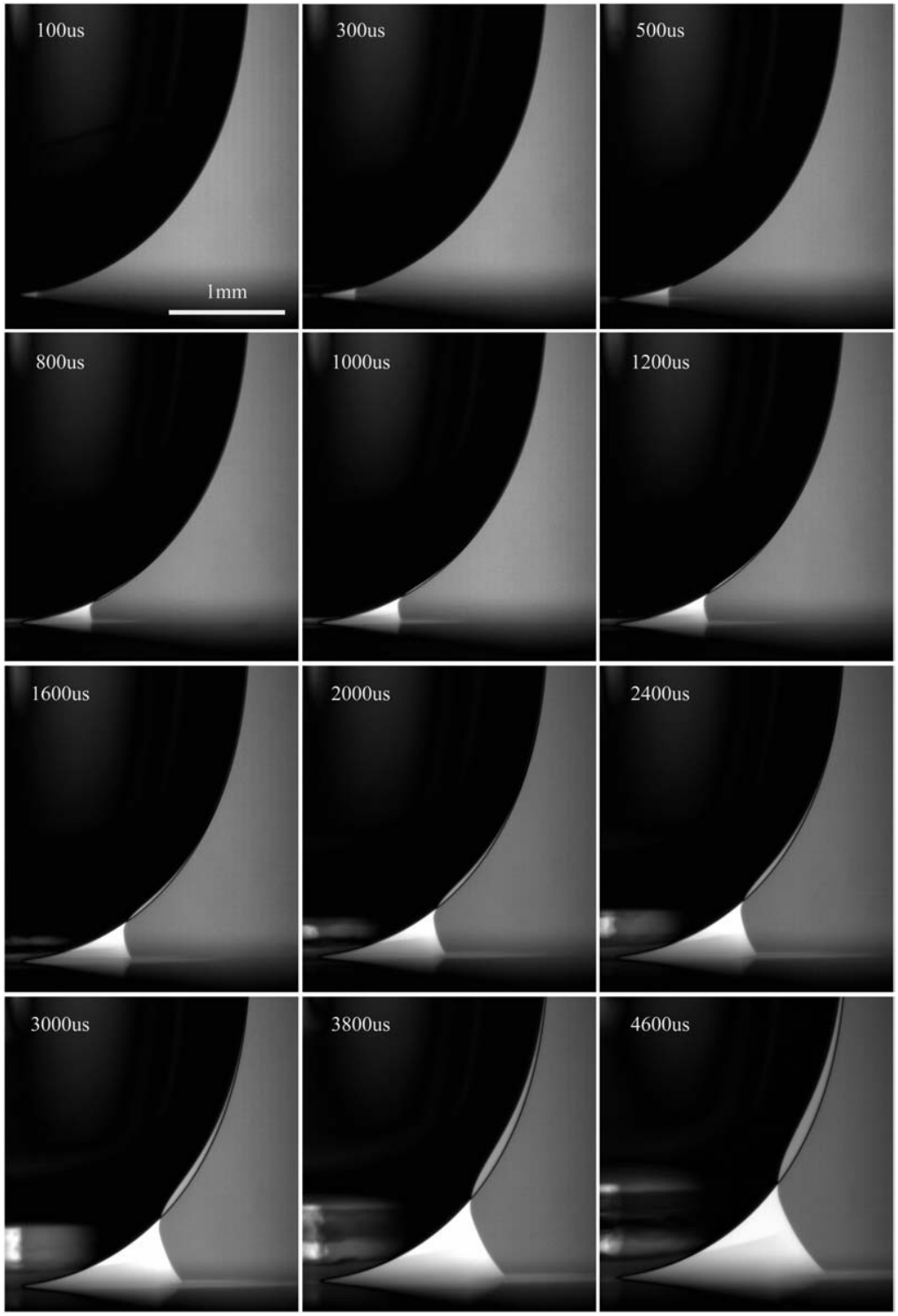

Figure 5-29: Coalescence of 85% glycerin onto water pool.

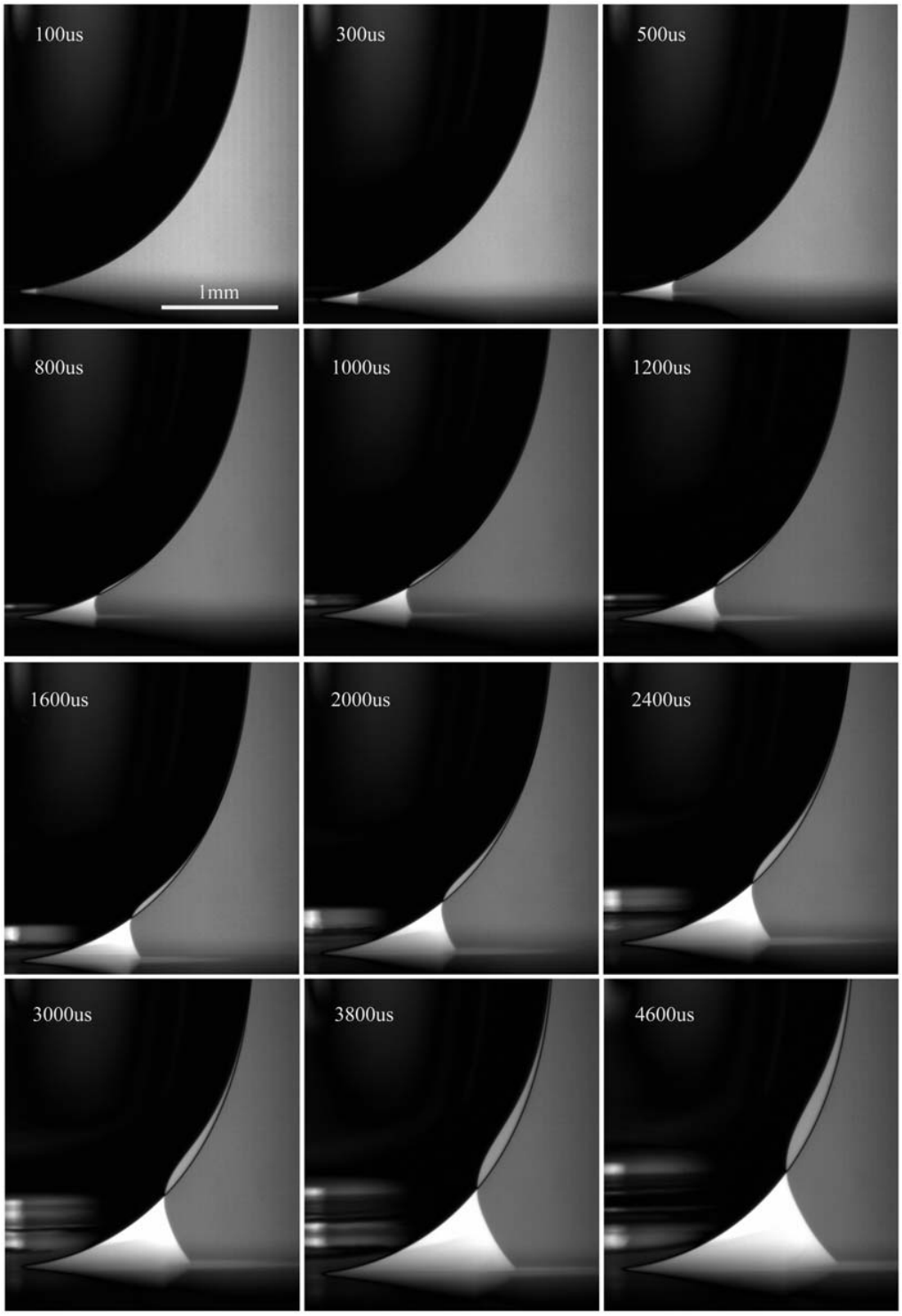

Figure 5-30: Coalescence of 80% glycerin onto water pool.

The curvature measurements in the neck region for all the experimental data are presented in figure 5-31. Here the radius of the inscribed circle has been normalized by the maximum horizontal radius of the stationary pendent drop, called R_{ave}.

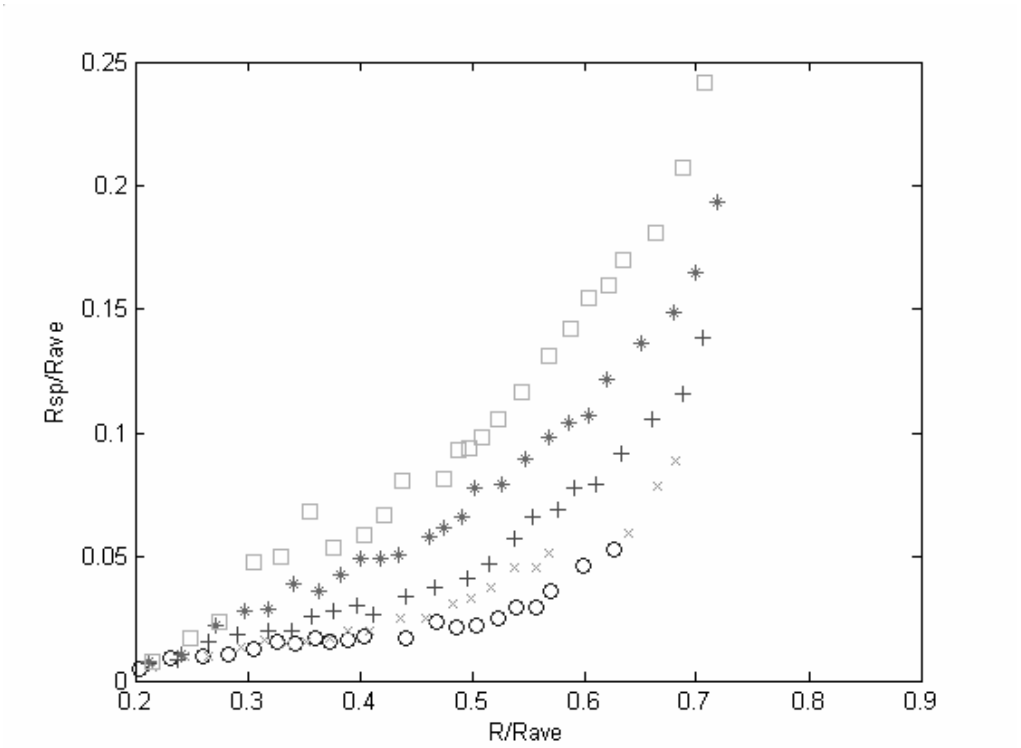

Figure 5-31: Variation in the radius of the inscribed circle in the neck region during the coalescence as the neck radius increases, For glycerin volume concentration of 80% (□), 85% (*), 90% (+), 95% (x) and 98% (○) and a water pool.

5.2.2 Effect of drop size on neck curvature

Similar experiments were conducted with tubes of different sizes, i.e. 4.75, 2.95, 1.85 and 0.88 mm, while keep the viscosity of the glycerin drop constant and high, by using 98% glycerin concentration by volume. The experimental images are presented in figures 5-32, 5-33 and 5-34. It is not difficult to see that the drop shapes during the coalescence are similar for the different size tubes, i.e. the curvature at the corner of

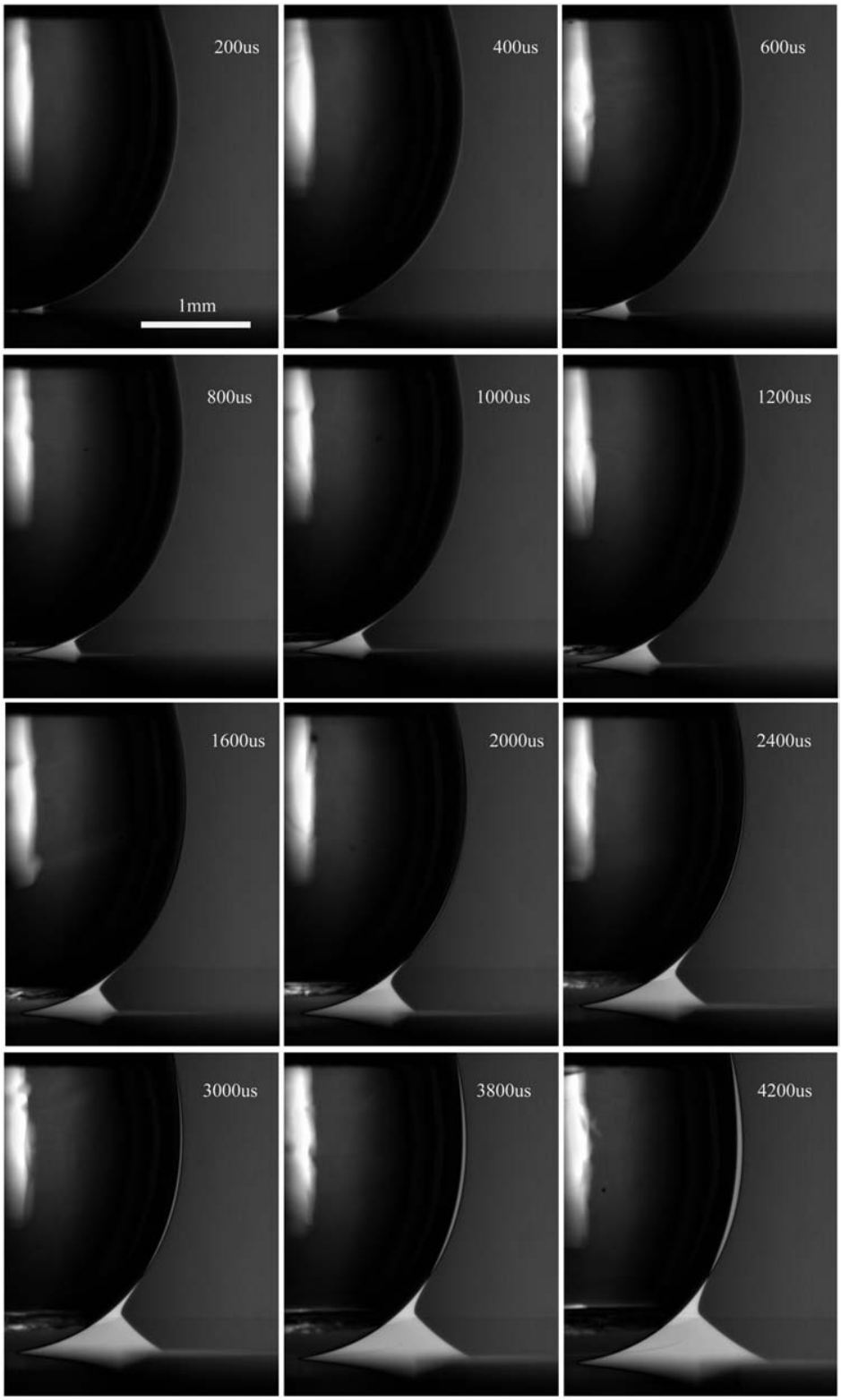

Figure 5-32: Coalescence of 98% glycerin/water mixture drop onto water pool, the needle used to produce the drop had outside diameter D=2.95 mm.

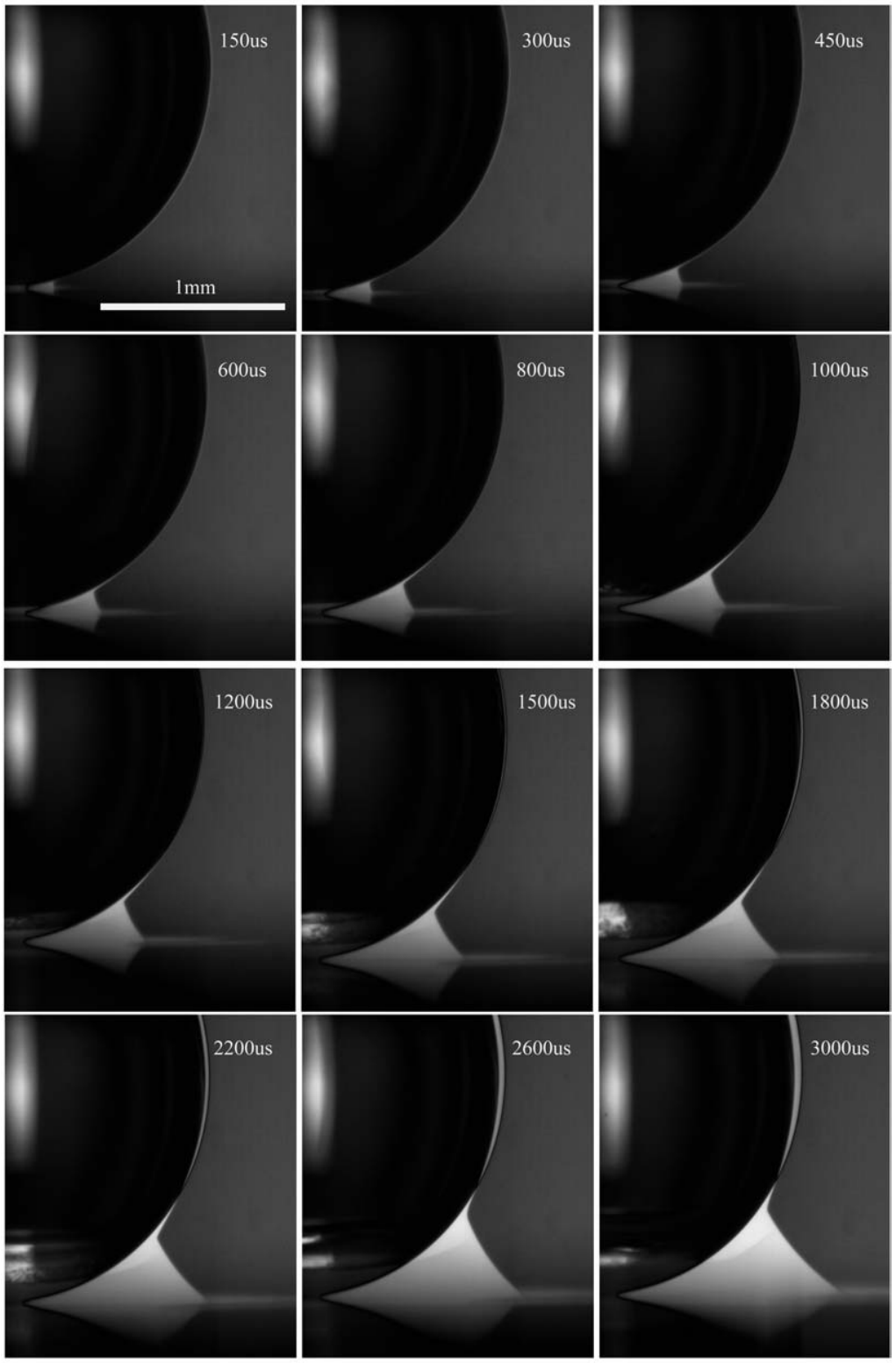

Figure 5-33: Coalescence of 98% glycerin/water mixture drop onto water pool, the needle used to produce the drop had outside diameter D=1.85 mm.

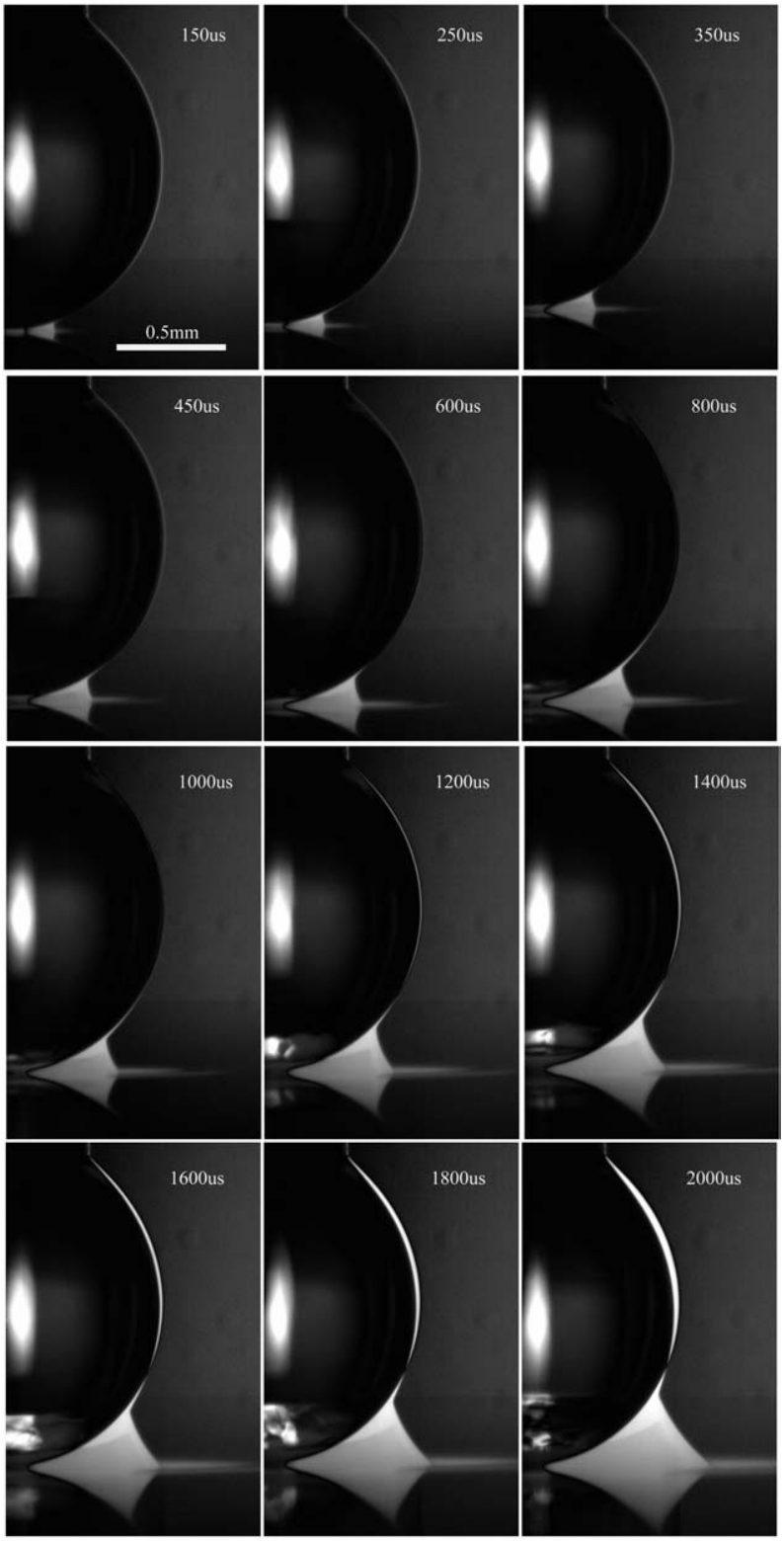

Figure 5-34: Coalescence of 98% glycerin/water mixture drop onto water pool, the needle used to produce the drop had outside diameter D=0.88 mm.

the neck region remains large and the drop shape does not show much distortion in the process.

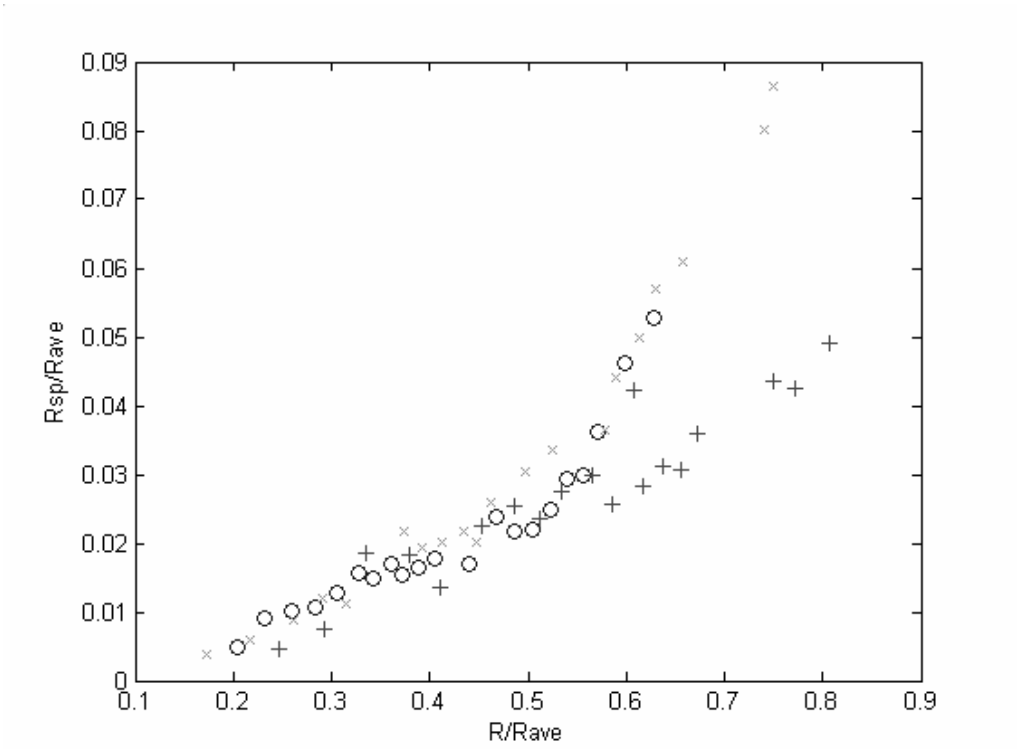

Figure 5-35: Radius of the inscribed circle in the neck region versus radius of the neck region, which is measure from coalescence of 98% glycerin drop generated with tube size of 4.75 mm (○), 2.95 mm (□) and 1.85 mm (+) with water pools.

Measurements of the radius of curvature R_{sp} are plotted in figure 5-35. The plot shows that the data points for tube 4.75 and 2.95 almost line on the same curve but a slight deviation in tube 1.85 when the neck region expanded to half R_{ave}. Also the curvature at the corner remains very large.

5.3 Glycerin/water drop coalescing with ethanol

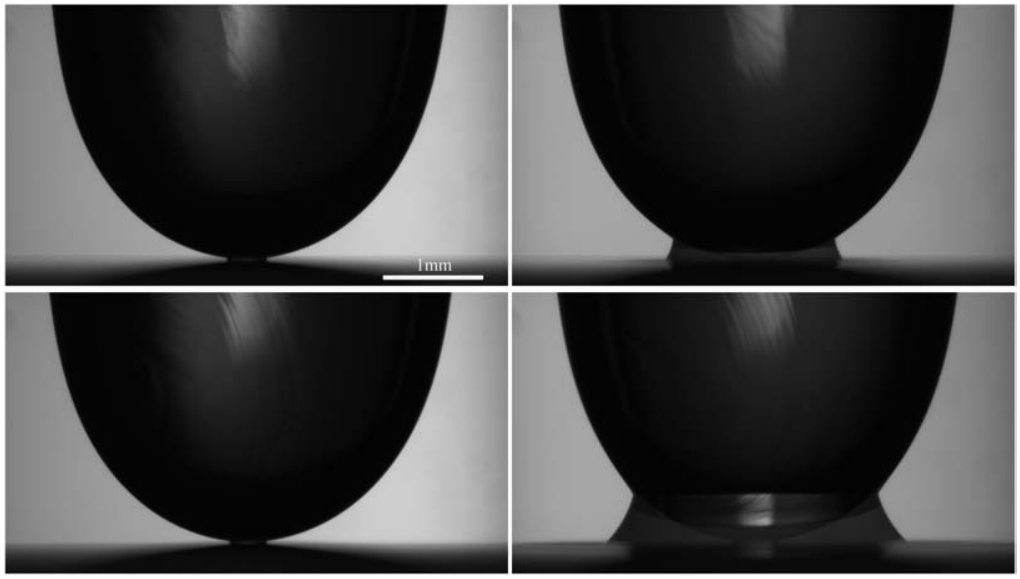

Figure 5-36: Shape of 98% glycerin/water drop coalescing onto a 94% ethanol/water pool, the left panel indicated the first contact and the right panels showed the coalescence shape 1600 μs (top) and 5000 μs (bottom) after first contact.

We also performed a set of experiments using a fixed pool mixture of 94% alcohol and 6% deionized water, while varying the viscosity of the drop liquid, by using water/glycerin mixtures for the drop. This setup, shown in figure 5-36, built up a large difference in both viscosity and surface tension between the drop, ranging from 65 to 73 dyne/cm, and the pool of about 25 dyne/cm. Marangoni forces generated by surface tension gradient are therefore always present in this set of experiments. However, the main variable here is the viscosity of the drop, which is varied by changing the volume concentration of glycerin/water solution. This set of experiments aims to investigate how the viscous forces overpower the Marangoni wave.

Figure 5-37, 5-38 and 5-39 show the resulting surface profiles. Images are again contrasted to the static drop shapes to highlight the waves and surface

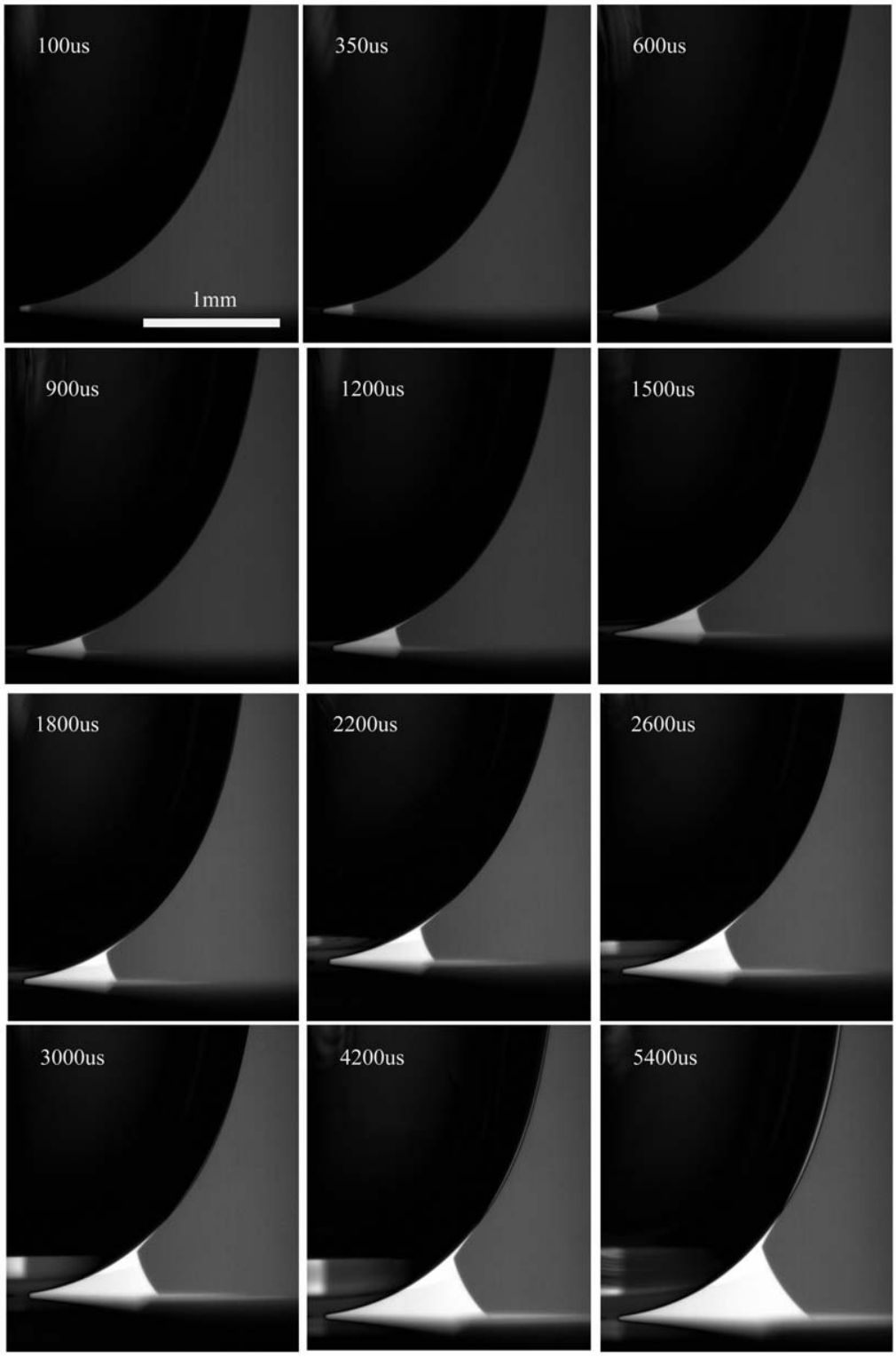

Figure 5-37: Evolution of coalescence of 98% glycerin/water drop onto 94% ethanol/water solution pool, the needle size generating the drop is D=4.75 and hung above H=?mm from the bottom liquid surface.

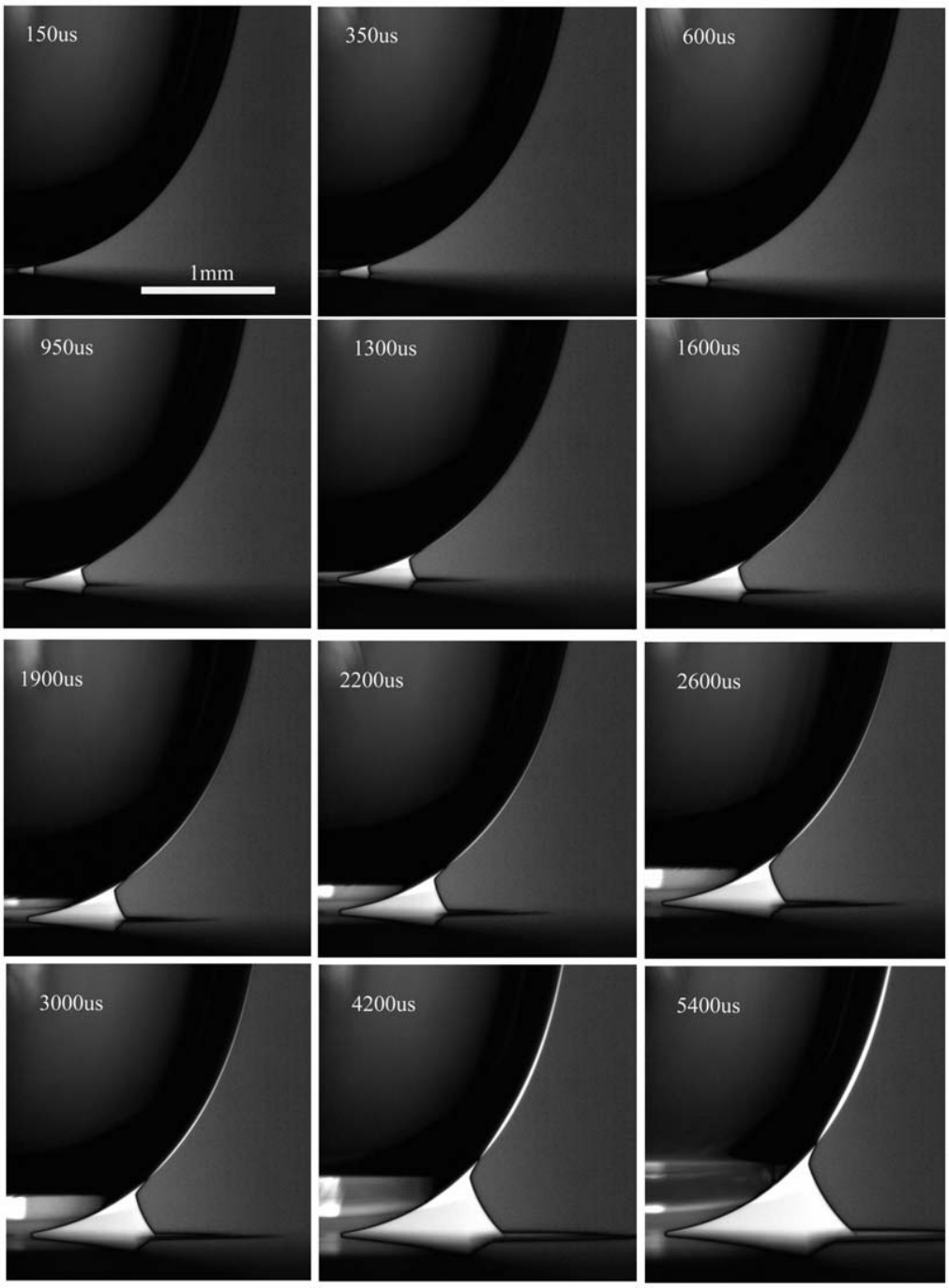

Figure 5-38: Evolution of coalescence of 90% glycerin/water drop onto 94% ethanol/water solution pool, the needle size generating the drop is D=4.75 mm.

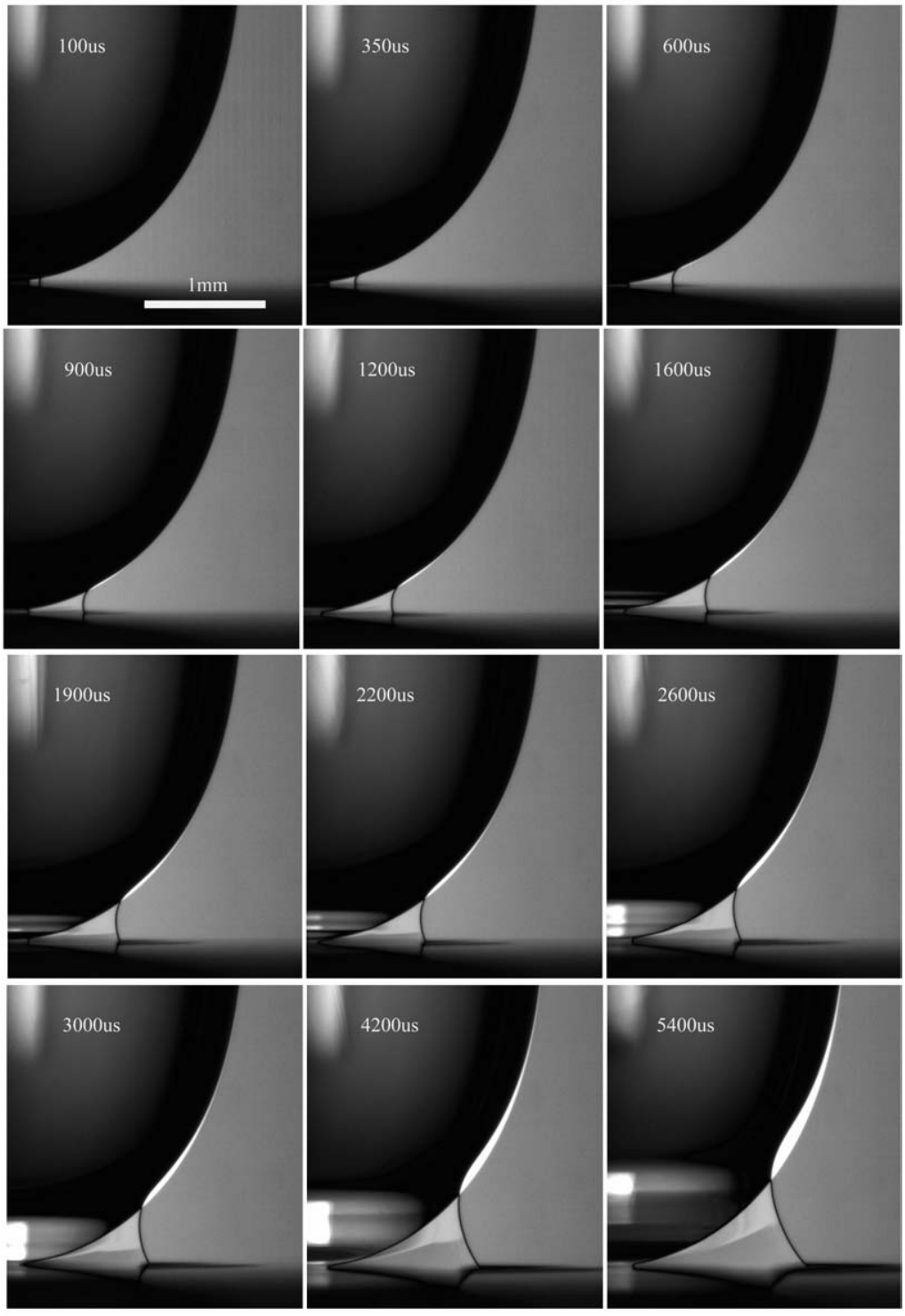

Figure 5-39: Evolution of coalescence of 70% glycerin/water drop onto 94% ethanol/water solution pool, the needle size generating the drop is D=4.75 mm.

deformations. Marangoni waves, so prominent in coalescences of water/ethanol, are invisible on the drop surface for the high viscosities. The high viscosities suppress these waves and the pool liquid moves up the drop as if it were wetting a solid surface. The corner at the advancing 'contact line' is so sharp that the pixel resolution of the image is in some cases insufficient to resolve the shape, which suggests that the radius of curvature is less than 5 μm. The total curvature at the free surface is therefore maximum in this region. Lowering the viscosity, the drop shape becomes progressively smoother in the corner and the drop deforms more compared to the much higher viscosity drops.

Similar experiments were performed with various size drops by changing the tube, while fixing the viscosity of drop liquid in volume concentration of 98% glycerin. The experimental results are presented in figure 5-40, 5-41 and 5-42. The general behaviors during the coalescence are similar, with the highest curvature always at the corner of the neck region.

In other words, the behavior is very similar for the viscous drops, whether they are coalescing with a pool of water or a pool of ethanol. Marangoni waves do not play a significant role here.

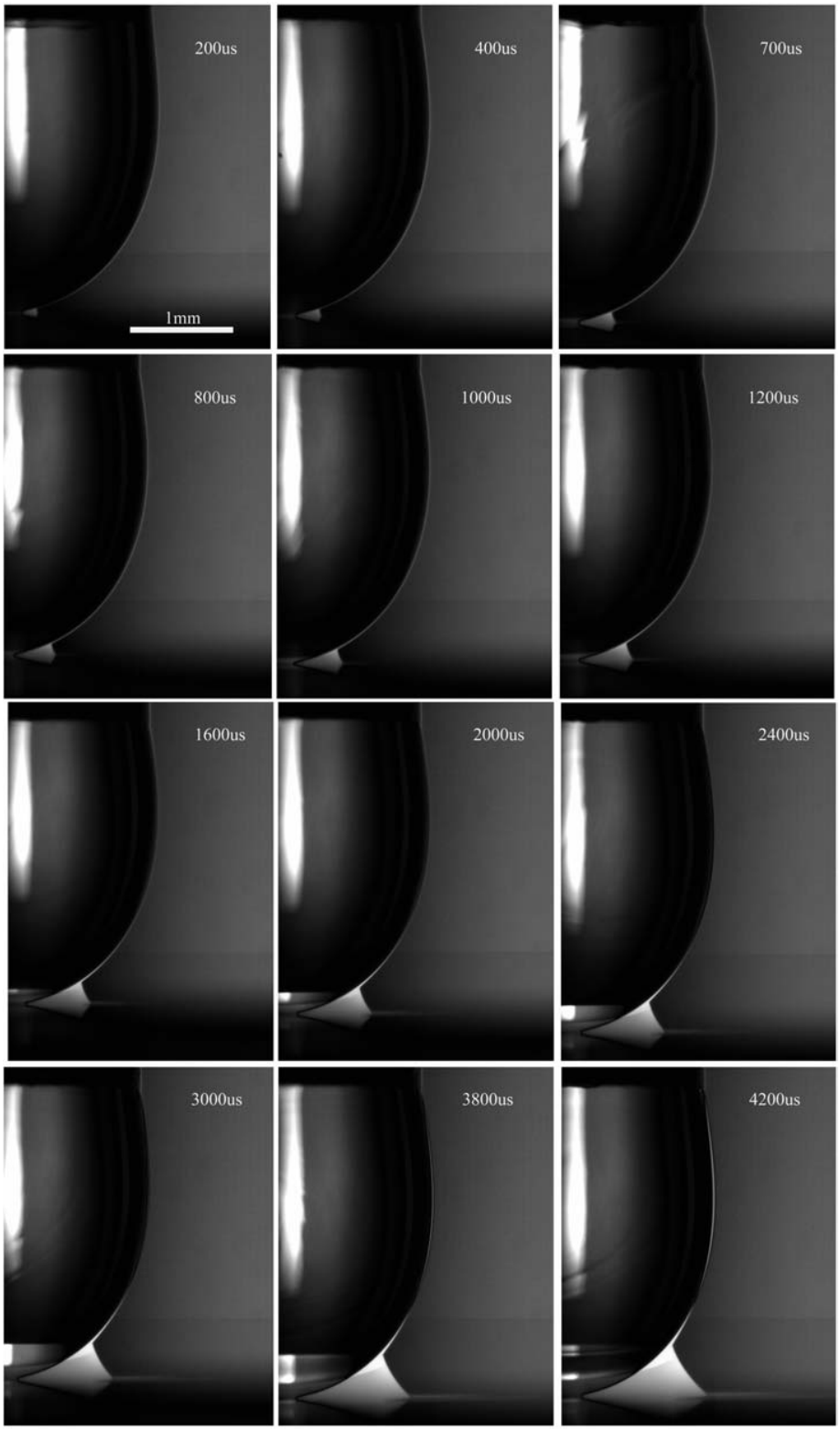

Figure 5-40: Evolution of coalescence of 98% glycerin/water drop onto 94% ethanol/water solution pool, the needle size generating the drop is D=2.95 mm.

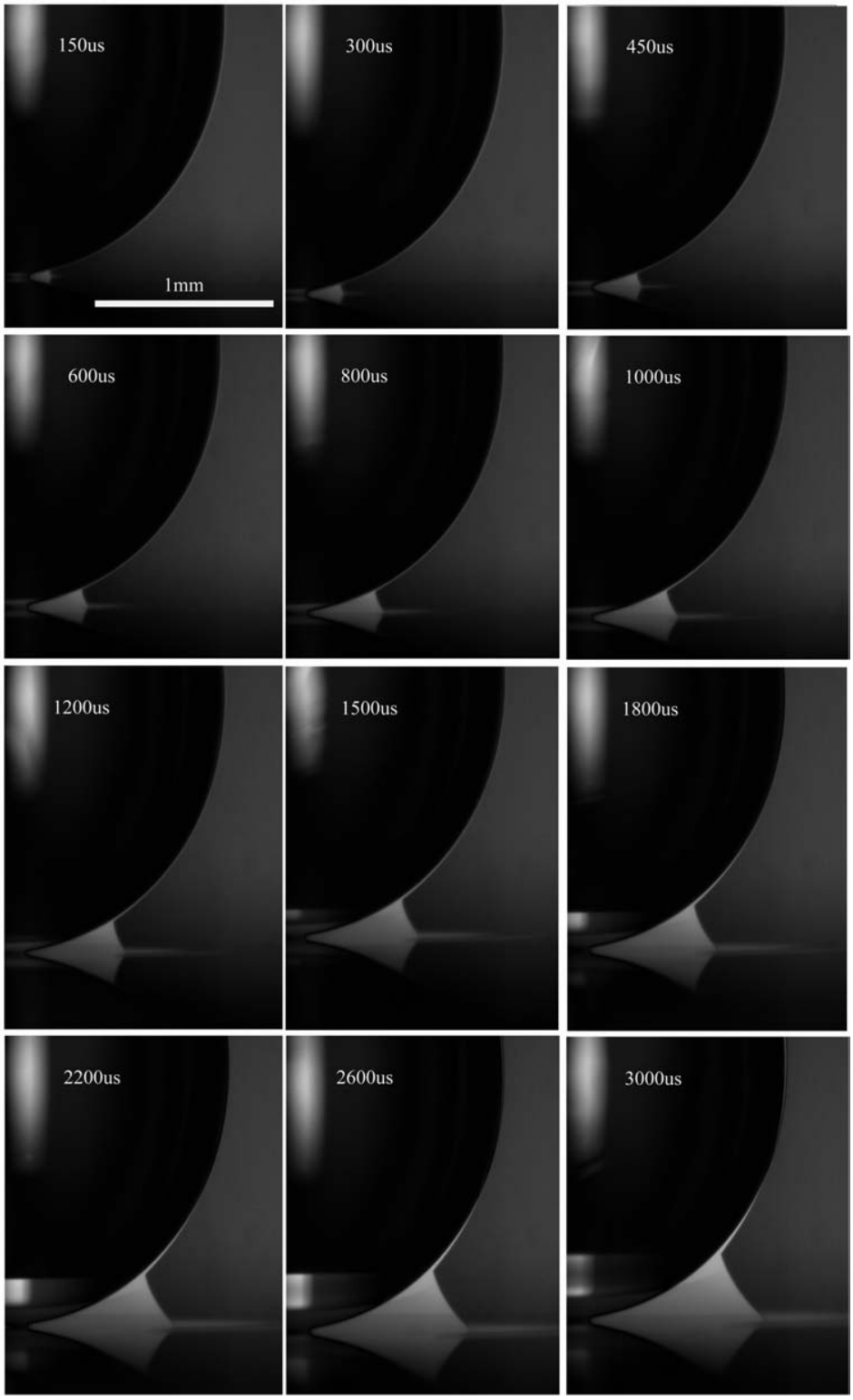

Figure 5-41: Evolution of coalescence of 98% glycerin/water drop onto 94% ethanol/water solution pool, the needle size generating the drop is D=1.85 mm.

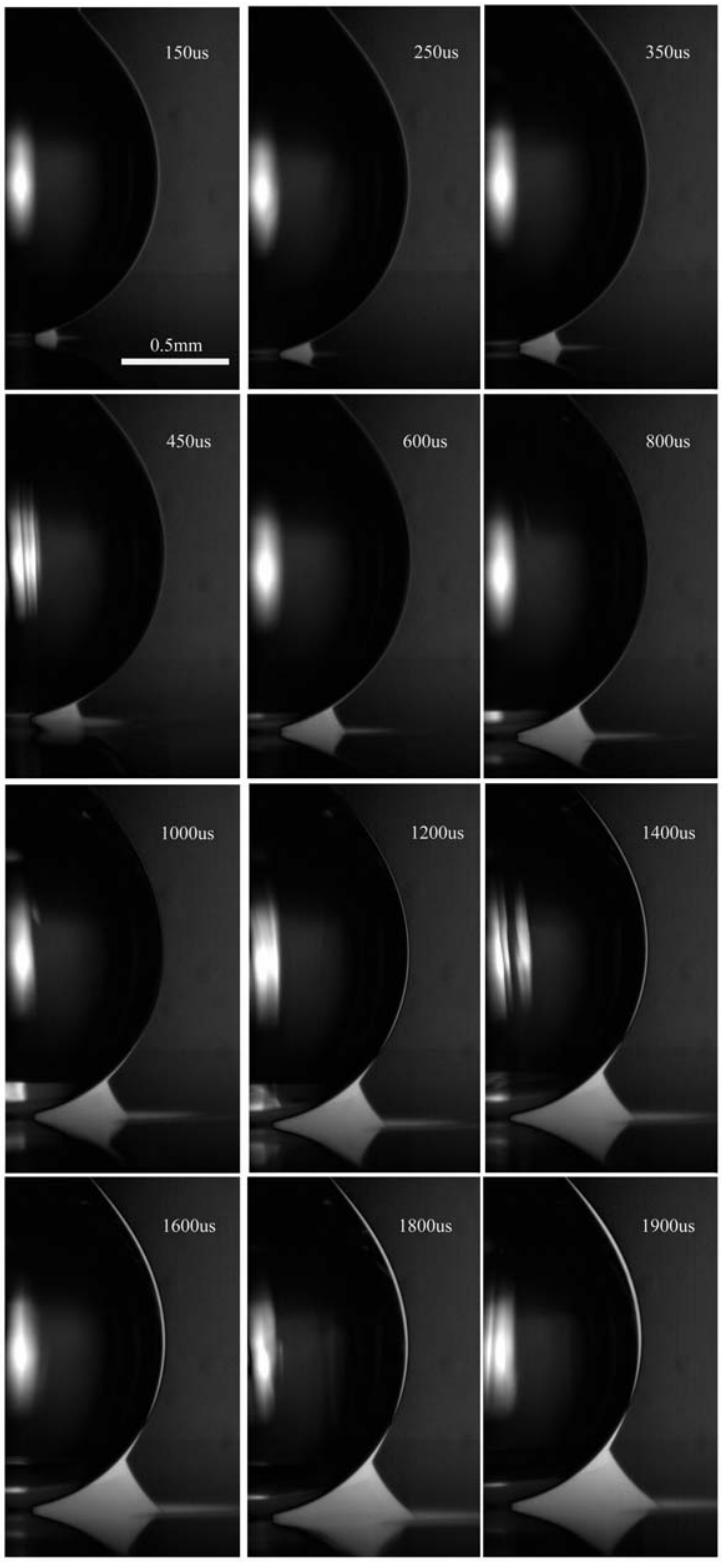

Figure 5-42: Evolution of coalescence of 98% glycerin/water drop onto 94% ethanol/water solution pool, the needle size generating the drop is D=0.88 mm. Note that the horizontal extent of the panels is only slightly more than 1 mm.

5.4 Effect of Surfactants on the drop coalescence

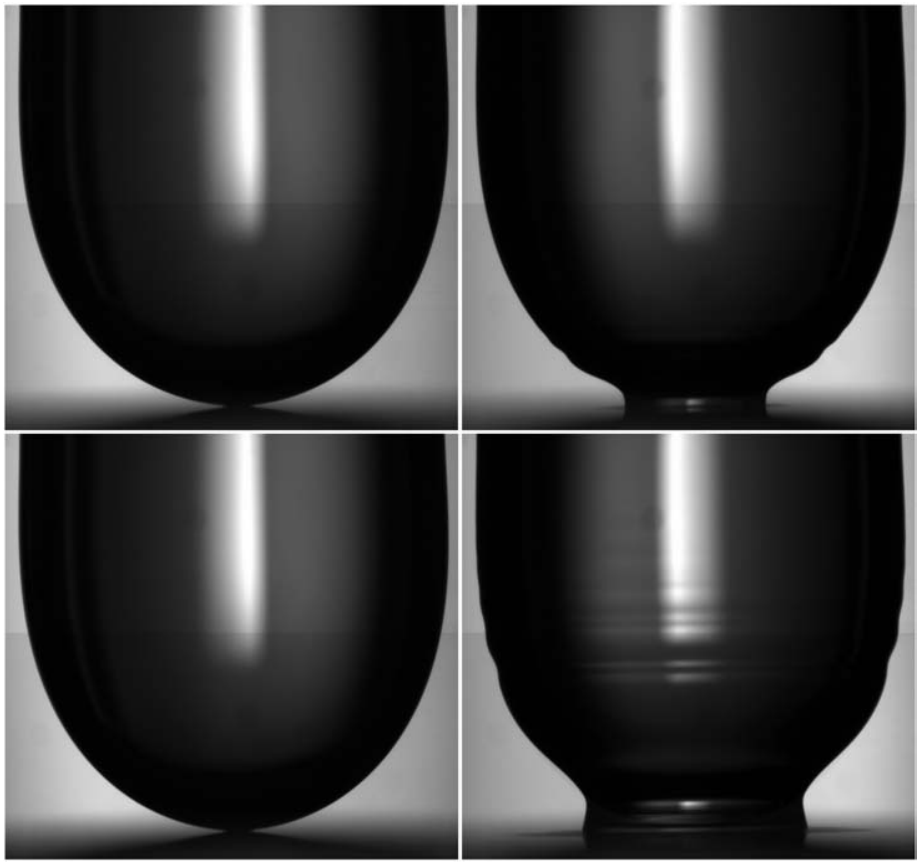

Figure 5-43: Coalescence of water drop onto 1 CMC Triton-X100 solution pool, the top and bottom panels show the shape of coalescing drop 900 and 2400 us after initial contact.

Surfactants are molecules which have an affinity for air-water interfaces. The most common example of such molecules is soap. Soap molecules have a hydrophilic head and a hydrophobic tail. Owing to this molecular structure, they find it energetically favorable to sit at a free surface with their tails sticking out of the water. Their presence at the free surface reduces the surface tension, which helps with the washing process. Therefore, gradients in surfactant concentration along the surface give rise to surface tension gradients, which can drive flow along the free surface. Surfactants thus generate a special class of Marangoni flows. There are many different types of surfactants, some of which are insoluble (and so remain on the

surface), others which are soluble in the suspending fluid (in our case the water) and can therefore diffuse into the bulk liquid. For a wide range of common surfactants, surface tension is a monotonically decreasing function of concentration until a critical concentration is achieved. This concentration goes by the name 'critical micelle concentration' (CMC). At this concentration the entire surface is loaded with a single layer of the surfactant molecules and starts to form micelles, which are little spherical collections of molecules inside the bulk liquid. In these micelles the tails are bunched together in the middle of the micelle, away from the surrounding water. For concentrations higher than CMC, the value of σ remains constant, at the lowest value. The principal dynamical influence of the surfactants is to impart an effective elasticity to the interface. The presence of the surfactants will serve not only to alter the normal stress balance (through the reduction of σ), but also change the tangential stress balance (through the generation of Marangoni stresses) when the interface is stretched. The presence of surfactants will act to suppress any fluid motion characterized by positive surface divergence. For example, consider a fluid motion characterized by a surface flow radially divergent from a point. The presence of the surfactants results in the redistribution of surfactants, with lower surfactant concentration at the central point of divergence. Therefore, Γ will be reduced near this. The resulting Marangoni stresses act pull the surface motion back towards the central point, thus suppressing this motion, resisting it through an effective surface elasticity. Similarly, if the flow is characterized by a radial convergence, the resulting accumulation of surfactant in the region of convergence will result in Marangoni stresses that serve to resist it. Such flow may also lead to buckling of the surfactant layers. It is this effective elasticity that gives soap films their longevity. Everyone has seen the long-lasting soap bubbles, which can last for many seconds or even minutes without breaking. The divergent

motions that would cause a pure liquid film to rupture are here suppressed by the surfactant layer on the soap film surfaces.

To investigate the effects of these dynamical properties of surfactants on the coalescence, we performed experiments of the coalescence of a water drop with a water pool containing surfactant Triton X100 and the experimental results are show in figure 5-43. Measurements of the traveling wave on the drop surface were done as before and are shown in figure 5-44.

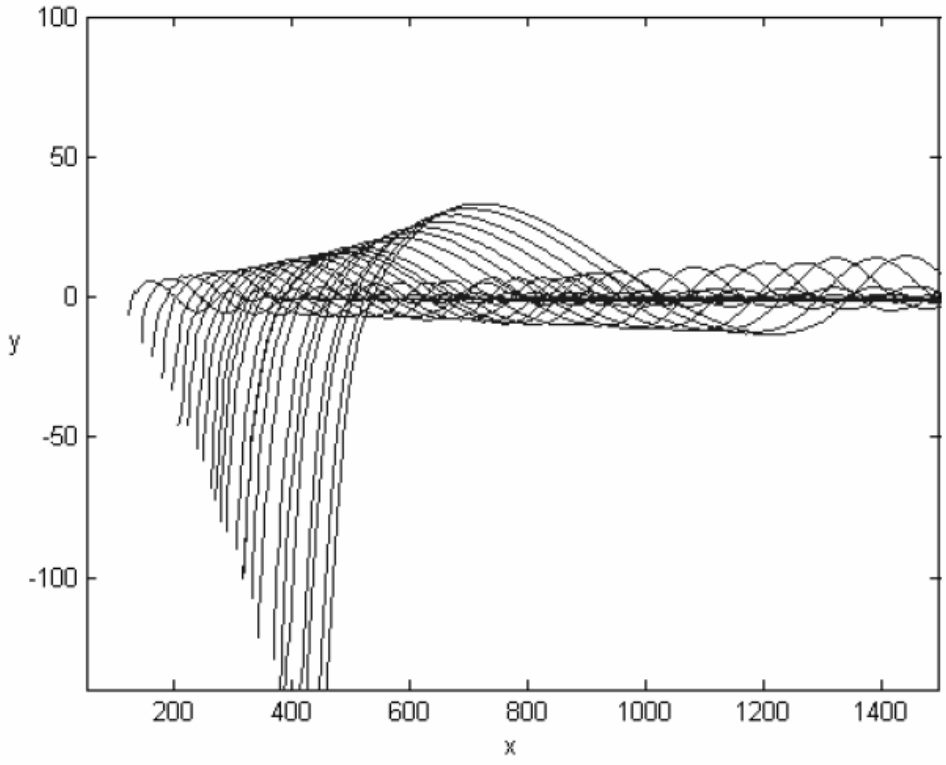

Figure 5-44: The wave amplitude normal to the drop surface measured from coalescence of water drop onto a water pool in addition of surfactant Triton X100 by volume concentration of 1 CMC.

The behavior of the wave motion during the coalescence with surfactant Triton X100 is similar to that of coalescence of water/water shown in figure 5-45 and 5-12, which presents only one obvious wave near the corner of liquids contacts following by some tiny waves. However, more visible tiny wave appear on the drop surface with addition

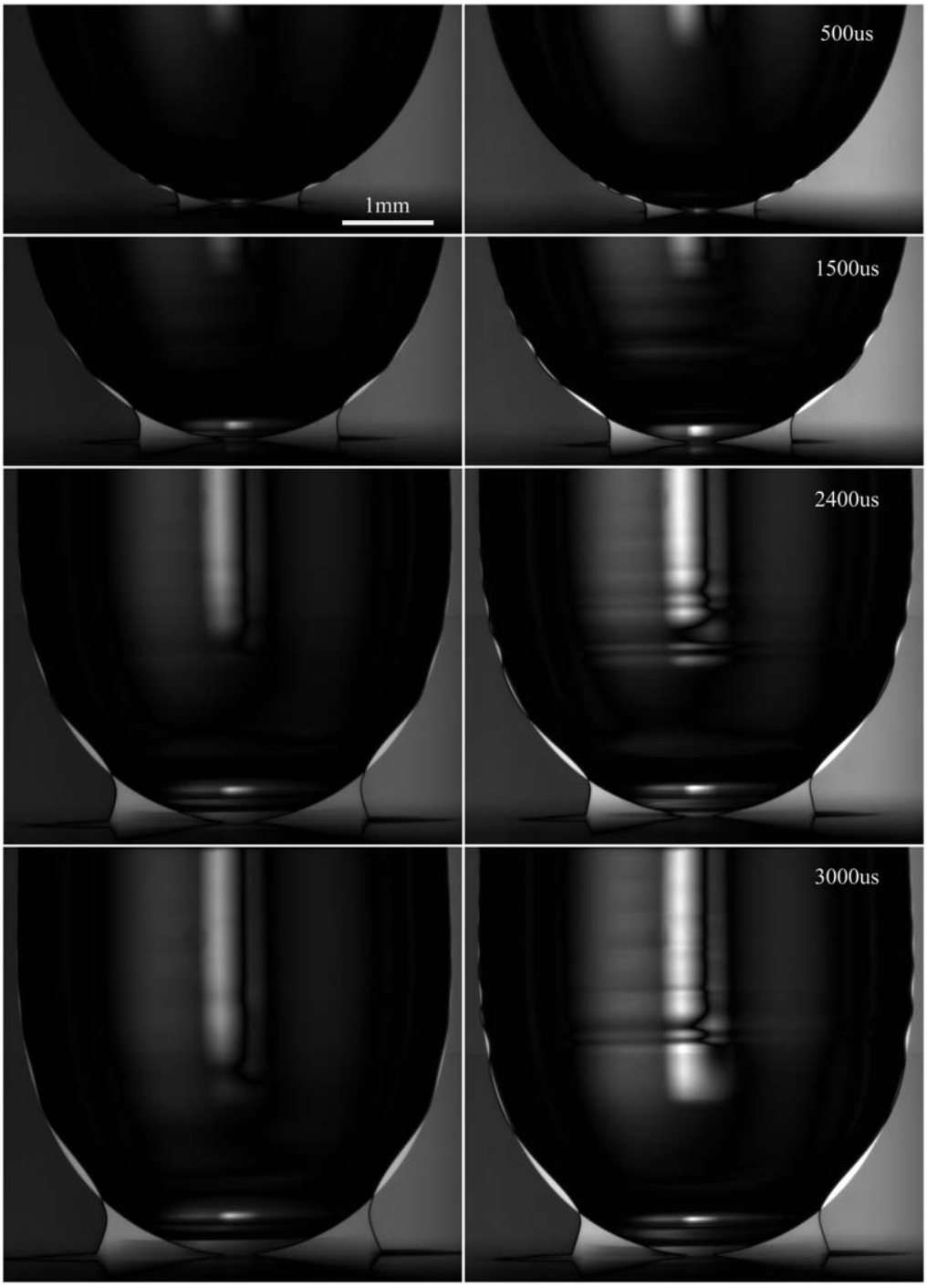

Figure 5-45: Comparison between water drop coalescing onto pure water pool and water solution in addition of surfactant Triton-X100.

of surfactant, because of the wave length except for the first wave is shorter. And the amplitude of first wave in coalescence with surfactant is significantly suppressed.

Comparison to the figure 5-11 for coalescence of water/ethanol shows that the wave appearing on the coalescence with surfactant is not only dampened in wave amplitude but also stretched in wave length.

5.4.1 Effect of Critical Micelle Concentration on drop coalescence

To investigate how variations of surfactant concentration affect the coalescence, 10 CMC surfactant solutions were also tested, for identical configurations used for the 1 CMC experiments. The experimental results are shown in figures 5-47 and 5-48 and the wave profiles are plotted in figure 5-46. No significant difference was observed in comparison of both experimental results with the two concentrations. Only a slight weakening of wave amplitude is seen in coalescence with the 10 CMC concentration.

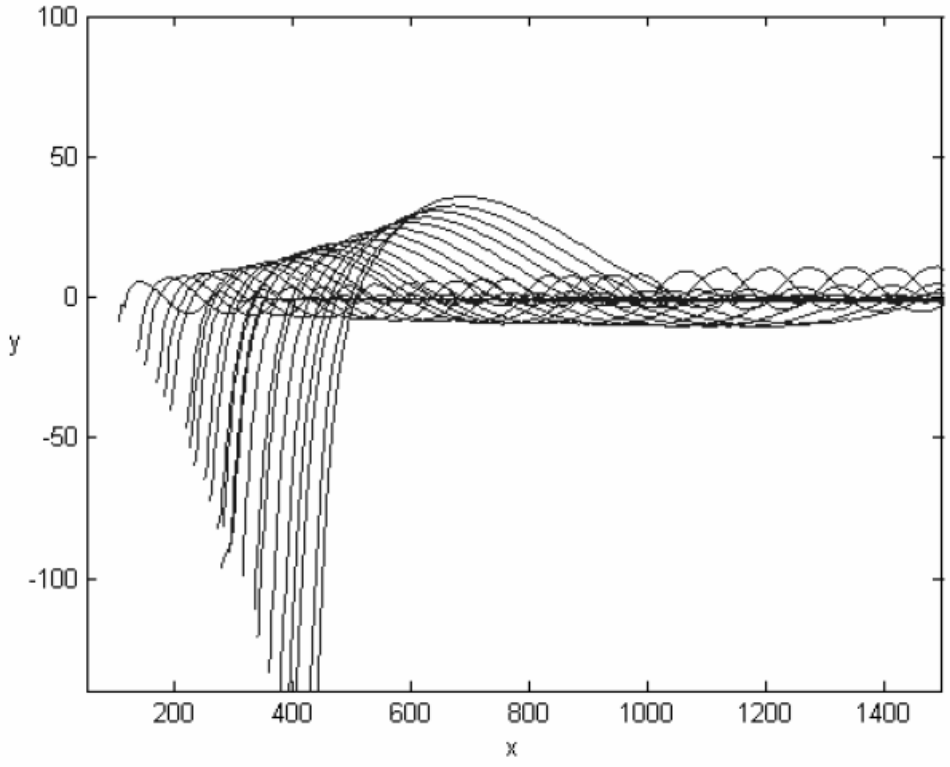

Figure 5-46: The wave normal to the drop surface measured from coalescence of water drop onto a water pool in addition of surfactant TritonX100 by volume concentration of 10 CMC.

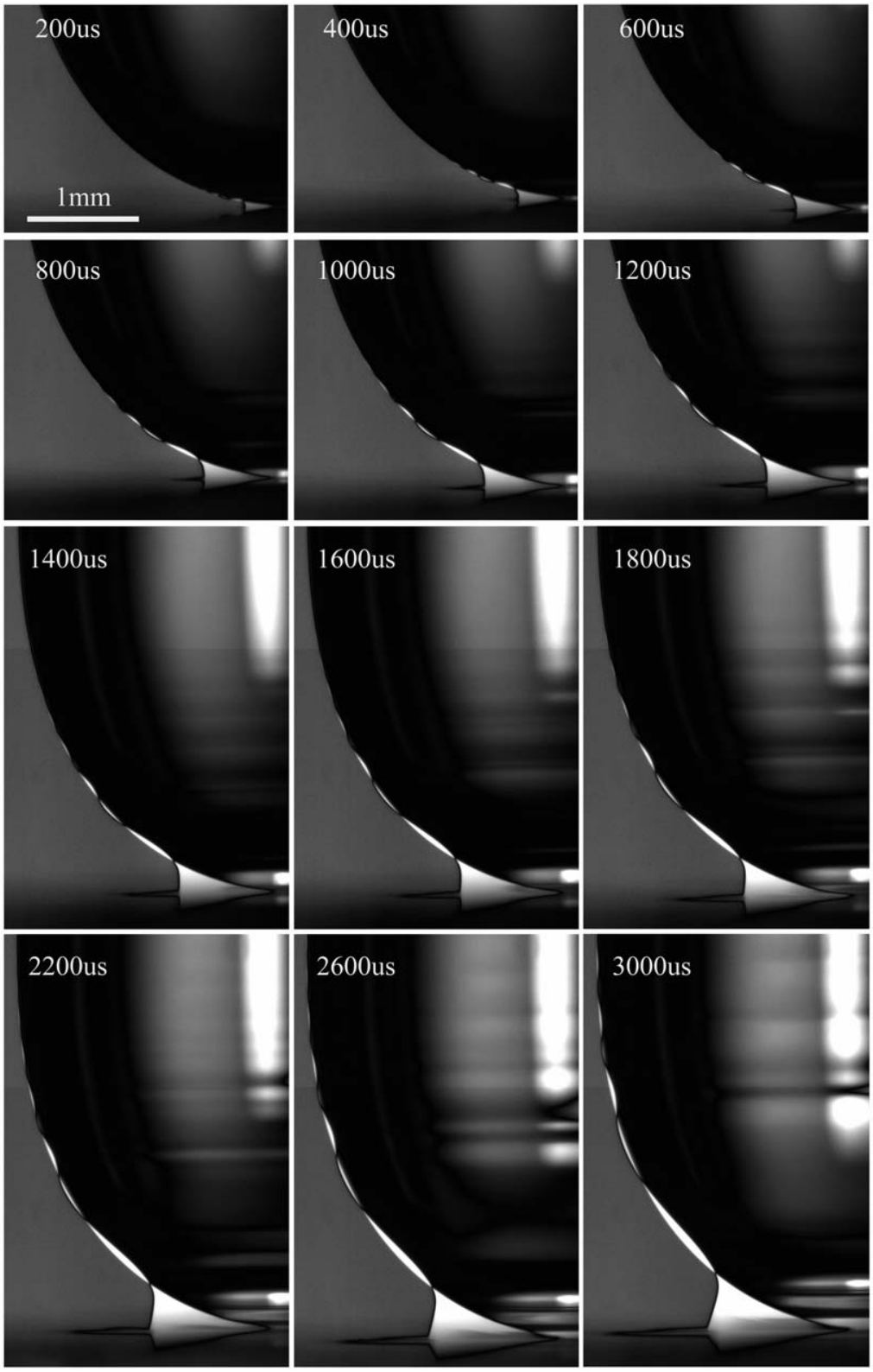

Figure 5-47: Coalescence of water drop onto 1 CMC surfactant (Triton-X100) water solution.

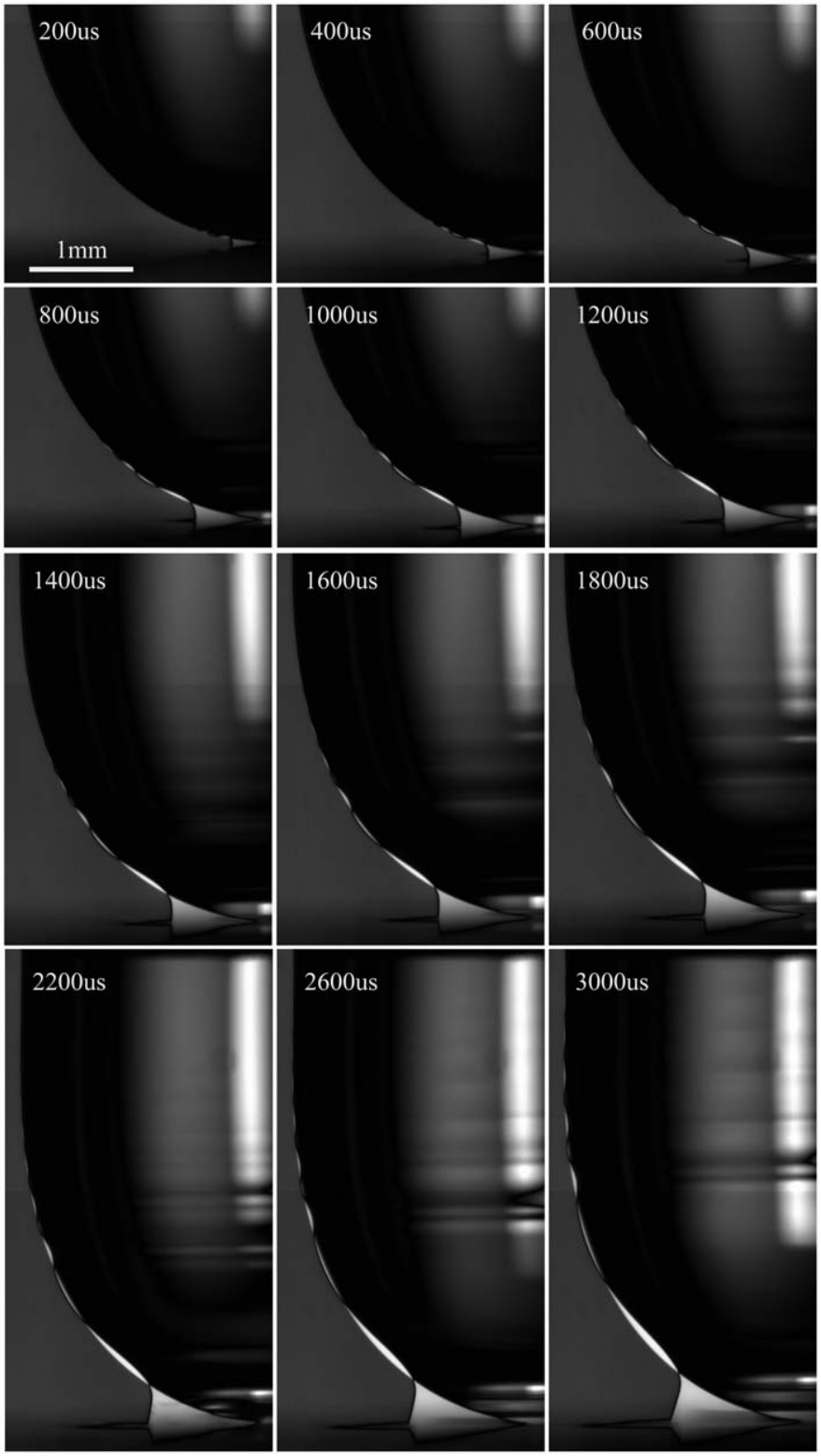

Figure 5-48: Coalescence of water drop onto 10 CMC surfactant (Triton-X100) water solution pool.

5.5 The wave underneath the pool surface

The results presented in the earlier sections of chapter 5, all show the drop surface shape above the pool liquid. However, there are also deformations of the pool liquid below the original flat surface. Most of the liquid going into the expanding neck region is pulled up from the pool liquid. This is especially true for the very viscous drops, as is clearly seen in the Fluorescein images. Due to the incompressibility of water, this liquid must *dig* a trough into the bottom pool to match the volume of liquid pulled up. To investigate this we conducted a separate set of experiments, where we observed the shape of the wave underneath the pool surface. These results will be presented together in this section, rather than splitting them up into the various earlier sections of this chapter.

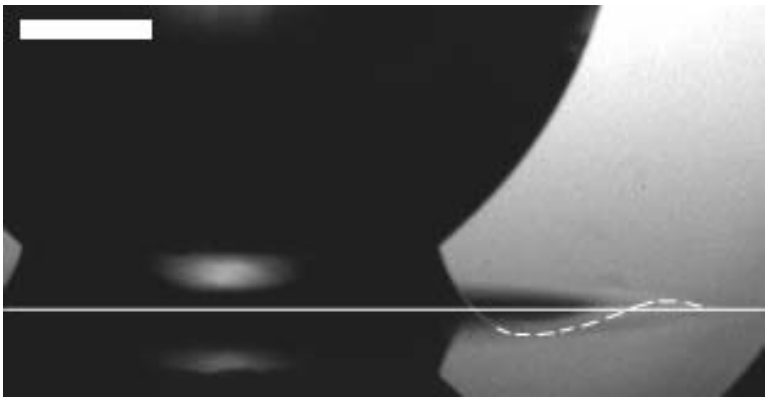

Figure 5-49: The proposed shape of the wave underneath the pool surface during the coalescence of a very viscous drop onto a low-viscosity liquid. The horizontal line shows the original pool surface.

Figure 5-49 shows the proposed bottom shape of the coalescence wave underneath the pool surface, sketched onto an image taken above the pool liquid. To investigate this wave structure we use a view which is horizon slightly underneath the free surface. The horizontal dark region marks the depth of the trough of the capillary

Figure 5-50: The shape of the wave underneath the pool surface during the coalescence of a water drop onto ethanol/water mixture pool. The horizontal white line marks the location of the original pool surface, which can be determined from the first image in the image-pair.

wave during the coalescence. This wave is axisymmetric and therefore in the horizontal view appears as a horizontal dark region across the center-line of the contact. This wave-trough advances radically outwards from the location of the first contact.

For the coalescence of a water drop with an ethanol pool an interesting cone-like tongue of water was observed to penetrate into the pool of ethanol, see figure 5-50. This cone is made visible by the large difference in the refractive index of the two liquids. This cone is pulled down by the coalescence dynamics in the neck region.

Figure 5-51 shows that the tip of the tongue moves down at a constant speed of about 10 cm/s. The density difference, between the heavier water on top and the

lighter ethanol in the bottom, is not responsible for this motion, as is clear from the broken curve in the figure, which shows the gravity driven speed of free-fall from rest $H = 0.5gt^2$, even when we have ignored the buoyancy. Figure 5-52 shows the depth of the capillary wave trough traveling outwards on the flat surface of the ethanol pool. The depth δ appears to approach a constant of about 0.15 mm, at the end of the coalescence process.

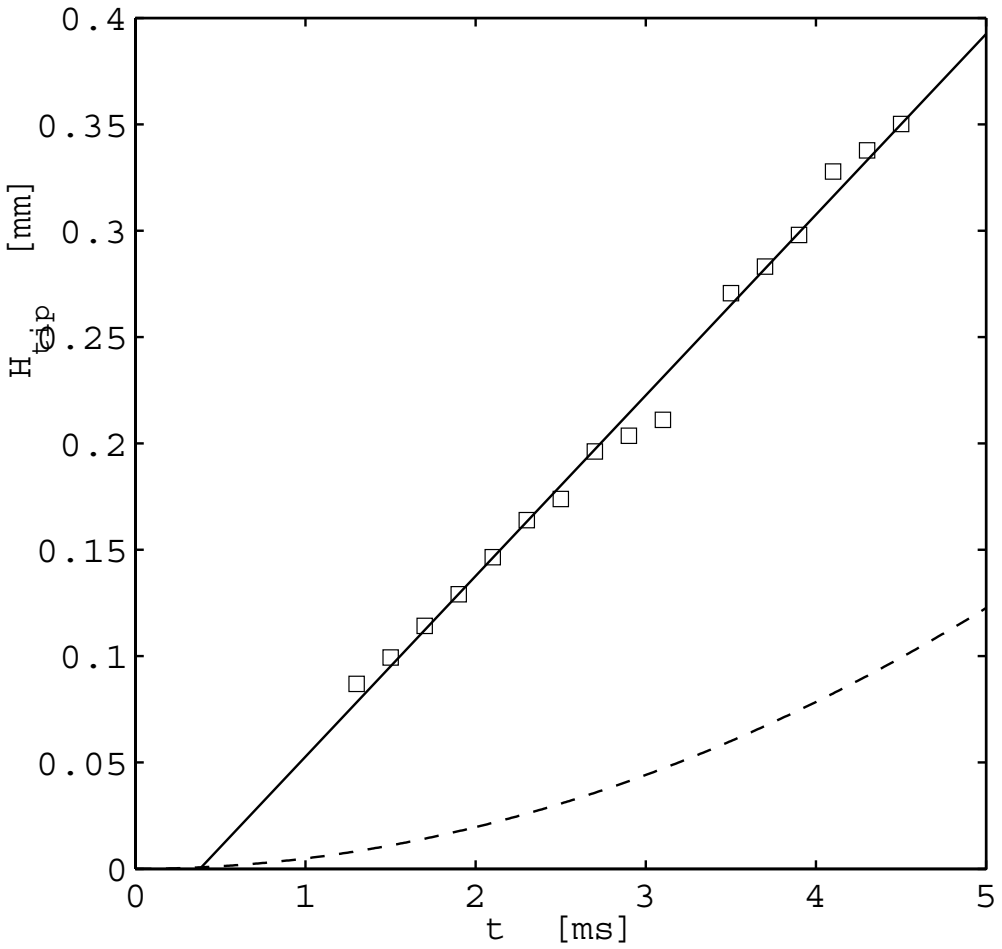

Figure 5-51: The depth of the tip of the water cone in previous figure vs. time from first contact, the broken line shows the free-fall curve.

For the very viscous drops the drop fluid is too viscous to be pulled down into such a cone. The results are shown in figures 5-53 and 5-54, not revealing any cone

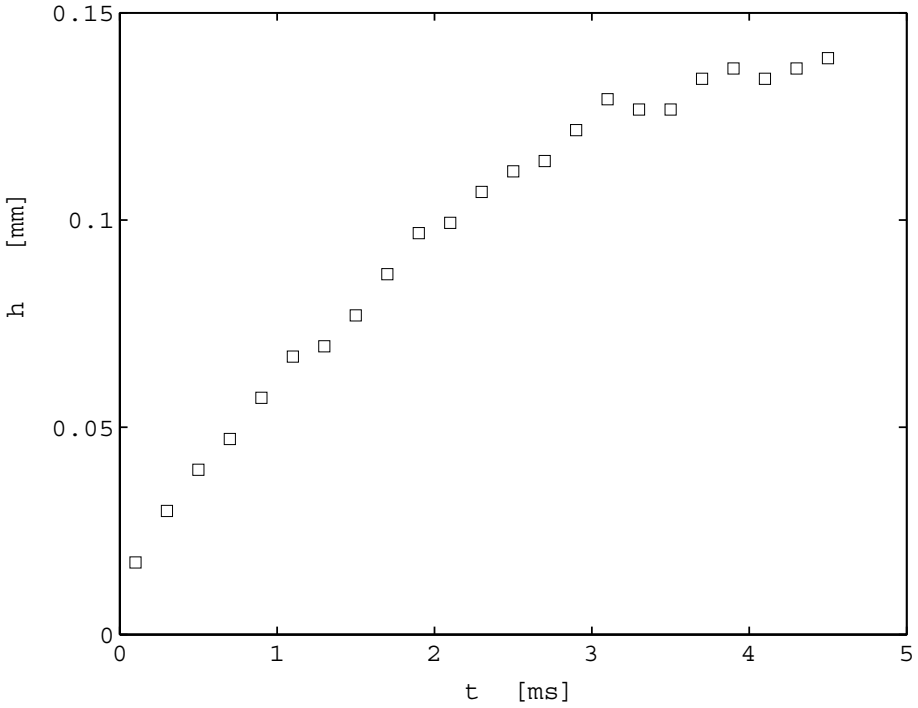

Figure 5-52: The depth of the free-surface trough traveling outwards following from the axis of symmetry. For the same conditions as in the previous figure.

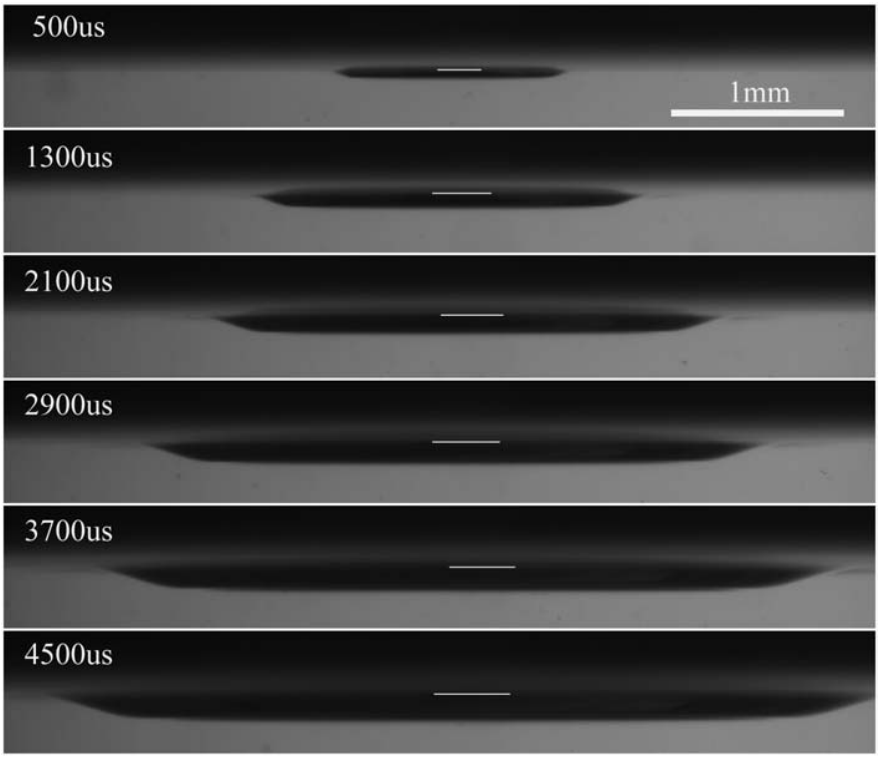

Figure 5-53: The underneath pool-shape for the coalescence of 98% glycerin/water drop with a flat water surface.

of drop fluid penetrating into the pool. The depth of the trough has been measured as a function of time and the radial extent of the axi-symmetric wave. Figure 5-55 shows the aspect ratio of the trough, i.e its depth δ as a function of its radial location. The radial location is measured to the radius where the depth of the trough is maximum. This was measured for the most viscous drop, both for a pool of water and a pool of alcohol.

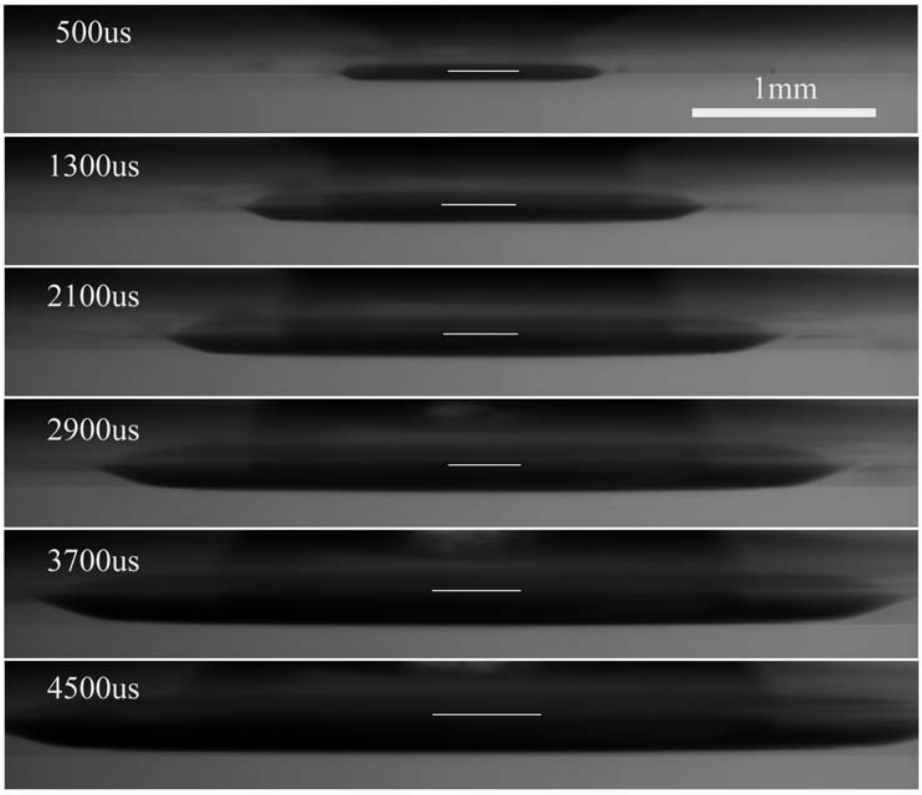

Figure 5-54: The underneath shape of coalescence of 98% glycerin/water drop onto ethanol/water mixture pool.

The results show that the aspect ratio for the two cases is identical, i.e. both follow a linear relation in figure 5-55. The proportionality constant show that the maximum depth δ increases linearly with radial distance, as

$\delta = 0.059\ R_o$.

or about 6% of the radius.

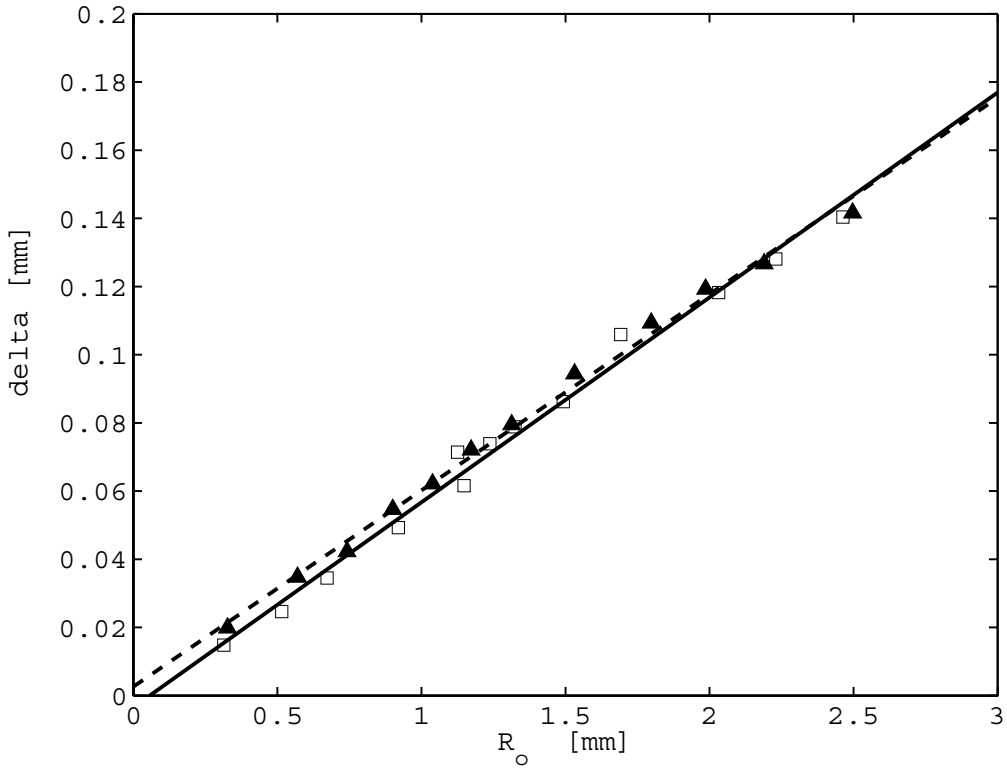

Figure 5-55: The depth of trough vs. radius, for the coalescence of a 98% glycerin drop with a water surface □ and an alcohol surface Δ. The average of the two best-fit slopes gives the relationship $\delta = 0.059\ R_o$.

6 Discussion

6.1 Self-Similarity of the Marangoni waves

Motivated by the theoretical work of Keller and Miksis (1983), we decided to investigate the possibility for self-similar characteristics for the Marangoni wave motions along the drop. Figures 6-1 to 6-4 show the wave shapes for the four different tubes. To highlight the self-similar nature of the wave-shapes we have added lines, marking the maxima and minima in the wave crests and troughs. Keep in mind that these plots do not give direct information about the time associated with each curve.

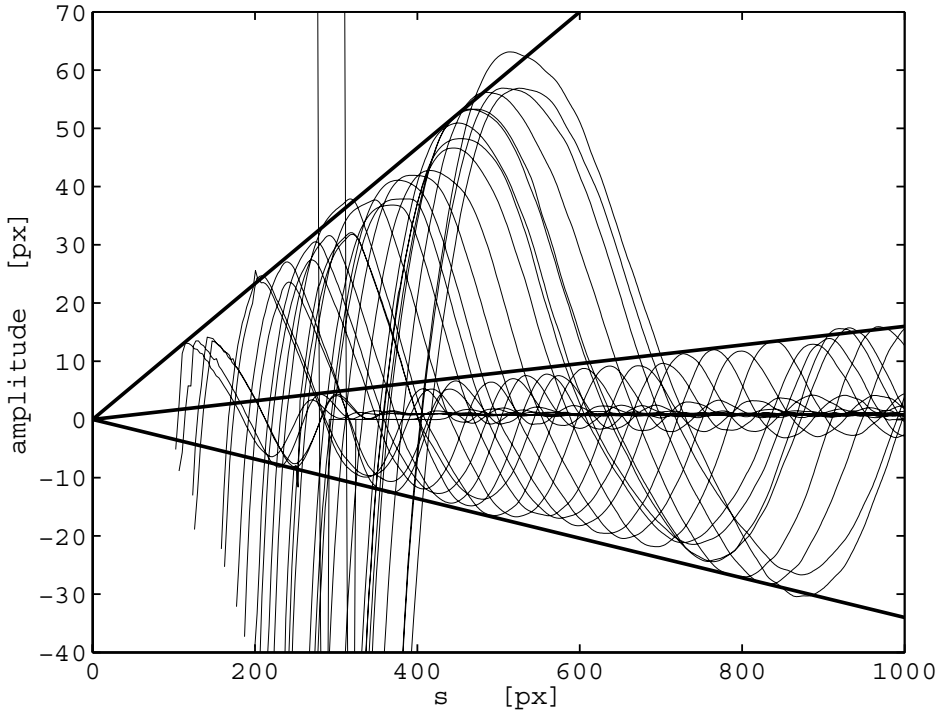

Figure 6-1: The Marangoni wave shapes for the largerst needle D = 4.75 mm.

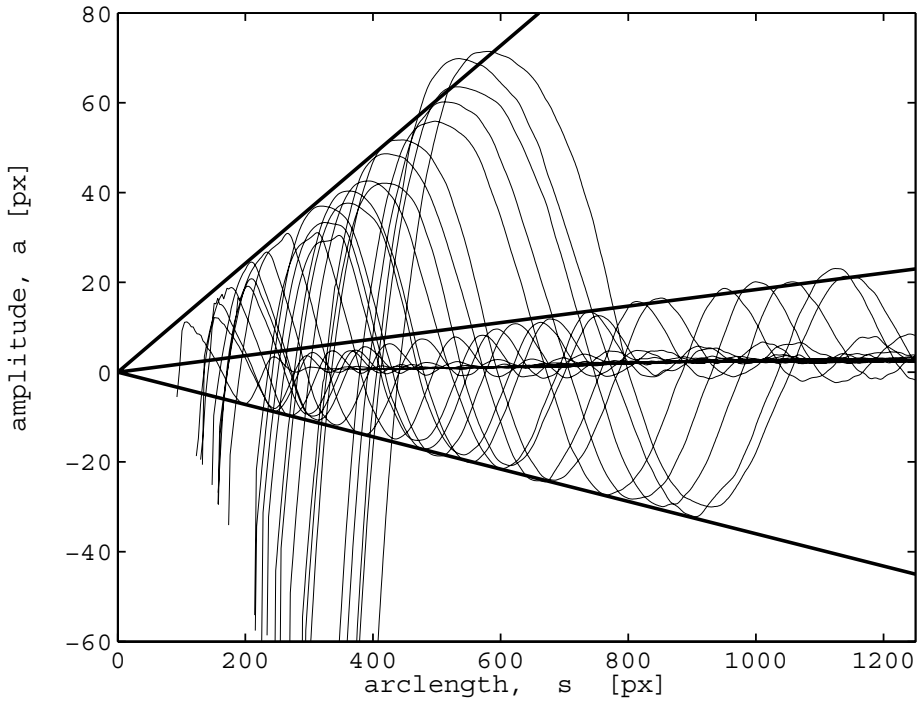

Figure 6-2: The Marangoni wave shapes for the second largerst needle D = 2.95 mm.

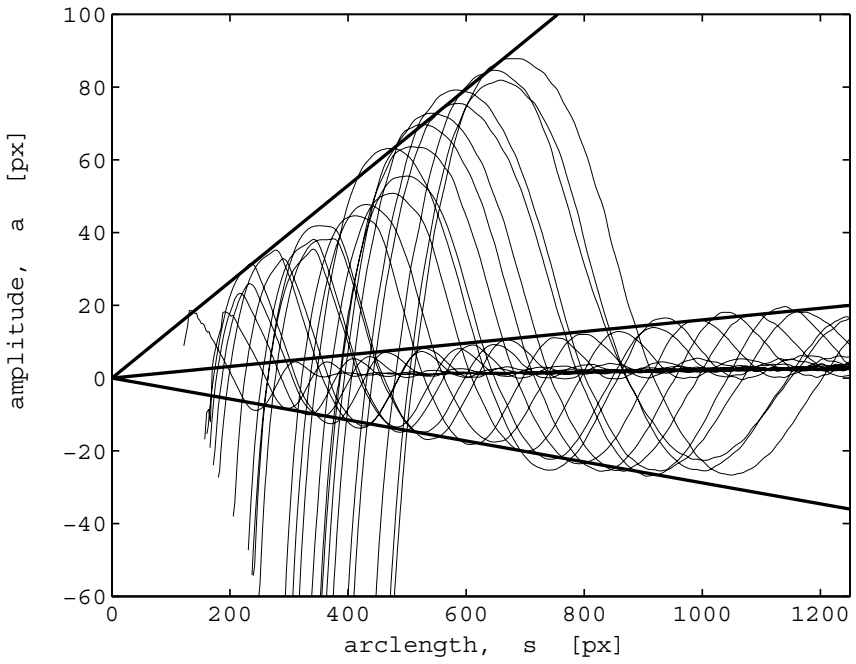

Figure 6-3: The Marangoni wave shapes for the second smallest needle D = 1.85 mm.

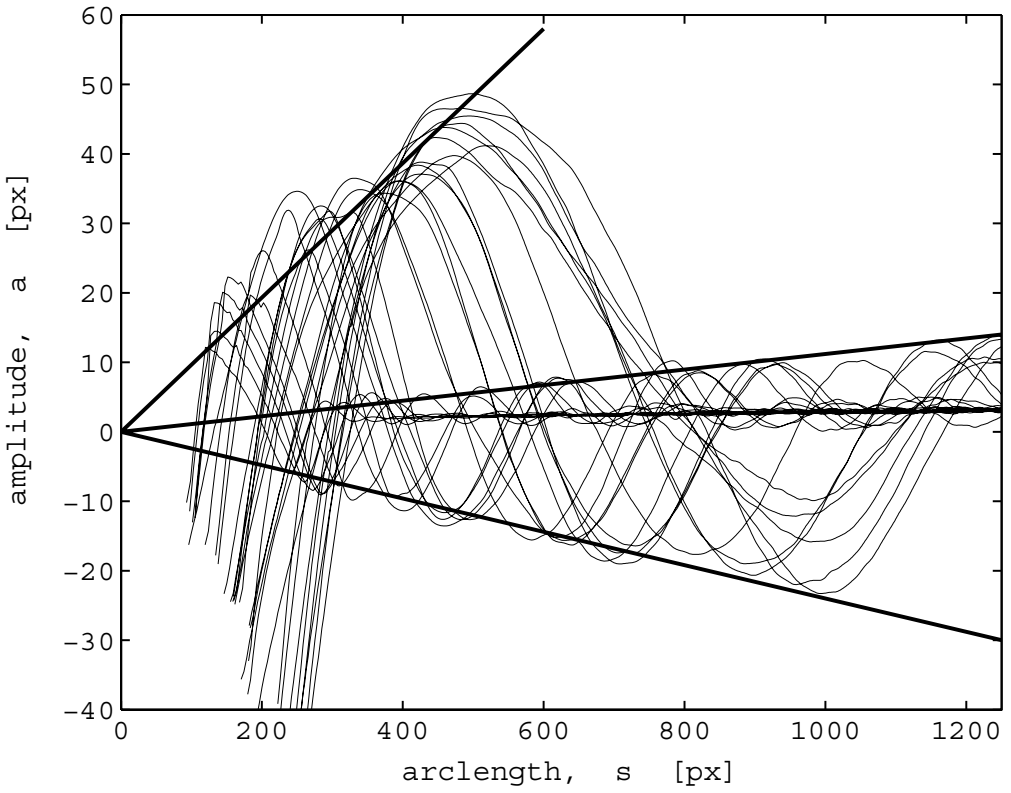

Figure 6-4: The Marangoni wave shapes for the smallest needle D = 0.88 mm.

However, the theory of Keller and Miksis (1983) suggests a power-law in terms of the time. By rescaling the Marangoni wave profiles from these figures by dividing the length-scales by $t^{2/3}$ and redrawing them in figure 6-5, we find that the waves presented similarity in both wave amplitude and wave length only showing slight shifts from the same wave-form.

It may be somewhat surprising that all the waves different size drops scale on the same curve. Notice that no length scaling was imposed in the figure, we got that Marangoni waves generating in coalescence of water/alcohol are similar regardless of coalescing drop size.

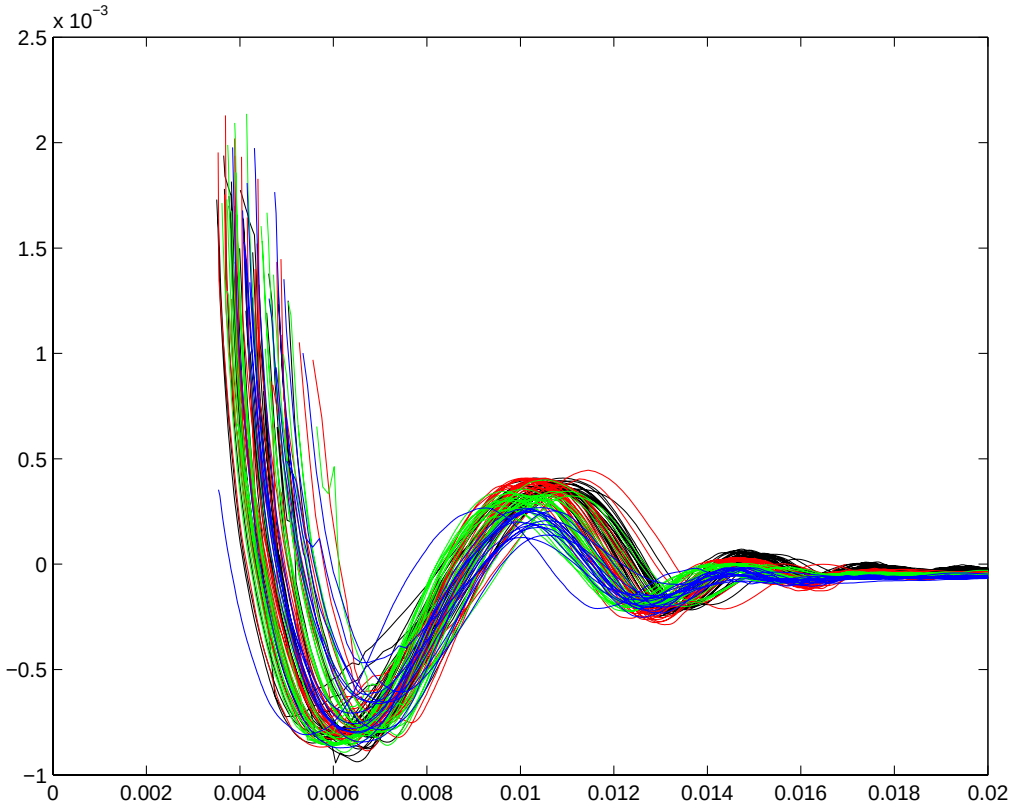

Figure 6-5: The Marangoni wave shapes scaled by dividing all lengths by time to the power 2/3. The axes have arbitrary units.

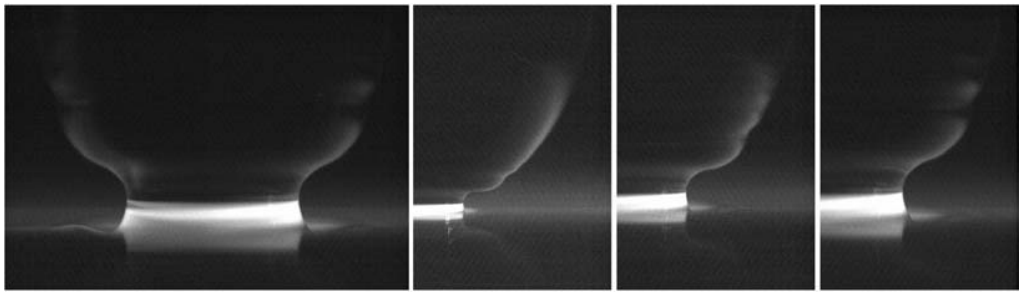

Figure 6-6: Interface imaging of a water drop coalescing with flat ethanol/water mixture surface, the times shown in the image from left to right are 2000, 500, 1200 and 1800us

Our assumption is that the Marangoni stresses generate the surface waves. In theory one should therefore be able to seed the ethanol with Fluorescein and observe it as it moves up the side of the drop. The same setup as before was applied to try to pick out

the interface during the coalescence of a water drop with a pool of ethanol and the results were presented in figure 6-6. However, because of the limited maximum output of laser energy and thinness of ethanol layer, we were unable to verify the existence of a thin layer of ethanol with this experimental setup. The theoretical treatment of Ruckenstein *et al.* (1970) suggests this layer is only of the order of 1 μm, which will certainly make it very difficult to observe. Even the weakest of reflections of the laser-light from the drop surface will, overpower this very weak fluorescence signal, despite the use of band-pass filters, as was explained in the experimental section.

6.2 The pool wave

Measurements of the pool-wave presented in section 5-5 can be used to estimate the added mass associated with the coalescence motions. Clanet and Quere (2002) have used a very simple model to estimate the added mass, in their work on the wetting of a solid rod which is brought into contact with a flat liquid surface. The added mass depends on the depth of the trough which forms in the pool, as this liquid is moved into the coalescing region. Knowing this added mass one can build a model to predict the speed of coalescence. Our measurements might allow for an improved estimate of this added mass, especially since the results presented here, show that the shape of the pool-wave is self-similar, i.e. the depth grows linearly with the radius of the trough as shown in figure 5-55.

The peculiar cone of drop-liquid which was discovered to penetrate the pool liquid (see figure 5-50), may give new insight into the fluid dynamics in the hole which opens up at the bottom of the drop, during the coalescence. It is well-known

that a water-drop coalescing with a water surface will generate a vortex ring. This has been known since Rogers (1858) and Thomson and Newall (1885). This vortex ring

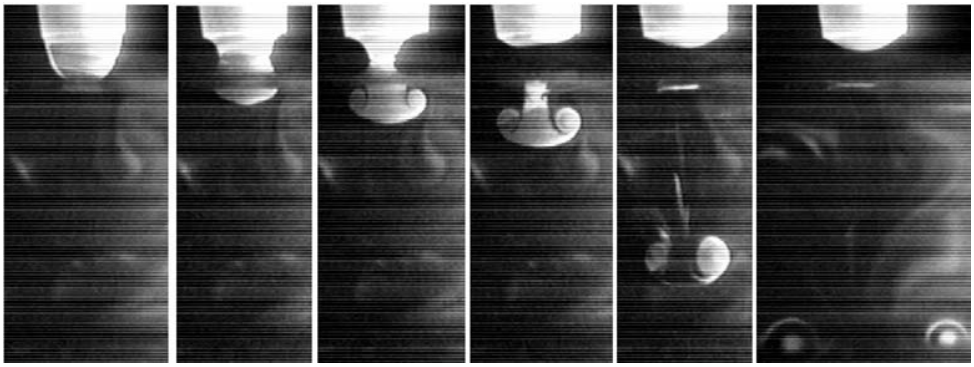

Figure 6-8: The vortex ring generated by the coalescence of a dyed water drop with a pool of water. (from Thoroddsen et al. 2005). The vortex ring hits the bottom of the tank in the last frame and expands due to the image vortex.

propagates into the pool liquid, as shown in figure 6-8, see Dooley *et al.* (1997) and Anilkumar et al. (1991). The vorticity in this ring is generated by the flow past the highly curved surface in the neck region, which is driven by the higher capillary pressure inside the drop, see Cresswell and Morton (1995). The present results show that the Marangoni forces appear to destroy this vortex ring, as it should show up along the water/ethanol interface, it it were present. Viscous forces will also destroy this vortex ring for the very viscous drop fluid. The vortex ring is therefore probably not present in any of the experiments shown in this thesis.

Figure 5-51 demonstrated that the cone is not driven by gravity, as the difference in densities between the two liquids is mostly balanced by buoyancy. The observed motions are even faster than if the drop liquid were in free-fall. This suggests that the higher capillary pressure inside the drop must drive down the drop liquid as the hole opens up.

6.3 The Neck Curvature for a Viscous Drop

The results in figures 5-31 and 5-35 show that the curvature in the neck region is strongly dependent on the viscosity difference between the two liquids. The largest curvatures in the neck region are observed for the coalescence of the most viscous drop with a less viscous pool liquid. This can be understood on the following physical grounds. As the viscosity of the drop is increased the capillary pressure in the neck region becomes less able to deform the drop surface, as it is counteracted by a large viscous stress inside the drop. However, the pool liquid has much lower viscosity, comparable to that of water. It can therefore be easily deformed and most of the motions therefore take place inside the pool liquid. Where the pool liquid meets the drop there will be a large mismatch in the viscous stress normal to the surface. This mismatch leads to the sharp curvature observed.

For early times this radius of curvature is very close to the optical resolution of the system, which has an ideal resolution of about 1 μm. The CCD pixels resolve between 1-2 μm. The curvature might therefore be even smaller. To determine this to a higher accuracy one would need to use a different optical system, possibly using shorter wavelength light, such as UV.

6.4 The coalescence of a small and a large drop

Section 5.1.2 showed the results when a small ethanol drop coalesces with a large water drop. This configuration was investigated to see the effects of the boundary conditions on the wave structure. In this case the bottom boundary is effectively 'pinned' at the smaller nozzle. The resulting Marangoni wave has a different shape from the one observed during the coalescence with an effectively 'infinite' pool.

Besides the pinning of the boundary, this configuration also reduces the length of the interface, from which the ethanol is pulled, as the neck radius is prohibited from growing as large. This most likely will lead to a reduction in the strength of the Marangoni stress. This could be investigated in a future study.

6.5 Effects of surfactants

Surfactants were found to reduce the Marangoni waves. This is to be expected, as the surfactant introduces surface elasticity, which tends to dampen surface waves. However, these experiments were rather limited in scope only investigating on type of surfactant and at only two surfactant concentrations. General conclusions can therefore not be drawn from these results, except that the Marangoni waves generated for with surfactants are much weaker than for the water ethanol case, even though the difference in the static surface tensions in the two cases are similar.

6.6 Recommendations for Future Work

The main drawback of this study is not being able to observe the whole coalescence process for a single drop, rather than construct a sequence from a numerous sets of image pairs. This unavoidably introduces some jitter in the results, primarily due to slightly different drop shapes and slightly different size of the initial contact between the drop and the pool. Therefore, future experiments should ideally be done with high-speed video cameras, so we can follow the free-surface evolution for one drop. This will require sufficient number of pixels in each video frame to extract the surface shape with sufficient fidelity. This would require approximately 1024×1024 pixels per frame at a frame-rate of around 100,000 fps. Currently

available high-speed video cameras can not supply this resolution and frame rates. It is likely that such cameras will not be available for the next 3-5 years.

Future work should include more variety of liquids, such as liquids containing different surfactants and of different concentrations. Liquids with non-Newtonian behavior would also be of interest, as the non-Newtonian behavior often is amplified at large strain-rates, which are present in the present coalescence configuration. Such an experiment could be performed using a polymer mixed in the liquid. Varying the concentration of this polymer will change the non-Newtonian response of the drop.

One can also imaging doing experiments with liquids containing a suspension of small particles. These particles could interact with the free surface in unexpected ways. They could for example prevent the area of the free surface from contracting. Such contraction occurs of course to minimize the surface area, but if the particles stick to the surface, they will change this contraction.

7 Conclusions

In this project, we have observed the early motions of a drop coalescing with a pool of liquid, by using a dual-image PIV camera in combination with an ultra-short-duration flash lamp to record two images of each coalescence event. The time evolution of the coalescence can be reconstructed by taking a sequence of image pairs at different times from the first liquid contact. The time was adjusted with a precise electronic trigger and time delay box under identical experimental conditions. To quantitively analyze the experimental images, several Matlab programs were written by the author to automatically extract the shape of coalescing drop and measure the shape of the surface Marangoni wave travels up the drop in the water/alcohol coalescence. The curvature of the surface was also measured for the coalescence of two liquids of greatly different viscosities.

This project studied mainly the configuration of a drop coalescing with a flat liquid surface and a few experiments of coalescence between a large drop and a very small drop. To reveal how the difference of liquid properties between liquids affected drops coalescence, we adjusted the properties of one of the liquids. To change the surface tension, we used water and ethanol. To change the viscosity we used different concentrations of glycerin/water mixtures.

We first looked at the effect of differential surface tension by coalescing a water drop onto a pool of ethanol and compared the wave motion on the drop surface with that produced by water onto a pool of water, i.e. the case without a surface tension difference. Comparison revealed that the outward speed of the neck region for water alcohol is slower than for water/water, suggesting that a thin film of alcohol

is pulled over the neck region by Marangoni forces, so that the lower surface tension drives the neck motions. The amplitude of traveling wave on the drop surface is also stronger for the Marangoni case and more wavelengths are observed along the drop surface. That indicated the amplitude of the surface wave is also affected by the Marangoni stress. Measurements of the Marangoni wave show that the wave shape extracted from a sequence of images looks similar with respect to $t^{2/3}$, with just a little bit of shifting on the original point. Further experiments with different tube size showed that similarity also exists among different size drops and that the wave amplitude as well as wave length does not change much with variation of drop size.

We also observed the coalescence of a highly viscous drop with a flat water surface and investigated the effect of varying viscosity on this coalescence. Experimental images demonstrated that the outward speed of the neck region bridging the liquids depends weakly on the viscosity of the more viscous drop, but the deformation of the drop shape depends strongly on the drop viscosity. Difference images for show that the capillary wave observed so prominently in the water/alcohol coalescence have disappeared. By increasing the drop viscosity, the curvature in the neck region became shaper. The sharpest curvature occurs where the two liquids meet. This was verified using fluorescent dye and laser illumination. Qualitative measurements were made of the total curvature in the corner of liquid contact. When the drop viscosity is reduced down to some limit, capillary wave reappeared.

Similar observation was obtained from investigation on the effect of viscosity difference in addition to the surface tension difference. This was done by testing coalescence of a viscous drop with a pool of alcohol. The higher viscosity of the drop eliminated the Marangoni wave and the pool liquid moved up the drop as if it were

wetting a solid surface. The corner at the advancing ‘contact line’ becomes progressively sharper as the drop viscosity increases.

Finally, we present the experimental results for the coalescence of water drop with a pool of water containing an addition of surfactants. These experiments were carried out with two different types of surfactants. Both showed significant deviations from the self-similar surface shapes, observed for water/ethanol coalescence.

Bibliography

Anilkumar, A. V., Lee, C. P. & Wang, T. G. (1991) "Surface-tension-induced mixing following coalescence of initially stationary drops", *Phys. Fluids A*, **3**, pp. 2587- 2591.

Biance, A.-L., Clanet, C. & Quere, D. (2004) "First steps of spreading", *Phys. Rev. E*, **69**, paper 016301, pp 1 – 4.

Charles, G. E. & Mason, S. G. (1960) "The coalescence of liquid drops with flat liquid/liquid interfaces", *J. Colloid Science*, **15**, pp. 105-122.

Clanet, C. & Quere, D. (2002) "Onset of menisci", *J. Fluid Mech.*, **460**, pp. 131-149.

Cresswell, R. W. & Morton, B. R. (1995) "Drop-formed vortex rings - The generation of vorticity", *Phys. Fluids*, **7**, pp. 1363.

Dooley, B. S., Warncke, A. E., Gharib, M. & Tryggvason, G. (1997) "Vortex ring generation due to the coalescence of a water drop at a free surface", *Exp. Fluids*, **22**, pp. 369-374.

Duchemin, L., Eggers, J. & Josserand, C. (2003) "Inviscid coalescence of drops", *J. Fluid Mech.*, **487**, pp. 167-178.

Dussaud, A. D. & Troian, S. M. (1998) "Dynamics of spontaneous spreading with evaporation on a deep layer". *Phys. Fluids*, **10**, pp. 23-38.

Eggers, J. (1997) "Nonlinear dynamics and breakup of free-surface flows", *Rev. Mod. Phys.*, **69**, No. 3, pp. 865.

Eggers, J., Lister, J. R. & Stone, H. A. (1999) "Coalescence of liquid drops", J. *Fluid Mech.*, **401**, pp. 293 - 310.

Etoh, T. G., Poggemann, D., Ruckelshausen, A. *et al.* (2002) "A CCD image sensor of 1 M frames/s for continuous image capturing of 103 frames", 2002 *IEEE Intl Solid-State Circuits Conf. Digest of Technical Papers, Visuals Supplement*, 30-31, vol. **386**, pp. 46 - 47.

Etoh, T. G., Poggemann, D., Kreider, G. (2003) "An image sensor which captures 100 consecutive frames at 1000000 frames/s", *IEEE Transactions on Electron Devices*, Vol. **50**, No. 1, 144 - 151.

Fordham, S. (1948) "On the calculation of surface tension from measurements of pendant drops", *Proc. Royal Soc., A*, **194**, No. 3, pp. 1-16.

Hopper, R. W. (1990) "Plane Stokes flow driven by capillarity on a free surface", *J. Fluid Mech.*, **213**, pp. 349 - 375.

Hopper, R. W. (1992) "Stokes flow of a cylinder and a half-space driven by capillarity", *J. Fluid Mech.*, **243**, pp. 171-181.

Hopper, R. W. (1993a) "Coalescence of two viscous cylinders by capillarity: Part I. Theory", *J. Am. Ceram. Soc.*, **76**, pp. 2947 – 2952.

Hopper, R. W. (1993b) "Coalescence of two viscous cylinders by capillarity: Part II. Shape evolution", *J. Am. Ceram. Soc.*, **76**, pp. 2953 - 2960.

Jensen, O. E. (1995), "The spreading of insoluable surfactant at the free surface of a deep fluid layer". *J. Fluid Mech.*, **193**, pp. 349-378.

Jones, A. F. & Wilson, S. D. R. (1978) "The film drainage problem in droplet coalescence", *J. Fluid Mech.*, **87**, pp. 263 - 288.

Joos, P. & Pintens, J. (1977) "Spreading kinetics of liquids on liquids". *J. Colloid Interface Sci.* **60**, pp. 507 - 513.

Keller, J. B. & Miksis, M. (1983) "Surface tension driven flows", *SIAM J. Appl. Math.*, **43**, pp. 268 – 277.

Keller, J. B., Milewski, P. A. & Vanden-Broeck, J.-M. (2000) "Merging and wetting driven by surface tension", *Eur. J. Mech. B-Fluids*, **19**, 491 – 502.

Keller, J. B., Milewski, P. A. & Vanden-Broeck, J.-M. (2003) "Breaking and merging of liquid sheets and filaments", *J. Eng. Maths*, **42**, pp. 283 – 290.

Lee, J. G., Mori, H. & Yasuda, Y. (2002) "Alloy phase formation in nanometer-sized particles in the In-Sn System", *Physical Review B, Condensed Matter and Materials Physics*, **65**, paper 132106, pp. 1-4.

Martinez-Herrera, J. I. & Derby, J. J. (1995) "Viscous sintering of spherical particles via finite element analysis", *J. Am. Ceram. Soc.*, **78**, pp. 645-649.

Miksis, M. J. & Vanden-Broeck J.-M. (1999) "Self-similar dynamics of a viscous wedge of fluid", *Phys. Fluids*, **11**, No. 11, pp. 3227-3231.

Menchaca-Rocha, A., Martinez-Davalos, A., Nunez, R., Popinet, S. & Zaleski, S. (2001) "Coalescence of liquid drops by surface tension", *Phys. Rev. E*, **63**, paper No. 046309, pp. 1 – 5.

Oguz, H. N. & Prosperetti, A. (1989) "Surface-tension effects in the contact of liquid surfaces", *J. Fluid Mech.*, **203**, pp. 149 – 171.

Peck, B. & Sigurdson, L. (1994) "The three-dimensional vortex structure of an impacting water drop", *Phys. Fluids*, **6**, 564 – 576.

Rein, M. (2002) "Capillary effects at newly formed liquid-liquid contacts", *Phys. Fluids*, **14**, pp. 411 – 414.

Richardson, S. (1992) "Two-dimensional slow viscous flows with time-dependent free boundaries driven by surface tension", *Eur. J. Appl. Maths*, **3**, pp. 193 – 207.

Rogers, W. B. (1858) "On the formation of rotating rings by air and liquids under certain conditions of discharge", *Am. J. Sci. Arts (Second Ser.)*, **26**, pp. 246 – 258.

Rother, M. A., Zinchenko, A. Z. & Davis, R. H. (1997) "Buoyancy-driven coalescence of slightly deformable drops", *J. Fluid Mech.*, **346**, pp. 117 - 148.

Ruckenstein, E., Smigelschi, O. & Suciu, D. G. (1970) "A steady dissolving drop method for studying the pure Marangoni effect", *Chem. Eng. Sci.*, **25**, pp. 1249-1254.

Santiago-Rosanne, M., Vignes-Adler, M. & Valerde, M. G. (1997) "Dissolution of a drop on a liquid surface leading to surface waves and interfacial turbulence", *J. Colloid & Interface Sci.*, **191**, pp. 65-80.

Shi, X. D., Brenner, M. P. & Nagel, R. S. (1994) "A Cascade of structure in a drop falling from a faucet", *Science*, **265**, pp. 219 – 222.

Sirringhaus, H., Kawase, T., Friend, R. H. *et al.* (2000), "High-resolution ink-jet printing of all polymer transistor circuits", *Science*, **290**, pp. 2123-2126.

Stover, R. L., Tobias, C. W. & Denn, M. M. (1997) "Bubble coalescence dynamics", *AIChE J.*, **43**, pp. 2385 - 2392.

Suciu, D. G., Smigelschi, O. & Ruckenstein, E. (1970) "The spreading of liquids on liquids", *J. Colloid Interface Sci.*, **33**, pp. 520 - 528.

Tan, E. & Thoroddsen, S. T., (1998a), "The Thistle Crown", Winner in the APS Gallery of Fluid Motion, *Phys. Fluids*, **10**, pp. s7.

Tan, E. & Thoroddsen, S. T. (1998b) "Marangoni instability of two liquids mixing at a free surface", *Phys. Fluids*, **10**, pp. 3038 - 3040.

Thomson, J. J. & Newall, H. F. (1885) "On the formation of vortex rings by drops falling into liquids, and some allied phenomena", *Proc. R. Soc. London*, **39**, pp. 417-436.

Thoroddsen, S. T., Etoh, G. T. and Takehara, K. (2003) "Air entrapment under an impacting drop", *J. Fluid Mech.*, **478**, pp. 125-134.

Thoroddsen, S. T., Takehara, K. & Etoh, T. G. (2005) "The coalescence speed of a pendent and a sessile drop". *J. Fluid Mech.*, **527**, pp. 85-114.

Thoroddsen, S. T., Etoh, T. G., Takehara, K. & Ootsuka, N. (2005) "On the coalescence speed of bubbles", *Phys. Fluids*, **17**, paper no. 071703, pp. 1-4.

Thoroddsen, S. T. & Takehara, K., (2000) "The coalescence-cascade of a drop", *Phys. Fluids*, **12**, pp. 1265-1267.

Velev, O. D., Prevo, B. G. & Bhatt, K. H. (2003) "On-chip manipulation of free droplets", *Nature*, **426**, pp. 515-516.

Wu, M., Cubaud, T., Ho, C.-M. (2003) "Coalescence of liquid droplets in micro fluidic device", *Bulletin of APS*, **48**, p. 224 (abstract only).

Wu, M., Cubaud, T., Ho, C.-M. (2004) "Scaling law in liquid drop coalescence driven by surface tension", *Phys. Fluids*, **16**, pp. L51-L54.

Zeff, B. W., Kleber, B., Fineberg, J. & Lathrop, D. P. (2000) "Singularity dynamics in curvature collapse and jet eruption on a fluid surface", *Nature*, **403**, pp. 401 - 404.